Fabrication of visible range hollow Bragg waveguides

by

Aaron David Melnyk

A thesis submitted in partial fulfillment of the requirements for the degree of

Master of Science

in

Photonics and Plasmas

Department of Electrical and Computer Engineering
University of Alberta

Abstract

This thesis describes the fabrication and characterization of visible-range hollow Bragg waveguides. A wafer bonding method was first utilized to fabricate tapered hollow Bragg waveguides, which can function as the dispersive element of an integrated spectrometer. Etched channels coated with Bragg reflector claddings enabled three-dimensional guiding. These prototypes were used to assess the spectroscopic sensing capability of the waveguides, and in particular their potential for integration into microfluidic sensing systems. The emission spectra of fluorescent microspheres were extracted, with an experimentally determined resolution as low as 0.9nm, and the results were shown to be in good agreement with measurements made by a commercial spectrometer.

Hollow waveguides were subsequently fabricated by controlled thin film buckling. Lithographically patterned areas of a low-adhesion material were embedded between matching Bragg reflectors. Heating the samples induced the buckling of the compressively stressed upper cladding over the regions defined by the low-adhesion layer. Ta_2O_5/SiO_2 multilayers combined with a fluorocarbon-based low-adhesion layer were found to produce buckle features consistent with the morphology predicted by elastic buckling theory. Device yield was as high as 60% and waveguide loss was as low as 2.6dB/cm at 543nm wavelength. These devices have potential applications in optofluidic microsystems as well as in fundamental physics studies.

Preface

Chapter 4 of this thesis has been published as A. Melnyk, M. H. Bitarafan, T. W. Allen, and R. G. DeCorby, "Air gap resonant tunneling bandpass filter and polarizer," Opt. Lett. **41**, 1845–1848 (2016). I was responsible for device fabrication, experimental analysis and manuscript composition. I was assisted with fabrication and manuscript edits by M.H. Bitarafan. T.W. Allen assisted with the experimental analysis and aided with manuscript edits. R.G. DeCorby was the supervisory author, was responsible for concept formation and device design, and also assisted with manuscript composition.

Chapter 6 of this thesis has been published as A. Melnyk, C.A. Potts, T. W. Allen, and R. G. DeCorby, "Visible range hollow waveguides by guided buckling of Ta_2O_5/SiO_2 multilayers," Appl. Opt. (in press, 2016). I was responsible for sample fabrication, experimental analysis and manuscript composition. C.A. Potts assisted in fabrication and manuscript edits. T.W. Allen was involved with concept formation and manuscript edits. R.G. DeCorby was the supervisory author and was involved with concept formation and manuscript composition.

Acknowledgements

I would like to start by thanking Dr. Ray DeCorby for his support, advice, and mentorship throughout my degree. Your calmness and guidance, even under the most intense deadlines, always put things in perspective.

The DeCorby research group has been a relatively small one, but one that I have grown to appreciate and love. The small nature of the group made for an intimate research experience and one which helped cultivate what I hope to be life-long friendships. Special thanks to Brian Drobot, Clinton Potts, and Mohammad Bitarafan for the countless hours spent helping with fabrication and experimentation (and enabling my coffee addiction). I would also like to thank Dr. Trevor Allen for his advice and experimental expertise. I can only imagine how many grammatical errors my manuscripts would have without your help. I'd also like to extend thanks to Min Choi and Carson Zhang.

I can't express my gratitude enough for the entire nanoFAB staff for providing such a welcoming place to make mistakes, learn, and ultimately succeed. I'd especially like to thank Les Schowalter. Without your insight my thesis would not have been possible.

Lastly, I'd like to thank all my family and friends whose unwavering support and patience provided the gentle encouragement I needed.

This research was supported financially by the Natural Sciences and Engineering Research Council (NSERC), Alberta Innovates Technology Futures (AITF), and the University of Alberta.

Table of Contents

List of Tables

List of Figures and Illustrations

List of Symbols, Abbreviations and Nomenclature

Abbreviations

ARROW	Anti-resonant reflecting optical waveguide
BPF	Band-pass filter
CCD	Charged-coupled device
cQED	Cavity quantum electrodynamics
CVD	Chemical vapour deposition
dB	Decibel
DBR	Distributed Bragg Reflector
DC	Direct current
DI	Deionized
FC	Fluorocarbon
FP	Fabry–Pérot
FSR	Free spectral range
FTIR	Frustrated total internal reflection
FWHM	Full width half max
HDMS	Hexamethyldisilazane
ICP-RIE	Inductive coupled plasma reactive ion etch
IPA	Isopropyl alcohol
LAL	Low adhesion layer
LED	Light emitting diode
LOC	Lab-on-a-chip
LVF	Linear variable filter
MEMS	Microelectromechanical systems
NA	Numerical aperture
OD	Optical density
ODR	Omnidirectional dielectric reflector
PBG	Photonic band gap
PDL	Polarization dependant loss
PDMS	Polydimethylsiloxane

PECVD	Plasma enhanced chemical vapour deposition
PTFE	Polytetrafluoroethylene
QED	Quantum electrodynamics
QWS	Quarter-wave stack
RF	Radio frequency
sccm	Standard cubic centimeter
SEM	Scanning electron microscope
TE	Transverse electric
TIR	Total internal reflection
TM	Transverse magnetic
TWS	Tapered waveguide spectrometer
VASE	Variable angle spectroscopic ellipsometer

Symbols

b	Half width of buckling region
c	Speed of light
$C(\lambda)$	Correction factor
d	Layer thickness
d_c	Core thickness
D_T	Spatial dispersion
$d\lambda$	Wavelength resolution
$\mathbf{k}$	Wavevector
K	Phase-shift coefficient
k_o	Free-space wavenumber
M	Integer mode order
n	Index of refraction
n_{eff}	Effective index
r	Amplitude reflection coefficients
R_{Bragg}	Peak reflectance at normal incidence
$S_c(\lambda)$	Reference spectrum
S_T	Taper slope

$S_T(\lambda)$	Raw spectrum
T_b	Temperature for the onset of buckling
$w(y)$	Buckle height
w_{max}	Peak buckle height
Y	Young's modulus
Zp	Effective detector array pixel size
α	Waveguide loss
α_m	Intensity attenuation coefficient
β_m	Mode propagation constant
δ_{eff}	Effective phase thickness
δ_i	Phase thickness
$\Delta\lambda_{Bragg}$	Width of the fundamental stop band
η	Admittance
η_{eff}	Effective admittance
θ	Angle
θ_B	Brewster angle
k	Extinction coefficient
λ	Wavelength
λ_{Bragg}	Bragg wavelength
ν	Poission ration
σ_f	Film stress
Φ	Phase shift
ϕ_m	Bounce angle
ω	Angular frequency

Chapter One: Background and motivation

1.1 Introduction

Optical sensing is one of the most widely used analysis techniques for a variety of fields including biology, chemistry, environmental monitoring and toxicology. In recent years there has been a strong shift to develop integrated on-chip sensing solutions [1]. This is motivated by a desire for cost-effective, portable and efficient methods for in-situ analysis of small volume samples. To reach this ultimate goal, there is a need for integrated optical components, such as hollow waveguides, that allow for light propagation and sensing in gases and liquids. The development of such a hollow-waveguide-based platform might allow for fully integrated sensing solutions, and is a key theme within the field of optofluidic microsystems [2].

Some of the most compelling applications for integrated hollow waveguides, such as fluorescence detection and fundamental physics studies, are typically performed in the visible or near-visible wavelength range [3–6]. Previous work by the DeCorby group on integrated hollow Bragg waveguides has shown promise to address some of these applications [7,8]. However, earlier results were limited to the near infrared wavelength range. The main objective of this thesis was to develop a fabrication process for realizing hollow core Bragg waveguides in the visible range. Towards this goal, waveguides were first fabricated using a wafer bonding method, in order to produce proof-of-concept devices for fluorescence sensing. Subsequently, hollow waveguides operating in the visible range were fabricated using a buckling self-assembly method. This chapter provides an overview of some important applications, typical operating schemes, and current fabrication trends for hollow waveguides. An outline of the thesis is provided at the end of the chapter.

1.2 Applications of integrated hollow waveguides

Hollow waveguides offer distinct advantages over their solid-core counterparts, including a significant reduction in nonlinear effects, dispersion, absorption and scattering [9], as well as the

ability to simultaneously confine light and an analyte within the same volume. These characteristics make hollow waveguides a perfect fit for many sensing applications.

Kumar recently proposed hollow Bragg waveguides as a tunable platform for a variety of photonic network applications [10]. Those devices (see Fig. 1.1(a)) consist of matching distributed Bragg reflectors (DBRs) with an air-gap spacing that can be mechanically controlled using either a piezoelectric or MEMS actuator. That platform has potential for realizing components such as dispersion and polarization manipulating devices and, when integrated with an optical amplifier, can potentially be the basis for a tunable semiconductor laser platform.

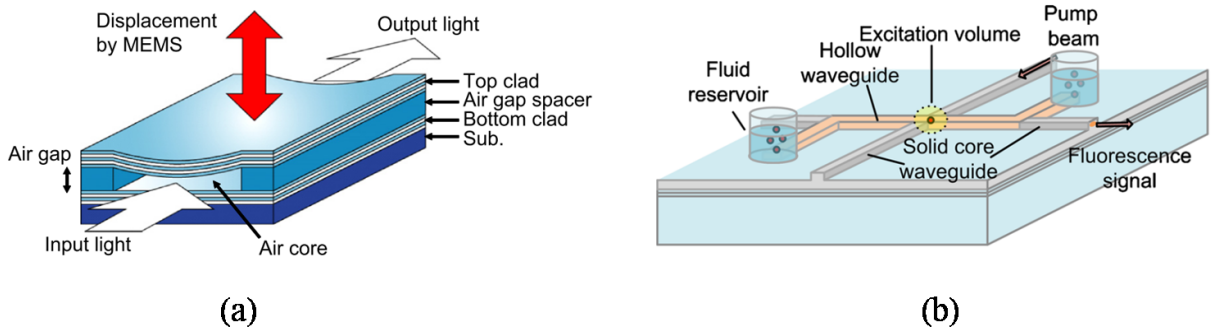

Figure 1.1 - (a) A tunable hollow waveguide consisting of Bragg reflector claddings separated by an air gap spacer. Tunability is provided by MEMS displacement. Adapted from [10]**. (b) A schematic of an integrated optofluidic chip for sensing applications, adapted from** [11]**.**

The ability to fill the core with a liquid analyte has also made hollow waveguides of interest for optofluidic sensing applications. In recent years, advancements in microfluidics has led to integrated devices combining valves, mixers and pumps, which can enable complex chemical analysis on a chip [12]. Ongoing research seeks to eliminate the reliance of these systems on bulky off-chip components and push for smaller device footprints. Co-integration of fluid channels and optical waveguides is one promising approach. A variety of optical sensing mechanisms can be used in optofluidic devices, including: refractive index, fluorescence, Raman scattering, absorption and polarization based detection modalities [1]. These techniques can be used individually or in combination, and offer rapid sensing of small volumes with high sensitivity, in some cases even enabling single molecule detection [2,13]. A schematic of an optofluidic chip containing integrated solid and hollow core waveguides and liquid reservoirs is

shown in Fig. 1.1(b). Research fields such as chemistry, toxicology, environmental monitoring and biosensing are all expected to benefit greatly from further advancements in optofluidic devices [14] .

Another emerging application for hollow core waveguides is the study of fundamental quantum coherence effects. Hollow waveguides, on their own or combined with other optical elements such as resonant cavities, have the ability to analyze and sense fundamental light-matter interactions on an atomic scale [4–6]. Optical microcavities are among the most important tools in the study and manipulation of quantum mechanical interaction between light and matter [5]. It is desirable to integrate such cavities with photonic elements such as hollow waveguides, which can be used to transfer signals and supply gas molecules [5]. The small core cross sections in hollow waveguides allow for the enhancement of optical intensity and maximize the nonlinear optical effects necessary to observe and sense these light-matter interactions [4]. Further advancements will allow these devices to be the basis for compact magnetometers, atomic clocks and complex quantum networks [4].

1.3 Confinement mechanisms for hollow waveguides

The most common optical waveguides, such as optical fibers or those used in silicon photonics platforms, consist of a higher index core, n_1, that is surrounded by a lower index cladding material, n_2. As depicted in Fig. 1.2(a), light is confined to the high index core by total internal reflection (TIR) at the core-cladding boundaries, the condition for which is defined as:

$$\theta_i > \sin^{-1}(n_2 / n_1) = \theta_C \ , \tag{1.1}$$

where θ_c is the critical angle for TIR. Solid state waveguides based on TIR can transport a signal over long distances with extremely low losses [15]. However, for waveguides designed for light confinement in a gas (e.g. air, $n_{air} = 1$) or liquid (e.g. water, $n_{H2O} = 1.33$) core, finding suitable low index cladding materials is challenging [2]. While using TIR for a gaseous core is not possible at this time, there are several clever methods used for guiding within a liquid medium. Teflon AF ($n = 1.29$) is one such material that provides a sufficiently low index to adequately guide light in an aqueous core waveguide. Integrated hollow waveguides fabricated with Teflon AF claddings have been shown to have loss on the order of a few dB/cm, and fluorescence detection has been accomplished using both silicon and PDMS based platforms [16,17]. The

adhesion of Teflon AF remains a challenging aspect to the fabrication of these devices, along with precise control over the cladding thickness.

An alternative method to reach the TIR conditions is to add nano-sized air pores to a high index material in order to reduce its effective index to be lower than that of the guiding region. Devices fabricated using this method have been shown to have propagation losses ~6dB/cm [18]. A particular advantage of this approach is the ability to tune the index contrast between the core and cladding, which can potentially enhance the fluorescence collection efficiency of these devices over those fabricated using Teflon AF claddings [18,19]. However, only planar, one-dimensional confinement has been demonstrated at this time. Provided that a pathway to two-dimensional mode confinement can be developed, this looks to be a very promising technology.

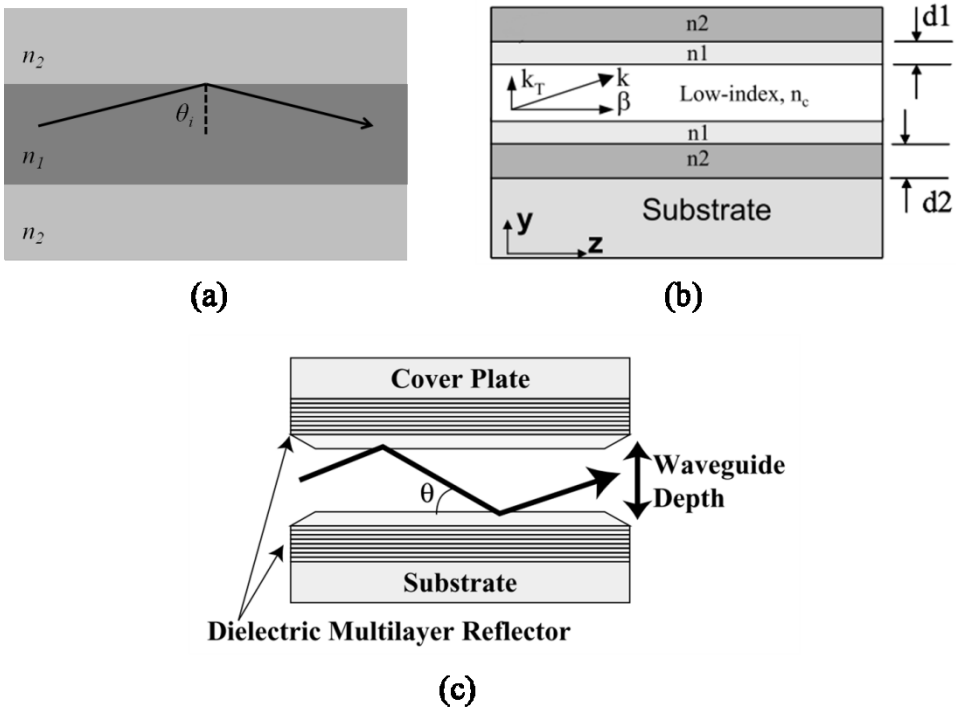

Figure 1.2 - Schematics of various waveguides. (a) The propagation of light in a waveguide based on TIR. (b) A side view of an ARROW, adapted from [20]**. (c) A side view of a waveguide with Bragg reflection claddings, adapted from** [21]

In order to guide light in a gaseous core, TIR is not generally possible and an alternative guiding mechanism must be used. Typically, this can be accomplished using interference-based multilayer claddings. In this case, the hollow core is surrounded by a dielectric multilayer. An

incident electromagnetic wave undergoes reflections at each dielectric interface, and these partial reflections are made to interfere constructively in order to maximize the overall reflectance. This enables low-loss (but leaky) propagation modes to exist within the hollow core.

One such example of an interference based waveguide is the anti-resonant reflecting optical waveguide (ARROW). First proposed by Duguay *et al.* in 1986 [22], these devices utilize an antiresonant condition to confine light within the core. The cladding material is chosen to be higher index than the core material, such that a light wave incident from the core is refracted into the cladding layer. The thickness of the cladding is chosen carefully to create an antiresonance condition of the equivalent Fabry-Perot cavity for the design wavelength. This thickness for the cladding material, d_i, to achieve the anti-resonance condition, can be expressed approximately as [22]:

$$d_i > \frac{\lambda}{4n_i}(2N+1)\left[1-\frac{n_c^2}{n_i^2}+\frac{\lambda^2}{4n_i^2 d_c^2}\right]^{1/2}, \tag{1.2}$$

where n_i and n_c are the cladding and core refractive indices, respectively and N is an integer representing the antiresonance order. A side view of a simple ARROW is presented in Fig. 1.2(b). The anti-resonances of a Fabry-Perot cavity are relatively broad, which in turn allows for a broad low loss transmission band [22]. Additionally, loss can be reduced further by adding more layers that satisfy the antiresonance condition [2]. Devices have been fabricated using both wafer bonding and sacrificial etching techniques [2], with hollow core loss on the order of ~10dB/cm [11,23]. A significant advantage of ARROWs is that the layers do not need to be periodic or even of the same material, which affords significant design flexibility. Further to this, careful layer design can allow for wavelength selectivity, allowing for built in wavelength filtering, an attractive characteristic for fluorescence sensing and Raman spectroscopy [24]. Researchers have recently demonstrated integrated ARROW waveguides as part of optofluidic chips that are capable of single molecule detection [25].

Another type of interference-based waveguide employs Bragg reflection claddings. In this case, guiding is achieved by constructive interference of an electromagnetic field reflected from a cladding composed of a periodic structure of alternating high and low index materials. The periodic structure of a Bragg reflector results in a photonic bandgap that corresponds to the range of wavelengths for which propagation through the multilayer is forbidden. This in turn

determines the wavelength range for which low loss guided modes are supported by the waveguide structure [26]. A schematic diagram depicting the propagation through a Bragg waveguide structure is shown in Fig. 1.2(c). Similar to ARROWs, hollow Bragg waveguides have been shown to provide broadband transmission and can exhibit low propagation loss [27]. Bragg waveguides have been studied extensively be the DeCorby group [27–30], and are the basis for the hollow waveguides discussed in this thesis. An analytical treatment of the Bragg waveguide is presented in Chapter 2.

1.4 Fabrication techniques

1.4.1 TIR-based hollow waveguides

As mentioned, the fabrication of hollow waveguides for liquid sensing has proven difficult, due to the limited options available for the low index cladding. Che *et al.* flowed a Teflon AF solution through fabricated PDMS microchannels (see Fig. 1.3(a)) [17]. Excess solution was removed during a vacuum step. The thickness of the Teflon AF cladding is determined by the vacuum force, which counteracts the adhesion of the Teflon AF to the PDMS sidewalls. Smooth cladding walls were successfully fabricated in a PDMS chip with various geometries.

Motivated by the poor collection efficiency of Teflon AF based TIR waveguides (due to the limited index contrast), nanoporous claddings have also been investigated. Risk et al., selectively removed the organic macromolecular phase in a hybrid organic/inorganic polymer [19]. The pores produced were on the scale of ~10-15nm, much smaller than the wavelength of visible light, enabling an effective medium approach to be used in assessing the cladding index. As depicted in Fig. 1.3(b), two nanopore substrates were then held in close contact with a water "core" between them. Although limited to one-dimensional confinement, optical losses as low as ~1dB/cm were reported. Gopalakrishnan *et al*. presented an alternative approach (see Fig. 1.3(c)), whereby a polymer with etched nanopores is exposed to UV light in specific regions, which alters the hydrophobicity of the material and defines the regions where liquid can flow [18]. Planar waveguides with solid-liquid hybrid cores were successfully fabricated, with losses on the order of 6.2dB/cm. Regions of the solid-liquid core were exposed to air, however, limiting the integration time as the liquid is susceptible to evaporation. To support 3D guiding, a wafer bonding step is likely required.

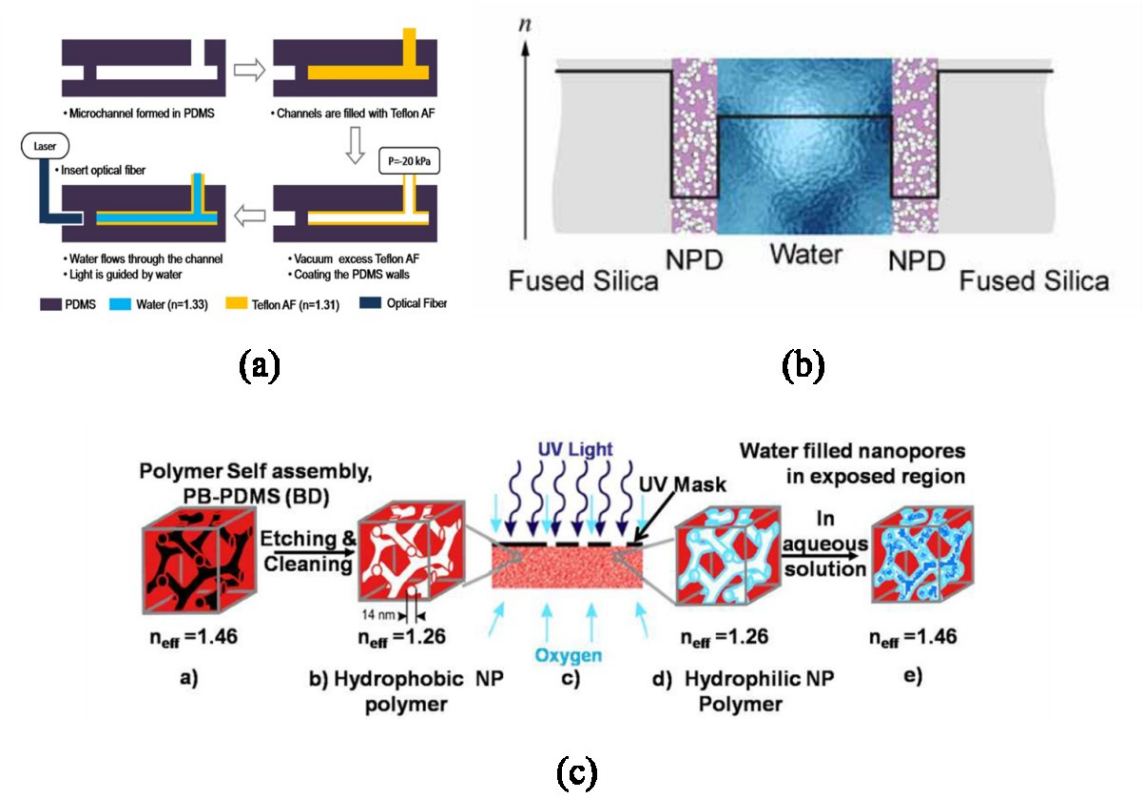

Figure 1.3 - (a) Fabrication steps to create TIR based waveguides with Teflon AF claddings, adapted from [17]**. (b) Cross section of a hollow waveguide with a liquid core and nanopore claddings, adapted from** [19]**. (c) Fabrication steps to create a TIR based waveguide with solid-liquid hybrid cores with nanopore claddings, adapted from** [18]**.**

1.4.2 Wafer bonding

In order to fabricate hollow core waveguides that are suitable to facilitate gas- and liquid-based sensing and related applications, wafer bonding is one of the most common approaches reported in the literature. A typical wafer bonding process can be outlined in three steps, as depicted in Fig. 1.4. First, channels are etched into a planar substrate to define the core region. Second, matched claddings are deposited on the etched substrate and another blank substrate. Last, the two separate substrates are bonded together, creating hollow core waveguides having the geometry of the etched channels.

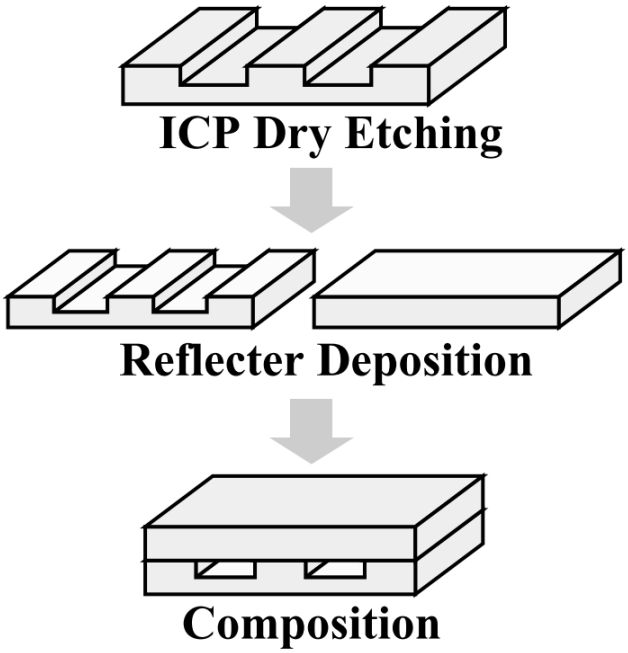

Figure 1.4 - Generalized fabrication steps used to create hollow waveguides using the wafer bonding technique, adapted from [21]**.**

Examples in the literature include the use of metallic mirrors [21], Bragg mirrors [9], or ARROW based claddings [31]. Typically, the channels are formed using dry etch methods to provide deep trenches with smooth sidewalls. Chemical vapour deposition (CVD) is often necessary to ensure good sidewall coverage in the etched channels. Bonding is typically facilitated by silicon nitride bonding [31], or mechanical pressure [21]. Waveguide losses as low as 1.7 dB/cm have been reported [9]. The wafer bonding method, however, is highly susceptible to film non-uniformities, surface roughness, and particulates that can result in gaps (see Fig 1.5). The demanding alignment tolerances for small-core hollow waveguides presents challenges in fabricating fully enclosed hollow waveguides using this method.

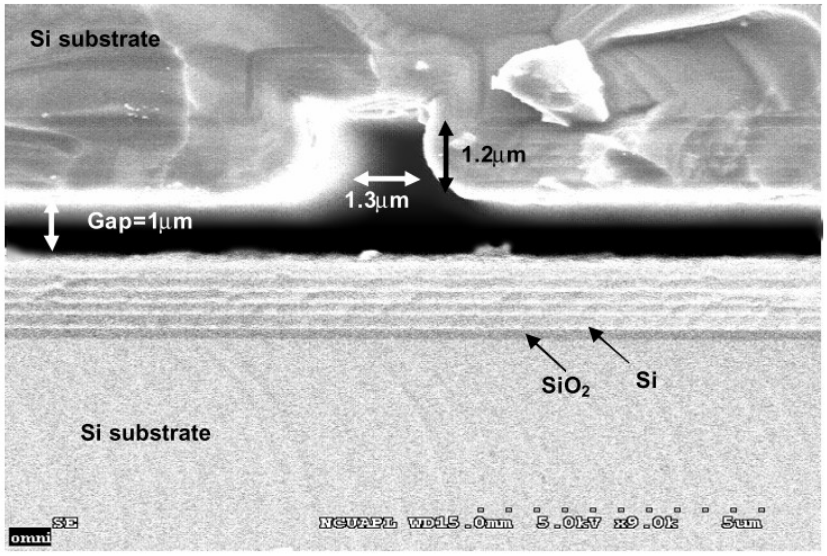

Figure 1.5 - SEM image of the cross section of a hollow waveguide fabricated using the wafer bonding technique, adapted from [9]**.**

1.4.3 Sacrificial etching

Another traditional approach for fabricating hollow waveguides is to use sacrificial etching methods. This approach has been used extensively by Hawkins and Schmidt [32], and relies on dielectric claddings that surround a sacrificial material, which is in turn selectively removed to create the hollow cores. A representative fabrication process is shown in Fig. 1.6(a). First, the bottom cladding is deposited using plasma enhanced CVD (PECVD) or sputtering. Next, the sacrificial material is patterned, using lithography and etching, to define the geometry of the waveguide. The top cladding is then deposited using PECVD or sputtering, enclosing the core. The sacrificial material is then selectively etched, producing hollow cores surrounded by dielectric claddings.

Metals and photosensitive resins (SU-8) have both been used as the sacrificial material [14]. The ARROW based cladding materials have been typically SiO_2 combined with either SiN or Ta_2O_5 [11,32]. Losses as low as ~11dB/cm and ~13dB/cm have been reported for the SiN and Ta_2O_5-based multilayers, respectively. Complex devices, complete with solid and liquid core interconnects and liquid reservoirs, have been fabricated and were used to demonstrate fluorescence sensing and single molecule detection [13].

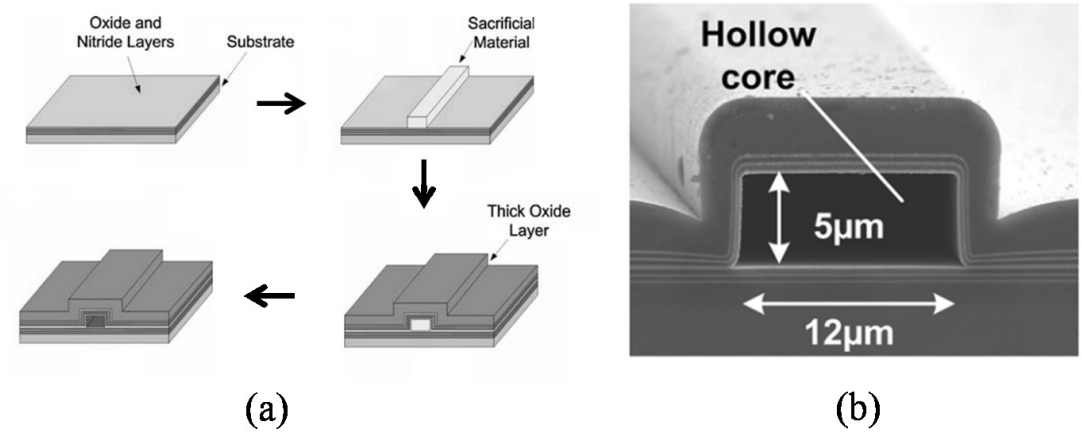

Figure 1.6 - (a) Fabrication steps used to create hollow core ARROWs using the sacrificial etching technique, adapted from [14]**. (b) An SEM of the end facet of a fabricated ARROW, adapted from** [11]**.**

1.5 Summary of thesis

This thesis details the fabrication and optical testing of hollow core waveguides operating in the visible wavelength range. The devices are an extension of prior research done by the DeCorby group [7,27,28] and are based on interference-based guiding, facilitated by Bragg reflector claddings.

Chapter 2 details the theoretical background of Bragg reflection and describes the operation of hollow waveguides with Bragg reflector claddings. The use of controlled thin film buckling to produce hollow cavities is introduced, and the conditions needed to produce low-loss hollow waveguides are examined.

The optical characterization of tapered hollow waveguides, fabricated using a wafer bonding technique, is described in Chapter 3. Those devices served as a proof of concept for fluorescence sensing and microfluidic integration using hollow Bragg waveguides. Performance, as well as limitations of the wafer bonding technique, is described.

Expanding the versatility of the wafer bonding technique, Chapter 4 describes the design, fabrication and optical characterization of a tunneling bandpass filter. The characteristics of the concept (air gap tunneling layer embedded between dielectric thin film stacks) complements many of the concepts discussed in Chapter 2 and borrows the wafer bonding technique in Chapter 3 and deposition techniques detailed further on in Chapter 5.

Chapter 5 provides the in-depth development of the fabrication platform used to create buckled hollow waveguides operating in the visible region. The reactive sputtering of optical thin films, control of thin film stress, optimization of the release mechanism, and morphology of the resultant buckles are discussed in detail.

Refined devices with improved optical characteristics, fabricated using the platform developed in Chapter 5, are presented in Chapter 6. The morphology and optical performance of the refined devices is presented along with a brief outlook for future applications.

Chapter 7 serves to summarize the thesis and provide a framework for future work.

Chapter Two: Theoretical background

2.1 Introduction

This chapter discusses some background and theory relevant to subsequent chapters. I begin by describing the basic theory and design of distributed Bragg reflectors. Omnidirectional reflectors are discussed next, including theory regarding the operation of hollow waveguides clad by omnidirectional reflectors. Finally, theory pertaining to thin film stress and elastic buckling mechanics is described.

2.2 Bragg reflectors

Reflecting devices, or mirrors, are amongst the most prevalent of all optical devices. For many applications metal- based mirrors have adequate performance. Moreover, they provide relatively high levels of reflectance over a broad range of wavelengths and for nearly all incident angles. However, for some demanding applications, such as laser cavities and transmittance filters, higher-performance mirrors are necessary. This is due to the lossy nature and limited reflectance of metallic materials. Aluminum based mirrors, for example, peak at ~91% reflectance, with several percent of the incident light being absorbed by the film [33]. Mirrors based on stacks of dielectric materials, on the other hand, can provide reflectance as high as 99.999% in extreme cases [34].

2.2.1 Quarter Wave Stacks

A particularly important type of dielectric mirror is the distributed Bragg reflector (DBR). A DBR consists of alternating layers of high and low index materials, in which the thickness of each layer is tuned to be a quarter of a wavelength thick for some centre wavelength, λ_{Bragg}. Consequently, these structures are also commonly called quarter wave stacks (QWS). The quarter-wave condition is expressed as:

$$\lambda_{Bragg} = 4n_1 d_1 = 4n_2 d_2 \,, \tag{2.1}$$

where n_1 and n_2 are the indices of refraction and d_1 and d_2 are the thicknesses of the alternating layers 1 and 2, respectively.

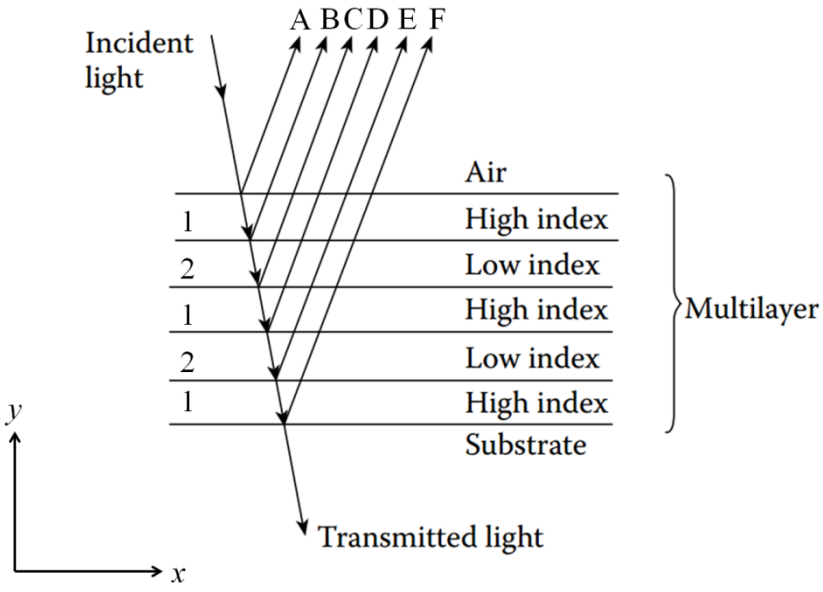

Figure 2.1 - Constructive interference interpretation of a distributed Bragg reflector based on the quarter-wave stack condition with alternating layers 1 and 2 with indices n1 and n2. Adapted from [33]**.**

A light wave incident on a DBR will have partial reflections at each boundary within the multilayer (see Fig. 2.1). Using the QWS condition, the partially reflected waves will all be in phase as they exit the multilayer and therefore combine constructively, enabling high reflectance. The peak reflectance of a QWS multilayer with an even number of layers can be expressed in closed form as [35]:

$$R_{Bragg} = \left[\frac{1 - \left(\frac{n_s}{n_o}\right)\left(\frac{n_1}{n_2}\right)^{2N}}{1 + \left(\frac{n_s}{n_o}\right)\left(\frac{n_1}{n_2}\right)^{2N}} \right]^2 . \tag{2.2}$$

For a QWS with an odd number of layers, the analogous expression is:

$$R_{Bragg} = \left[\frac{1 - \left(\frac{n_1}{n_o}\right)\left(\frac{n_1}{n_s}\right)\left(\frac{n_1}{n_2}\right)^{2N}}{1 + \left(\frac{n_1}{n_o}\right)\left(\frac{n_1}{n_s}\right)\left(\frac{n_1}{n_2}\right)^{2N}} \right]^2, \tag{2.3}$$

where n_o and n_s are the indices of the incident and substrate materials and N is the number of periods in the stack. With an appropriately large index contrast and high number of periods R_{Bragg} rapidly approaches unity. Reflectance values as high as 0.99999 have been reported in the literature [34].

Bragg reflectors exhibit high reflectance for a range of wavelengths in the vicinity of λ_{Bragg}. The spectral width of this range, or stopband, at normal incidence can be expressed as [36]:

$$\Delta\lambda_{Bragg} = \lambda_{Bragg} \frac{4}{\pi} \arcsin\left[\frac{|n_2 - n_1|}{n_2 + n_1} \right]. \tag{2.4}$$

The stopband width represented by eq. 2.4 scales directly with the index contrast of the two constituent materials. Thus, for a given application careful selection of materials is paramount to ensure operation over the required wavelength range.

2.2.2 Omnidirectional dielectric reflectors

Metallic mirrors provide nearly omnidirectional reflection, that is, high reflectivity for nearly all polarization states and incident angles. Historically, Bragg reflectors have only achieved high reflectance for one polarization and/or a specific range of incident angles. Past attempts to expand the reflectance range for all incident angles or polarizations involved special high index materials or a cumbersome combination of several multilayer stacks [37,38]. This limitation has been addressed with the development of omnidirectional dielectric reflectors (ODRs) which can be realized by augmenting the QWS condition discussed above with an additional set of conditions on the layer indices. First, the index contrast between the two dielectric materials needs to be adequately large and second, the index of the incident medium must be relatively small compared to that of the dielectric materials [39]. These structures can be viewed as one-dimensional photonic crystals, since they possess a 'complete' photonic bandgap (PBG) for light waves incident from the external medium. Analogous to the electronic bandgap in crystalline materials, photons that lie within the PBG of a photonic crystal cannot propagate through the

structure. Joannopoulos *et al.* has provided a complete analysis of the photonic crystal treatment of ODRs, including band structure [40].

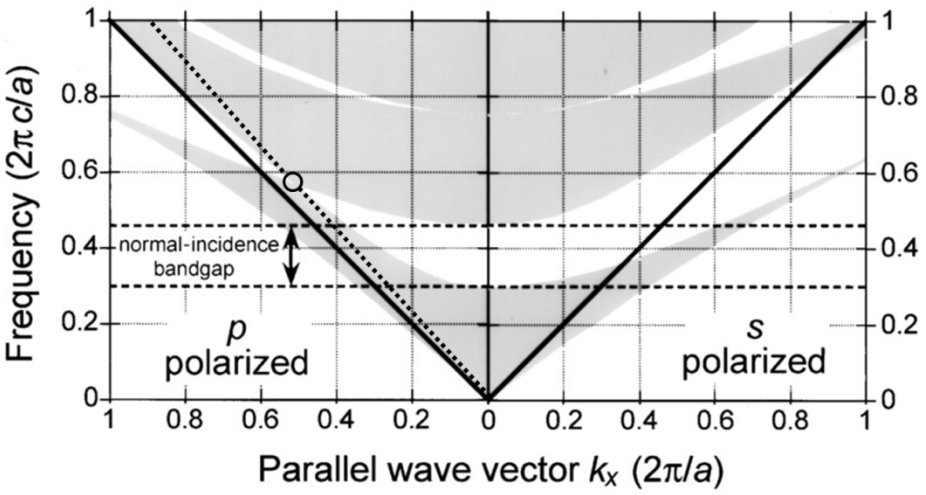

Figure 2.2 - Numerically solved band structure for a QWS with n_1 = 1 and n_2 = 2. Horizontal dashed lines indicate the bandgap at normal incidence. Solid diagonal lines are the light lines $\omega = ck_x$. Diagonal dashed line indicates the Brewster angle for p-polarized light. Circled region on the Brewster angle denotes the band overlap and collapse of the band gap. Adapted from [41]

To illustrate these structures, we will refer to the example in the previous section; a multilayer film, periodic in the y-direction, consisting of two materials with indices n_1 and n_2 and layer thicknesses d_1 and d_2 such that $a = d_1+d_2$. Figure 2.2 depicts the band structure of a quarter wave stack with n_1=1 and n_2=2, obtained using a numerical solution of the Maxwell's equations [42] for an incident electromagnetic mode in the x-y plane with wavevector **k**. Consider only the regions above the light lines, $\omega=ck_x$ (solid diagonal lines), thereby limiting the analysis to the case of plane wave propagation in the incident medium (assumed to be air n_i=1). The greyed regions indicate supported modes within the multilayer while the white gaps represent the forbidden regions. For a given angle of incidence, the PBG is the range of frequencies between the two grey regions. For example, the dashed horizontal lines indicate the PBG for normal incidence (k_x=0). It can be seen that the band gap vanishes (since the two grey regions overlap as

indicated by the circle in Fig. 2.2) for p-polarized light at a particular incident angle, indicating that there is no range of frequencies for which there exists a band gap. This overlap occurs at the Brewster angle, θ_b=arctan(n_2/n_1), in which case there is zero reflection for p-polarized light at the interface of the dielectric materials (indicated on Fig. 2.2 by the dashed diagonal line). By making the Brewster angle inaccessible to light originating from the incident medium, omnidirectional reflection can be achieved. By applying Snell's Law this condition can be expressed as:

$$\arcsin(n_i / n_2) < \theta_B. \tag{2.5}$$

Thus, by choosing dielectric materials with indices that are sufficiently larger than that of the incident medium, the Brewster angle becomes inaccessible [39].

Next consider a quarter wave stack structure with a larger index contrast, for example n_1=1.7 and n_2=3.4. Figure 2.3 depicts the band structure for this case, with the solid diagonal lines representing the light lines, the dashed diagonal line representing the Brewster angle and the dashed horizontal lines indicating the band gap at normal incidence. In this case a PBG can be seen to exist for both polarizations and at all angles of incidence. The width of the omnidirectional band gap is the range of frequencies between the open circle at normal incidence and the solid circle at glancing angles for p-polarized light.

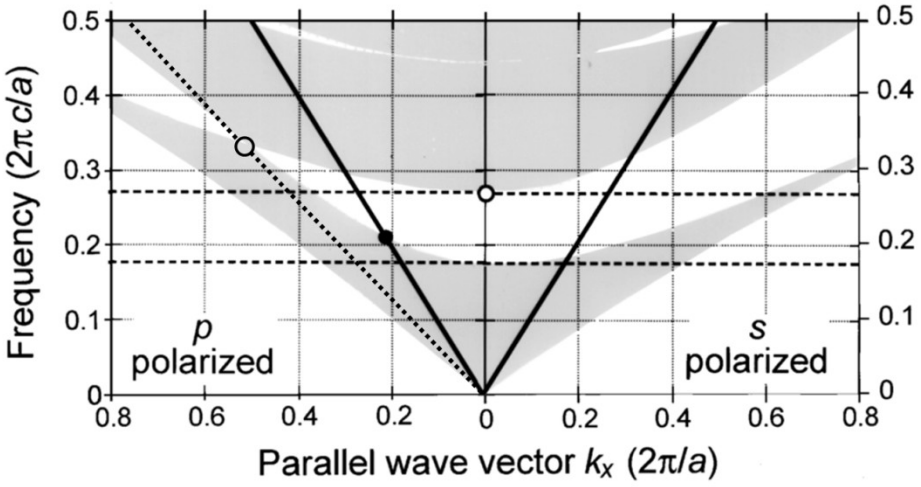

Figure 2.3 Numerically solved band structure for a QWS with n_1 = 1.7 and n_2 = 3.4 with the same conventions as Fig. 2.2. Adapted from [41]**.**

2.2.3 Hollow waveguides clad with DBRs

Let us now consider a hollow core slab waveguide clad with distributed Bragg reflectors. Due to fabrication limitations, perfect dielectric mirrors are a theoretical abstraction; there will always be losses due to surface roughness, finite number of layers, and layer absorption. In general, these structures can therefore be viewed as leaky dielectric waveguides.

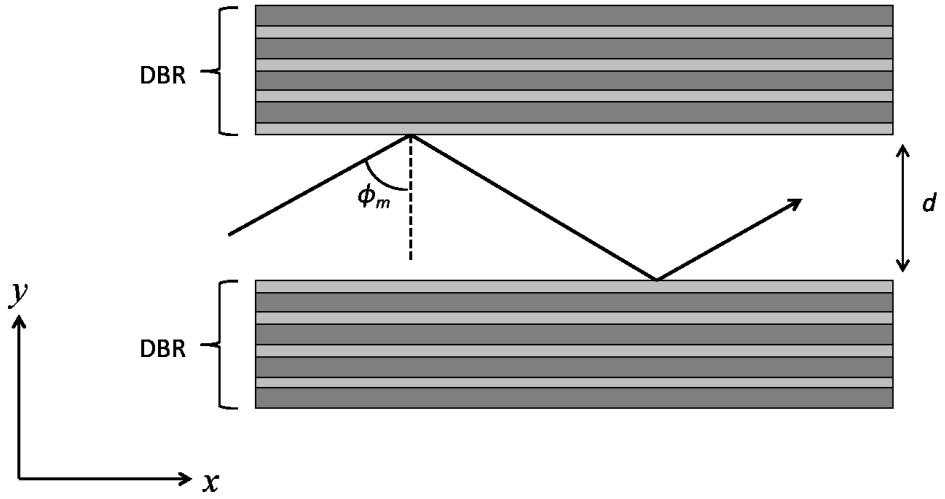

Figure 2.4 Ray optics illustration of a hollow waveguide clad with distributed Bragg reflectors.

With reasonable accuracy, these devices can be analyzed using a simple ray-optics model [29,43], as depicted in Fig. 2.4. Assuming hard boundary conditions the bounce angle for supported modes can be approximated as:

$$\cos(\phi_m) = \frac{m\lambda}{2d}, \tag{2.5}$$

where ϕ_m is the bounce angle for mode m, d is the core thickness and λ is the wavelength within the core medium $\lambda=\lambda_o/n$. In the case of perfectly reflecting mirrors the modes can be solved for using the phase-consistency equation [44]:

$$2k_x d - \Phi_T - \Phi_B = m \cdot 2\pi, \tag{2.6}$$

where Φ_T and Φ_B are the phase shifts on reflection due to the top and bottom mirrors, respectively. As mentioned previously, perfectly reflecting mirrors are a theoretical abstraction. Real waveguides will have sub-unity reflectance at the claddings. As such, a self-consistency condition for leaky modes is necessary, and can be expressed as [45]:

$$r_T r_B \exp(-j \cdot 2k_x d) = 1, \tag{2.7}$$

where r_T and r_B are the amplitude reflection coefficients of the top and bottom mirrors, for a given ray incident angle. k_x is the transverse propagation constant and must be complex to satisfy Eq. 2.7. Although analytic expressions exist for the amplitude reflection coefficients [46] they can be cumbersome to compute. Computational methods utilizing the transfer matrix method are best used to calculate these values [47,48]. Solving Eq. 2.7, one can determine the modal propagation constants as:

$$k_z = \sqrt{k_o^2 - k_x^2} = \beta_m - j \cdot \frac{\alpha_m}{2}, \tag{2.8}$$

where k_o is the free space wavenumber, β_m is the mode propagation constant, and α_m is the intensity attenuation coefficient. Taking into account the number of reflections that a guided mode undergoes per unit length, the attenuation coefficient can be estimated as [49]:

$$\alpha_m = -\frac{\ln(R_T R_B)}{2d \tan(\phi_m)}, \tag{2.9}$$

Where R_T and R_B are the reflectance of the top and bottom Bragg claddings for a given wavelength, λ_o, and incident angle ϕ_m. Furthermore, loss of the waveguide can be expressed in dB/cm as [30,50]:

$$\alpha \approx \frac{5\lambda}{d^2} \log_{10}(R_T R_B). \tag{2.10}$$

As expressed in 2.9 and 2.10, the loss scales logarithmically with the reflectance of the mirrors, indicating that low loss require that R_T and R_B are sufficiently large for the bounce angle of the particular mode. This implies that for low-loss guidance, rays associated with the guided mode must fall within the PBG of the cladding mirrors.

2.3 Thin film stress and defect formation

Fabrication of optical coatings, such as the distributed Bragg reflectors described above, relies on vacuum coating technologies and is subject to the capabilities and limitations of thin film deposition techniques. In this section we will look specifically at thin film stress, which can have profound consequences on multilayer structures.

2.3.1 Thin film stress

Thin film stresses, in general, fall into one of two categories: intrinsic and extrinsic stresses [51]. The former describes stresses that arise during film growth. These include, but are not limited to stresses caused by:

- incorporation of impurities
- surface and/or interface stress
- cluster coalescence
- grain growth, or grain boundary area reduction
- grain boundary relaxation
- vacancy annihilation

Extrinsic stresses, on the other hand, are stresses that arise from external influences after growth. Some examples include:

- temperature change, where materials with different coefficient of thermal expansion are employed
- chemical reactions

In the case of a thin film deposited on a substrate, the constraint of the substrate is the underlying cause of stress. The confined dimensions of the substrate prevent the lateral dimensions of the film from changing due to any process that would normally cause a volumetric change in the film [52]. This relationship between film, substrate and stress was examined by Stoney in 1909. He observed that a metal film deposited on a substrate was in a stressed state with no external forces applied and as a result this would bend the substrate. This relationship is expressed as Stoney's equation:

$$\sigma_f = \left(\frac{Y}{1-\nu}\right)\frac{d_s^2 w}{6R \cdot d_f} \tag{2.11}$$

Where σ_f is the film stress, for a film with Young's modulus Y, Poisson ratio ν, and thickness d_f on a substrate with thickness d_s and a radius of curvature of R. Many modern stress measurement systems rely on Stoney's equation to accurately determine thin film stress [51].

2.3.2 Buckle delamination of thin films

Films deposited under compressive stress, including many films deposited by sputtering, have been known to blister or buckle from their substrate [53]. In conventional electronics and optoelectronics this is a failure mode of fabricated devices. However, by controlling the regions over which a film buckles it has been proposed that these delaminations could form the basis for microfluidic channels and waveguides [30,54], as discussed further in Chapter 5.

Depending on conditions such as film stress, adhesion and thickness, the buckle delaminations can take on various morphologies. These include straight sided 'Euler columns' as well as telephone and varicose modes (see Fig. 2.5). The straight sided Euler modes are of particular interest for the optical applications discussed in Chapter 5. Thus we restrict the present discussion to the analysis of this morphology and to the conditions necessary for this mode to predominate. A detailed analysis of the telephone-cord buckles can be found elsewhere [55].

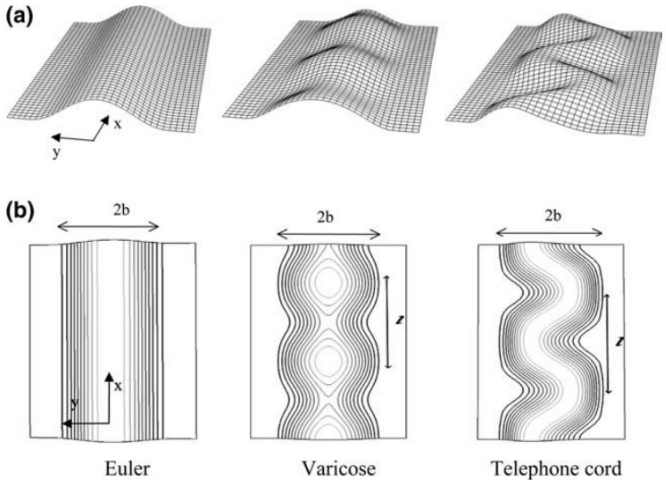

Figure 2.5 The geometry of a buckled plate of constant width clamped along it's edges. Adapted from [54]

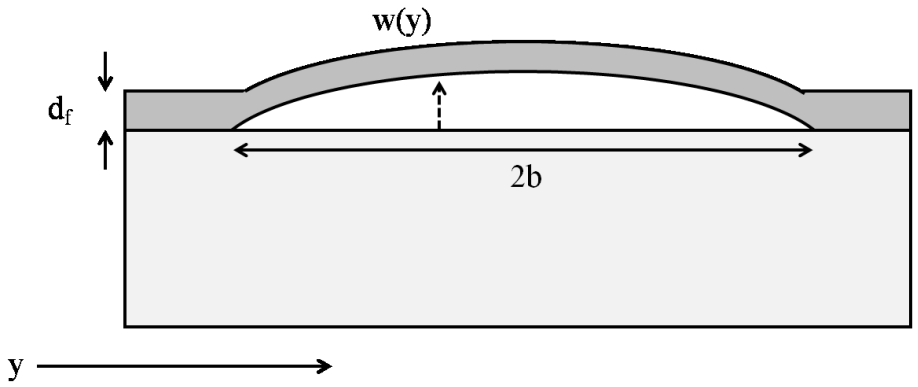

Figure 2.6 Cross sectional illustration of a Euler column of width 2*b*, thin film thickness d_f, and buckle height *w(y)*.

To analyze the Euler buckles, consider a thin patterned strip of width 2*b* such that the delamination buckle is confined to this region (see Fig. 2.6). The buckling behavior of a film under equi-biaxial compressive stress can be modelled as a plate of the same width that is rigidly clamped along its edges [51,54]. This approximation has been shown to be accurate in the limit that the Young's modulus of the substrate is no less than about one tenth of the film's modulus [56]. The critical compressive biaxial stress at the onset of buckling, σ_c, for the Euler mode over a region of width 2*b* is [54]:

$$\sigma_c = \frac{\pi}{12}\frac{Y_f}{1-\nu_f^2}\left(\frac{d_f}{b}\right)^2, \tag{2.12}$$

where Y_f, ν_f and d_f are the Young's modules, Poisson's ratio and thickness of the film respectively. The shape of the buckle is defined by:

$$w(y) = \frac{1}{2}w_{\max}\left(1+\cos\left(\frac{\pi y}{b}\right)\right), \tag{2.13}$$

where $w_{\max}$ describes the peak buckle amplitude. For a film with a specific compressive stress, σ_0, we can define the smallest half-width that will result in buckle formation, b_0, as

$$b_0 = \frac{\pi d_f}{2}\sqrt{\frac{Y_f}{3\sigma_0\left(1-\nu_f^2\right)}}. \tag{2.14}$$

The film stress and buckle width are then related as

$$\frac{\sigma_0}{\sigma_c} = \left(\frac{b}{b_0}\right)^2 . \tag{2.15}$$

The peak buckle amplitude depends on the ratio of the compressive stress of the film, σ_0, and the critical stress, σ_c, which in turn relates to the buckle width as

$$w_{\max} = d_f \sqrt{\frac{4}{3}\left(\frac{\sigma_0}{\sigma_c} - 1\right)} = d_f \sqrt{\frac{4}{3}\left(\left(\frac{b}{b_0}\right)^2 - 1\right)} . \tag{2.16}$$

It follows that in the range $b>>b_0$, Eq. 2.16 reduces to

$$w_{\max} \approx \frac{2d_f}{\sqrt{3}} \frac{b}{b_0}, \tag{2.17}$$

implying that the peak buckle height varies linearly with the buckle width. A plot of Eq. 2.16 can be seen in Fig. 2.7. The region of validity for linear approximation predicted by Eq. 2.17 is indicated on the figure.

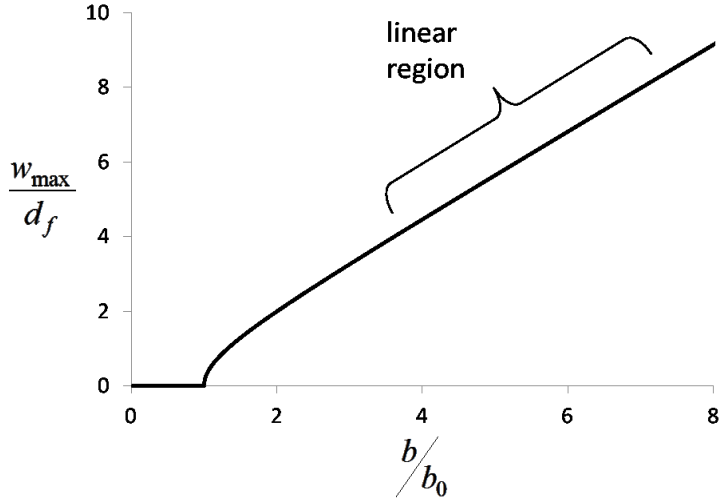

Figure 2.7 Plot of $w_{\max}/d_f$ compared to b/b_0. In the range $b>>b_0$ the relationship the relationship is approximately linear.

The above analysis is restricted to the symmetric Euler column. However, depending on specific conditions, the Euler column may become unstable leading to varicose or telephone-cord growth. Determining the specific ranges for stable Euler column growth was the subject of work by Moon *et al.* and Audoly [54,57]. It was found that when σ_0 is much larger than σ_c (or, equivalently, when b is much larger than b_0) the Euler mode becomes unstable and secondary buckling occurs to lower the energy of the buckled state. At this point the sides of the

delamination cannot remain straight and the secondary buckling manifests itself as axial undulation, or a wave-like pattern. The results are summarized in Fig. 2.8. For values of the film stress and critical stress such that $1 < \sigma_0 / \sigma_c < 6.5$ (or, equivalently when $1 < b/b_0 > 2.5$) stable Euler column growth was prevalent. For values where $\sigma_0 / \sigma_c > 6.5$, varicose or telephone cord buckles may form. The symmetric varicose mode only reveals itself within a limited range of variables, in particular, when $v_f < 2.5$ and $6.5 < \sigma_0 / \sigma_c < 7.5$. Whereas telephone cord modes are prevalent when $v_f < 2.5$ and $\sigma_0 / \sigma_c > 7.5$ or when $v_f > 2.5$ and $\sigma_0 / \sigma_c > 6.5$. Physical interpretation of these results is aided by Eq. 2.15; for a given film stress, σ_0, that is larger than the critical stress, σ_c, there exists a critical width where the loading on the delamination front is no longer uniform resulting in the secondary buckling that leads to the varicose or telephone pattern.

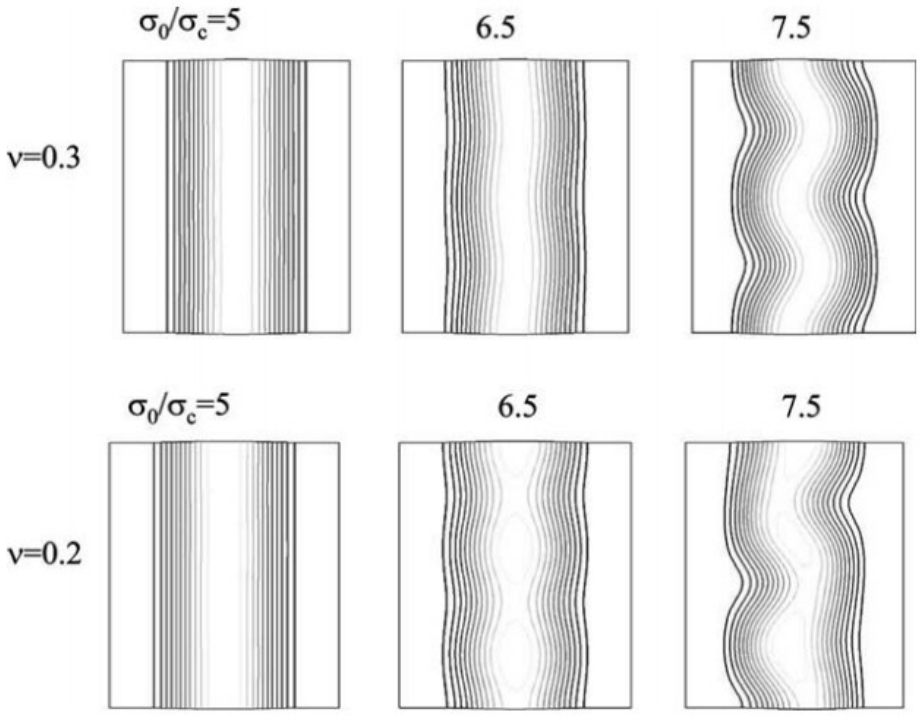

Figure 2.8 Contour plots of a buckled plate of constant width clamped along it's edges with three different stress ratios and two Poisson's ratio. For $\sigma_0 / \sigma_c < 6.5$ the Euler mode is dominant (left most column). For $\sigma_0 / \sigma_c > 6.5$ varicose (bottom middle) or telephone cord (right column and top middle) buckling occurs. Adapted from [54]**.**

Chapter Three: Tapered air-core channel Bragg waveguides

3.1 Introduction

This chapter details the work to design, fabricate and test air-core ridge waveguides based on a wafer bonding technique. In particular, these devices were designed to facilitate proof-of-concept fluorescence detection with the potential for integration within lab-on-a-chip (LOC) systems. The main building block is a tapered waveguide spectrometer which has been studied previously by the DeCorby group [7,28,58,59]. Initial results, as well as design limitations, are presented and discussed. This serves as a prelude to Chapter 5, where an alternative fabrication method based on controlled buckling is described. Portions of this chapter where published in *Frontiers in Optics 2014* [60].

3.2 Background and motivation

Recently, lab-on-a-chip (LOC) devices have attracted a large amount of academic research. These chips combine valves, pumps, mixers and channels to perform automated functions that would typically require a full-scale laboratory [12]. The advantages these systems offer are myriad, and include:

- Portability
- High sensitivity
- Reduced cost
- In situ analysis

Optical detection methods have many attributes that are attractive for LOC systems including high sensitivity, and high resolution, as well as being non-invasive and offering real time results. Typically, optical detection is accomplished using bulky off-chip components such as filters, microscopes, imaging systems and commercial spectrometers. In order to align with the goal of point-of-care-diagnostics, integrated (on-chip) optical sensing devices are of significant interest.

Fluorescence detection is widely used for biological and chemical analyses [61], and, as a result, techniques for fluorescence detection are highly developed and are the most common sensing modality in LOC and optofluidic microsystems [1]. Fluorescence systems typically employ filters to suppress excitation light at the detector, and to isolate the emission from one or more known dyes. While less common, the acquisition of spectrally-resolved fluorescence is a more powerful and flexible approach, which can enable the study of native fluorescence and provide insight into dynamic chemical and biological processes [62].

While many optical devices benefit from size reduction and integration, the implementation of chip-scale spectrometers remains a difficult challenge. Compact spectrometers can be realized by placing a linear variable filter (LVF) (ex. a tapered Fabry-Perot cavity) in close proximity to an image sensor [63]. However, the traditional LVF spectrometer has inherently low throughput and is not particularly compatible with point-source emitters. Schmidt *et al.* [64] proposed an alternative geometry that addresses some of these issues, by integrating a hollow waveguide adjacent to the wedge filter. However, that system requires that fluorescence be collected from a large volume or from a particle flowing at stable and uniform velocity.

We have previously described [7,28] an instrument that can be viewed as a side-coupled LVF, and which we'll subsequently refer to as a tapered waveguide spectrometer (TWS). These devices utilize omnidirectional Bragg reflectors as the claddings while the tapered core of the waveguide provides the dispersive functionality. Here, we describe preliminary experiments that illustrate the utility and advantages of the TWS for on-chip fluorescence spectroscopy in LOC systems.

3.3 TWS concept and design

A schematic illustration of the TWS concept is shown in Fig. 3.1. Light emitted by a small volume emitter (for example, a fluorescent particle) is collected into the hollow waveguide and is spatially dispersed for collection and analysis using an image sensor and signal processing techniques. A fluidic channel containing the liquid analyte would be closely integrated with the tapered waveguide to ensure efficient collection of the emitted signal.

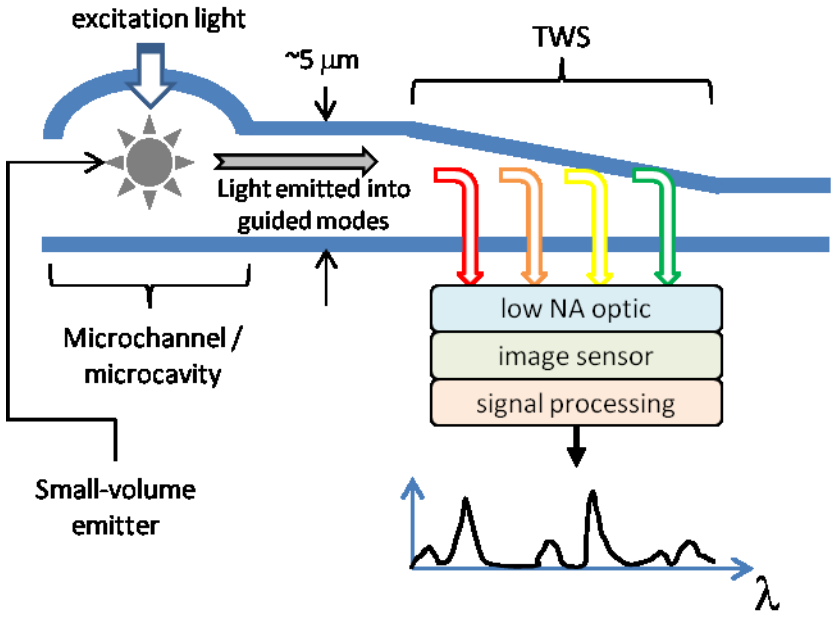

Figure 3.1 - Cross-sectional schematic of the proposed spectroscopy system. A fluidic channel would be closely integrated with the tapered waveguide spectrometer, to facilitate efficient coupling of the emission (ex. from a fluorescing particle) into the hollow waveguide modes.

One of the advantageous features the TWS possesses is its dispersion mechanism afforded by the tapered core. Consider a tapered slab waveguide clad with distributed Bragg reflectors. For wavelengths that lie within the omnidirectional band of the mirrors, light is well guided until the mode approaches its critical cut-off thickness. At this point, the mode effectively becomes a vertical cavity resonant mode. As discussed in Chapter 2, fabricated Bragg mirrors have sub-unity reflectance, and as a result the light at cut-off is partially radiated out of the waveguide in the near vertical direction (see Fig. 3.2(a)). Neglecting field penetration into the mirrors, the core thickness that corresponds to the critical cut-off thickness for mode *m* (resulting in the equivalent Fabry-Perot cavity) is given by:

$$d_c = \frac{m\lambda}{2}, \tag{3.1}$$

where λ is the free space wavelength. As expressed by Eq. (3.1), the cut-off position is wavelength dependent, allowing for the spatial dispersion of an input signal. Each unique spectral component of a polychromatic signal can then be extracted based on its unique cut-off

location. Wavelengths that undergo cut-off are subject to back reflection and standing wave formation in the proximity of d_c [7]. For wavelengths larger than the upper limit of the omnidirectional band (see Fig. 3.2 (b)) modes are guided poorly at the waveguide input and ultimately do not reach the detection point. For wavelengths shorter that the lower limit of the omnidirectional band (see Fig. 3.2 (c)) modes are guided well at the taper input. However, as the bounce angle becomes smaller, the guided modes begin to leak out at off-normal angles. These modes do not reach the vertical cavity resonance condition.

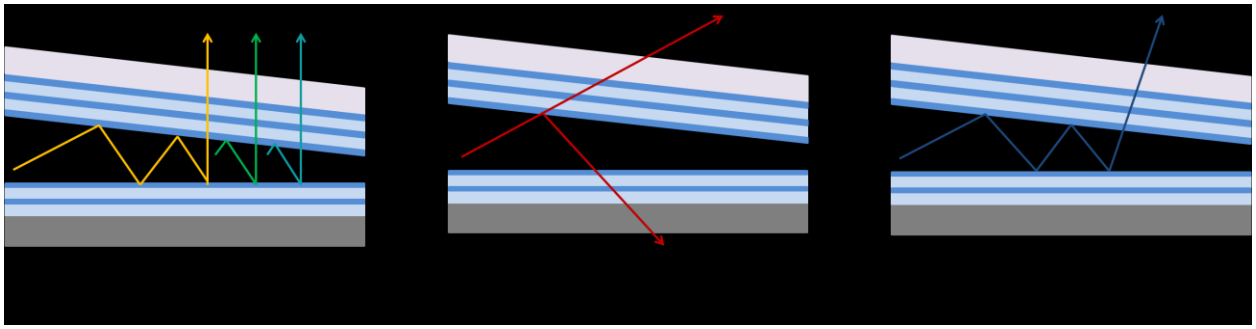

Figure 3.2 - A ray optics representation of guided light within a tapered air-core Bragg waveguide. (a) Guided modes within the omnidirectional band of the cladding mirrors are transformed into vertical cavity resonant modes which radiate outward in the near vertical direction. (b) Wavelengths that are longer than the upper limit of the omnidirectional band are poorly guided at glancing angles and leak out. (c) Wavelengths that are shorter than the lower limit of the omnidirectional band are guided well at glancing angles but begin to leak out as the bounce angle becomes smaller. A low NA optic at the detection point can filter out these wavelengths.

The off-normal radiation that is emitted through the structure from standing wave formation and out-of-band wavelengths (particularly at shorter wavelengths) can cause significant interference and cross talk problems. For use as a microspectrometer these effects must be reduced or eliminated. Some strategies to address this issue include using a low-NA optic at the detector location to suppress off normal light rays (see Fig. 3.1) or careful choice of taper profile. In the case of fluorescence sensing, careful design can ensure the wavelength of the excitation source lies outside the omnidirectional band of the DBRs so that when light is collected using a low-NA optic, is effectively filtered out of the vertically radiated spectrum.

For a taper spectrometer, where the off-normal radiation is suppressed, the wavelength resolution can be approximated as [7,28]:

$$d\lambda \approx \frac{Z_p}{D_T} + \frac{\lambda}{m\pi\left(\sqrt{R}/(1-R)\right)}, \tag{3.2}$$

where m is the vertical mode order (m=1,2,3...), Z_p is the effective detector array pixel size (accounting for magnification), and R is the normal incidence reflectance of the Bragg mirrors. The spatial dispersion, D_T, imparted by the taper is given by:

$$D_T \equiv \frac{\Delta Z}{\Delta \lambda} \equiv \frac{\Delta z}{\Delta d}\frac{\Delta d}{\Delta \lambda} \approx \left(\frac{1}{S_T}\right)\left(K + \frac{m}{2}\right), \tag{3.3}$$

where S_T is the absolute value of the taper slope, d is the air core thickness, and K is the phase shift coefficient accounting for field penetration into the cladding mirrors at normal incidence [65]. Furthermore, the free spectral range (FSR) can be expressed as:

$$\delta\lambda_{FSR} \sim \frac{\lambda}{m+1}. \tag{3.4}$$

Analogues to the properties of a diffraction grating, higher ordered modes offer enhanced spatial resolution and dispersion, but at the expense of reduced FSR. It should be noted that, depending on the material choice for the Bragg mirrors and geometry of the taper, the omnidirectional band can limit the operating range of the spectrometer, rather than the FSR [28].

In the description above, a slab model has been assumed. However, in many cases 3D confinement is preferred. To achieve optical confinement in the lateral direction, an effective index contrast can be induced by varying the core height to produce channels. Waveguides of this nature are commonly called rib or ridge waveguides.

Figure 3.3 depicts a ridge waveguide clad by DBRs. Using the effective index method [66], we can separate the structure into different regions corresponding to different core thickness (Fig. 3.3 (a)). Each region can then be approximated by an equivalent planar slab model that is used to obtain the effective index, n_{eff}, of the region. The ridge waveguide can thus be viewed as a slab structure composed of layers with effective refractive indices, n_{eff1} and n_{eff2}. For a guided mode, m, with bounce angle, θ_m, the effective refractive index in a slab waveguide with core thickness, d, can be expressed as:

$$n_{eff,m} = \frac{\beta_m}{k_0} = n_i \cos(\theta_m) = n_i \sqrt{1 - \left(\frac{m\lambda}{2d}\right)^2}\ , \tag{3.5}$$

where β_m is the mode propagation constant, k_0 is the free-space wavenumber and n_i is the refractive index of the core region (assumed to be air, $n_i = 1$). This expression illustrates that an increase in core thickness corresponds to an increased effective index. By designing the ridge thickness, d_1, to be larger than the cladding region, d_2, n_{eff1} becomes larger than n_{eff2} allowing lateral confinement of guided modes within region 1.

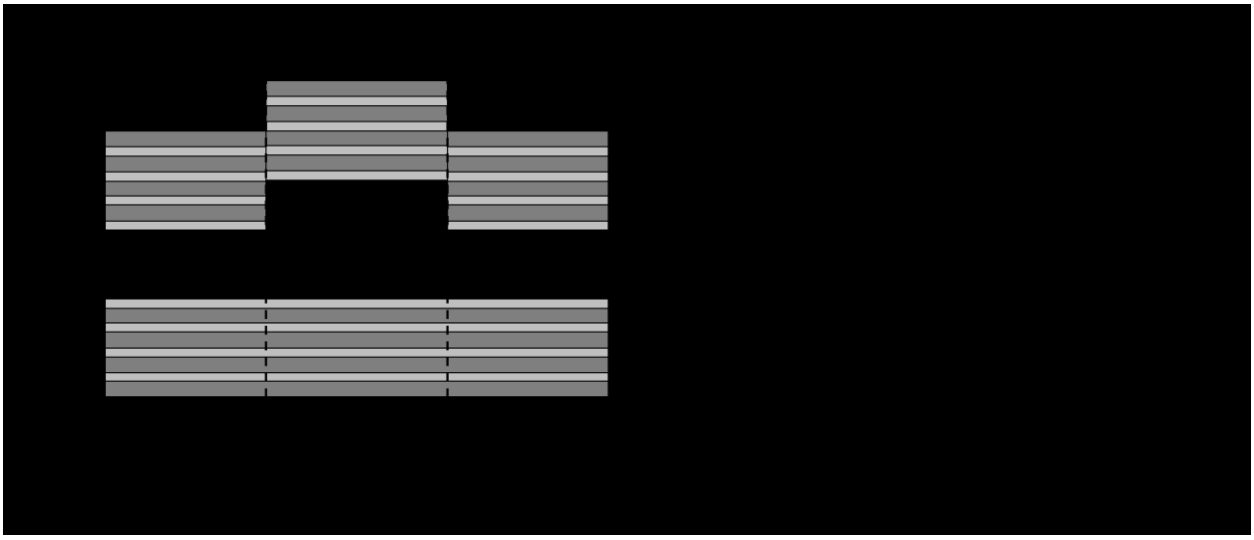

Figure 3.3 - Effective index model of a ridge waveguide clad with distributed Bragg reflectors. (a) Cross section of the ridge waveguide separated into region 1 with core height d_1, width w, and region 2 with core height d_2, where $d_1 > d_2$. (b) The ridge waveguide can be viewed as a composite slab waveguide with regions 1 and 2 having effective indices n_{eff1} and n_{eff2}, respectively.

Propagation within the core can be single or multi-moded, depending on the dimensions of the channel region. While intuitively, one would think that the single mode criteria would mirror that of an equivalent slab waveguide, it has been found that that is not the case [67,68]. In fact, it was found that the ridge waveguide may be multimode in the vertical direction, but under certain geometric conditions, it can only support one low loss mode. These conditions are expressed as:

$$t < \frac{r}{\sqrt{1-r^2}}, \tag{3.6}$$

$$r > 0.5, \tag{3.7}$$

where, neglecting field penetration into the claddings, $r \sim d_2/d_1$ and $t \sim w/d_1$, where w is the width of the ridge region. For a ridge waveguide that meets these conditions, only the fundamental mode in the ridge region has a propagation constant that is higher than that of the fundamental mode in the adjacent slab waveguide regions. This results in all modes of order $m > 1$ leaking out of the ridge region. For tapered ridge waveguides discussed above, there are inherent concessions that are made for single mode operation, namely a reduction in dispersion and resolution. This reduced versatility makes multimode operation preferred for the concept described.

The tapered waveguide based spectrometer described above possesses many key characteristics that make it particularly well suited for optofluidic and LOC analysis. The tapered channels provide in-plane collection of light from adjacent sources, the decomposed signal is delivered in the out-of-plane direction (vertical), inherently compatible with direction integration over a CCD or other image sensor, and lastly, the properties of the dispersive element (Bragg waveguide) can offer intrinsic filtering and suppression of excitation light at the detector, reducing the need for additional elements such as filters.

3.4 Fabrication

Proof-of-concept devices were fabricated using a wafer bonding method [28]. The general overview of the fabrication process is provided in Fig. 3.4. First, ridges are etched in a fused silica substrate using standard lithography and etching techniques. Next, a DBR is deposited on the etched fused silica substrate as well as a matching DBR on a silicon substrate. SU-8 posts are then patterned on the silicon substrate. Both substrate samples are then diced into appropriately sized chips such that the posts are positioned along one edge of the silicon chips. Lastly, diced pieces from the two substrates are bonded together, with the mirror surfaces facing one another. The posts run across the front edge of the chips and the etched channels run length-wise perpendicular to the posts along the chips perpendicular to the posts. In this way the posts prop up the fused silica substrate at one end forming a tapered slope. It should be noted that the wafer-

bonding technique described below was chosen specifically for its relative simplicity as a method to test the sensing capabilities of the prototype platform. As a result, direct integration with microfluidics or LOC devices would prove complicated and likely require a different fabrication method. Nonetheless, prototype devices fabricated in this fashion illustrate the utility of the concept. The detailed development of each step in the fabrication process is described below.

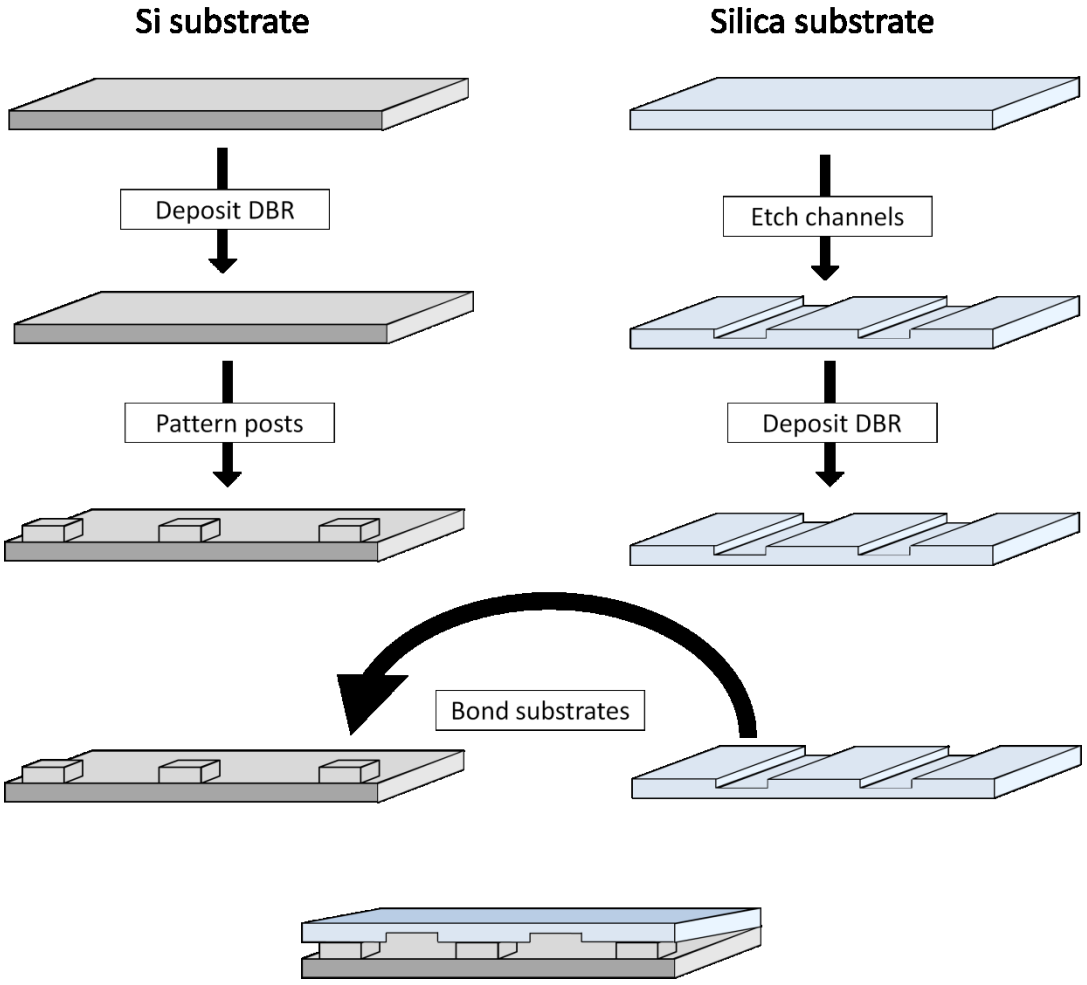

Figure 3.4 - Process flow for the fabrication of wafer bonded tapered Bragg waveguides. Separate silicon and silica substrates are used. Posts are patterned on one edge of the silicon substrate while channels are etched into the silica substrate. Both substrates are deposited with identical Bragg reflectors and bonded together, with the mirrors facing each other, such that the posts prop the silica substrate up on one end forming a linear taper.

3.4.1 Development of low loss DBRs

Previously the DeCorby group has fabricated low-loss DBRs in the near infrared using chalcogenide/polymer and Si/SiO_2 pairs [27,29]. For fluorescence detection, operation in the visible range is typically required and therefore different materials were needed. As discussed in Chapter 2, the operational characteristics (loss, bandwidth, etc.) of a Bragg waveguide are determined by the optical properties of the materials comprising the structure. Required attributes for the materials include:

- Low optical loss in the wavelength range of interest
- Large index contrast between materials
- Well understood and compatible deposition techniques

With these requirements in mind, TiO_2 and SiO_2 were chosen as deposition materials. TiO_2 has long been used in the optical coatings industry due to its transparency in the visible to near infrared region, high index (n~2.4), hardness, and excellent chemical and mechanical stability [33,69–71]. SiO_2 is the natural low index counterpart to TiO_2 and shares many of the desirable properties TiO_2 possess [33]. Due to the limited index contrast of the chosen materials, the photonic band gap is expected to be narrow. If only TE-polarized light is considered, however, the conditions for achieving omnidirectional reflection are relaxed considerably [41].

Extensive research has been performed into the various methods of deposition for TiO_2 including electron-beam evaporation [71], reactive sputtering (RF and pulsed DC) [70,72,73], and ion-beam assisted methods [74,75]. The properties of deposited TiO_2 films vary extensively depending on the exact deposition conditions. The relationship has been shown to be extremely complicated, with starting-material, substrate, pressure deposition rate, substrate temperature, etc. all playing significant roles [71]. Due to variances between deposition methods and machines, optimal processes must be developed in-house to suit a particular need.

Electron-beam evaporation is, in general, the most common deposition method for optical films, and in particular, TiO_2 [33,69]. Owing to this, and prior familiarity with local electron-beam systems, this was the deposition method chosen for the devices described in this chapter. A schematic of a typical electron-beam evaporation system is shown in Fig. 3.5.

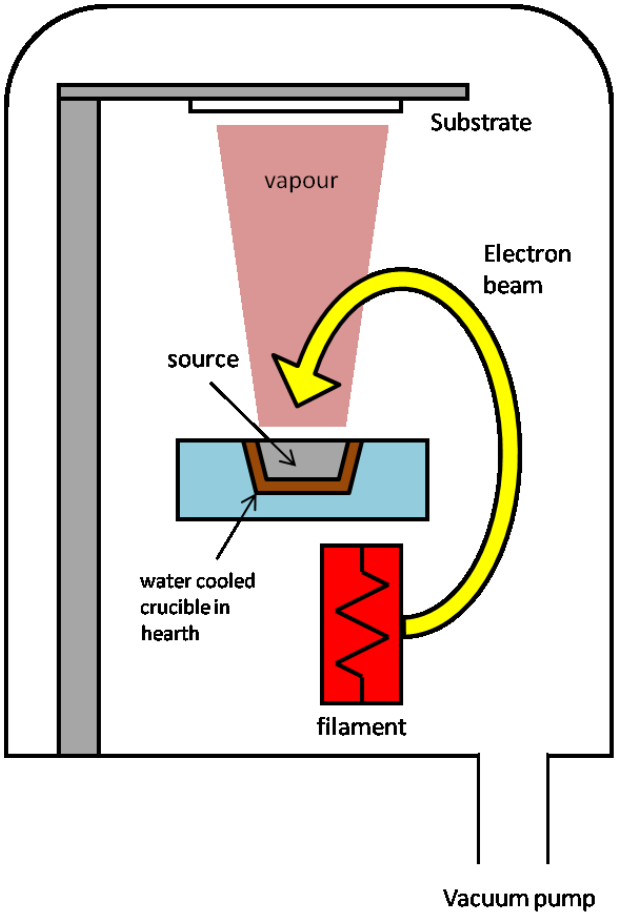

Figure 3.5 - Schematic representation of a typical electron beam evaporation deposition system. Using magnetic fields, an electron beam is guided onto the surface of the source material. The material evaporates or sublimates and the vapour is deposited on the substrate above.

Systems are generally housed in large chambers and connected to one or more vacuum pumps. A high energy electron beam is generated by a thermionic source, such as a tungsten filament, and directed toward the source material which is housed in a water cooled crucible. In general, the filament is kept out of the line of sight of the source material to prevent contamination. Strong magnetic fields are used to bend the electron beam so that it strikes the source material. The collision of high energy electrons with the source material rapidly raises the temperature of the source causing the material to evaporate or sublimate. The resultant vapour then condenses on the surface of the substrate, which is placed above the source material. Using modern technologies, the electron beam can be controlled to raster across the crucible in a

programmed pattern to create uniform melts. In order to prevent potential contamination between the source and crucible, the crucible must be made of a material with a higher melting temperature than the source.

An electron-beam evaporation system equipped with a 6-pocket hearth (MDC e-VAP 4000) was used for depositions. A mechanical roughing pump was used to reduce the pressure to ~500mTorr after which a cryo-pump was used to reach the base pressure of ~$5x10^{-7}$ Torr. Pressure was monitored using an ion-gauge sensor and two quartz crystal monitors are used for real-time film thickness monitoring. A programmable current sweep controller (MDC eVAP programmable X-Y sweep) was utilized to control the beam position. A particular advantage of this system was that no other users were accessing the system during the period of the fabrication. Seemingly minor changes to the chamber between depositions can produce inconsistent results from one deposition to another and is, by far, the biggest disadvantage of multi-user systems. Having nearly exclusive use of the system proved invaluable during the fabrication process.

Individual layers of TiO_2 and SiO_2 were initially deposited to calibrate the crystal monitors and to determine physical and optical characteristics to be used in the subsequent designing of the DBR. A 99.9% pure TiO_2 source (Lesker) was used for depositions. Depending on the degree of oxidation, TiO_2 sources vary from white in colour to near black. The particular source used for these depositions is black in colour, indicating an oxygen deprived source, although white sources have been used in the past. A tungsten crucible was filled approximately half full with 1-4mm sized pieces of the TiO_2 source and melted into a convex glob like shape. This process was repeated until the domed source material filled two thirds of the crucible (see Fig 3.6 (a)). This source preparation is extremely important to ensure high film quality. Any new TiO_x source will outgas and turn black once it has begun melting. During this process, the pressure of the e-beam chamber was observed to increase from $3.6x10^{-7}$ Torr to $5x10^{-5}$ Torr. A uniform domed melt indicates uniform outgassing, ensuring that the same oxygen content is present throughout the source and eliminating varying oxygen content in the subsequent films. A non-uniform melt may also contain air pockets which can rise to the surface of the melt and cause spitting, which in turn causes the deposition rate to vary [76].

(a) (b)

Figure 3.6 - Photographs of prepared e-beam sources in crucibles. The TiO_2 source (a) has been melted down into a domed shape to ensure uniform film properties. This process causes out-gassing resulting in a black material. The SiO_2 source (b) sublimates rather than melts. In this case the e-beam must be rastered across the source material to ensure uniform film properties.

Table 3.1 - Deposition parameters and film properties of e-beam deposited TiO_2 and SiO_2 monolayer films

Material	Base pressure (Torr)	Deposition Pressure (Torr)	Substrate temperature (°C)	Current	Deposition rate (nm/s)	n_{550}	k_{550}
TiO_2	$5.2x10^{-7}$	1.010^{-4}	300	0.13	0.068	2.39	$1x10^{-5}$
SiO_2	$3.3x10^{-7}$	$1.8x10^{-6}$	300	0.04	0.178	1.46	~0

Once the source material was properly prepared, the system was loaded with a piranha cleaned silicon wafer and pumped down overnight. A summary of the deposition parameters can be found in Table 3.1. As mentioned above, after the initial melt the TiO_2 source is oxygen deprived, and therefore requires an oxygen partial pressure to ensure stoichiometry. This was accomplished by introducing pure oxygen into the system by a valve located at the bottom of the chamber. The oxidation of the TiO_x vapour occurs on the substrate surface [33]. Due to the large distance between the oxygen valve and substrate, a high partial pressure ($1x10^{-4}$ Torr) of O_2 was necessary for the deposited films to ensure enough O_2 reached the substrate surface for the

oxidation to occur. The substrate was kept at a temperature of 300°C to encourage the oxidation of TiO_x at the substrate surface [77]. High temperature depositions have also been found to increase film density resulting in a higher index of refraction [69,71,76,78], an attractive attribute for maximizing the DBR stop-band.

The sample was allowed to cool to room temperature before subsequent venting and unloading. A contact profilometer was used to confirm the thickness of the film and determine the tooling factor for the crystal monitors. To test the optical properties of the film, a variable angle spectroscopic ellipsometer (VASE, J.A. Woollam) was used to scan the reflectance of the sample. From this, the VASE software can be used to fit the experimental reflection to various models. A Cauchy fit of the from

$$n(\lambda) = A + \frac{B}{\lambda^2} + \frac{C}{\lambda^4}, \tag{3.8}$$

was used where A, B, and C are fitting parameters. To account for absorption, an Urbach tail model was used:

$$k(\lambda) = \alpha e^{\beta\left(1240\left(\frac{1}{\lambda}-\frac{1}{\gamma}\right)\right)}, \tag{3.9}$$

where α and β are the amplitude and exponent factor, respectively and are used at fitting parameters and γ is the band edge. The optical properties of the TiO_2 monolayer are provided in Fig. 3.7 (a). along with the dispersion relation determined by Kim [79]. As expected, using a high substrate temperature produced films with high index, n_{550}=2.39 and low loss, k_{550}<1e-6 (see Table 3.1). Compared to the Kim model, the experimental index was found to be larger by ~0.08 over the visible wavelength region.

Monolayers of SiO_2 were deposited in much the same was as TiO_2. A copper crucible was filled approximately two thirds full of 1-5mm pieces of a 99.99% pure SiO_2 source (Lesker). Minimal source preparation is required for SiO_2, since the material tends to sublimate rather than form a uniform melt (see Fig 3.6 (b)). However, to ensure that a hole is not drilled through the source material, careful control of the beam location is required. Here, a small spiral pattern was used and manually moved across the crucible to ensure uniform source consumption. The complete summary of the deposition parameters can be found in Table 3.1. The deposition rate was verified using contact profilometer measurements of the film. The resultant Cauchy fit using

the VASE software can be seen in Fig. 3.7, with n_{550} = 1.46, comparing well to results previously reported by the group [28].

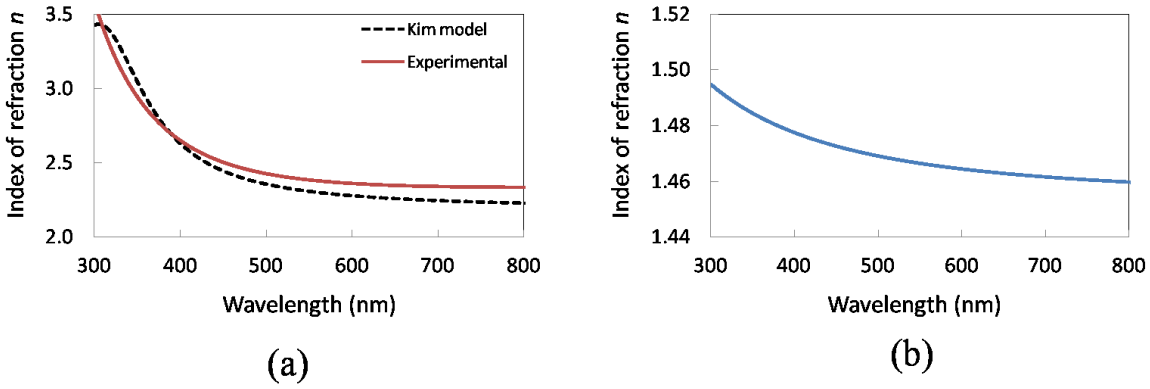

Figure 3.7 - Refractive index of electron beam deposited monolayers of (a) TiO_2 and (b) SiO_2. Results were obtained using a VASE measurement system and determined using Cauchy fits.

The optimized monolayer films were subsequently applied to the fabrication of DBRs. A 6-period TiO_2/SiO_2 multilayer at centre wavelength, λ_{Bragg} = 550nm, was deposited on a piranha cleaned silicon wafer. The system was pumped down overnight, achieving a base pressure of $3.2x10^{-7}$ Torr. The total multilayer stack was deposited at 300°C. The multilayer was allowed to cool to room temperature before venting and unloading. To predict the stop-band for the multilayer, transfer matrix simulations [47] were performed using the optical properties of the individual layers determined above. Peak reflectance for TE-polarized light at 550nm and normal incidence is predicted to be R_{550} = 0.996. The experimentally determined reflectance characteristics measured using the VASE system and the predicted stop-band are shown in Fig. 3.8. A stop-band (TE) spanning ~495-565 is observed, in close agreement with simulation.

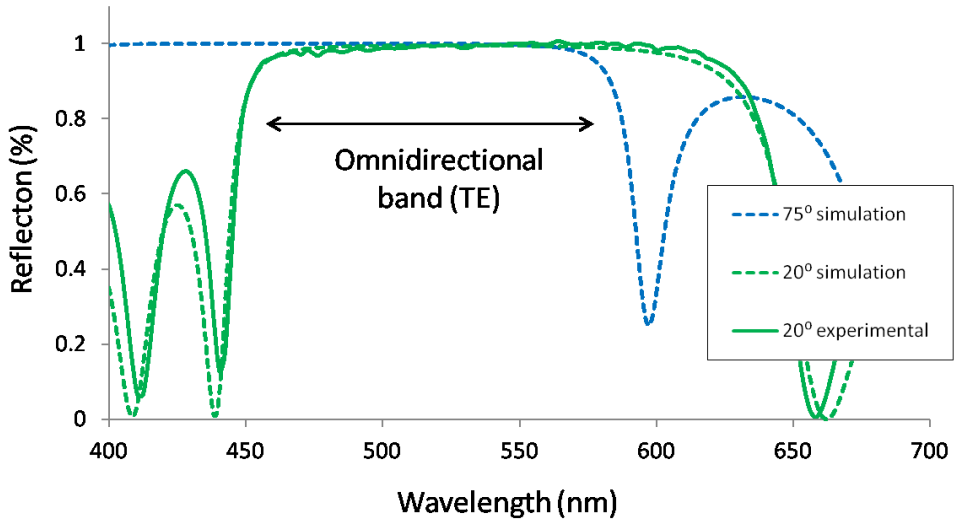

Figure 3.8 - Predicted (dashed lines) and experimentally determined (solid line) reflectance characteristics of the electron beam deposited 6-period TiO_2/SiO_2 mirror. Results are for TE-polarized light at 20^0 and 75^0 incident angles.

A contact profilometer measurement indicated a total thickness of ~888nm, in close agreement with the target thickness of 908nm. The ~2% discrepancy in thicknesses has been observed to be typical for large multilayers. Variations in the reflectance values are attributable to the slight variation in thickness, and to the fact that the model neglects details such as surface roughness and index gradients at the interface between layers.

A matching 5.5-period DBR was deposited on a fused silica substrate, which had been previously etched with arrays of channels with widths varying from 10µm to 80µm. The channels were etched to a depth of ~2.5µm using an inductively coupled plasma reactive ion etcher (ICPRIE- Alcatel, AMS110). Due to the change in substrate from silicon to fused silica the mirror was designed to start and terminate with the high index layer to increase the reflectance [33], resulting in the odd number of layers in the DBR.

3.4.2 Manual assembly

Following successful deposition of the DBRs, the wafers were cleaned using an acetone sonication bath and prepared for lithography. In order to create the required taper, a strip of posts must be patterned long the edge of the chips (see Fig. 3.4). SU-8 (Microchem), a photosensitive

polymer, was a natural choice as the material for patterning due to its chemical and mechanical stability and the extensive literature on the material due to its prevalent use in MEMS devices [80].

SU-8 is available in many different viscosities that can produce film thicknesses between 0.5-200μm. For the devices described above, a film thickness of ~5μm was desired to ensure multi-mode operation. In order to achieve the desired thickness, SU-8 2002 (% solids 29%) and SU-8 2010 (% solids 58%) were mixed to form a series of solutions of varying viscosities. The process involved adding the lower viscosity resist to a flask of the higher viscosity resist and gently rotating the flask. Care was taken to prevent bubble formation within the solution, which can be detrimental to the lithography process. Each mixture was spun cast at ~2000 RPM and processed to determine its median film thickness. Figure 3.9 (a) shows the film thicknesses of the various mixtures tested. From this curve, the mixture with a 2010:2002 ratio of 3:5 was selected for use. Further refinement of this mixture was performed, the resultant spin speed vs. thickness curve is shown in Fig. 3.9 (b). The lithography was performed on the silicon substrate DBR producing a post height of 4.6μm. A complete summary of the optimized process parameters performed on the DBR are provided in Table 3.2. The SU-8 posts were found to be slightly thinner than expected, a side effect of the reduced adhesion on the TiO_2 surface compared to the Si surface used for the optimization process.

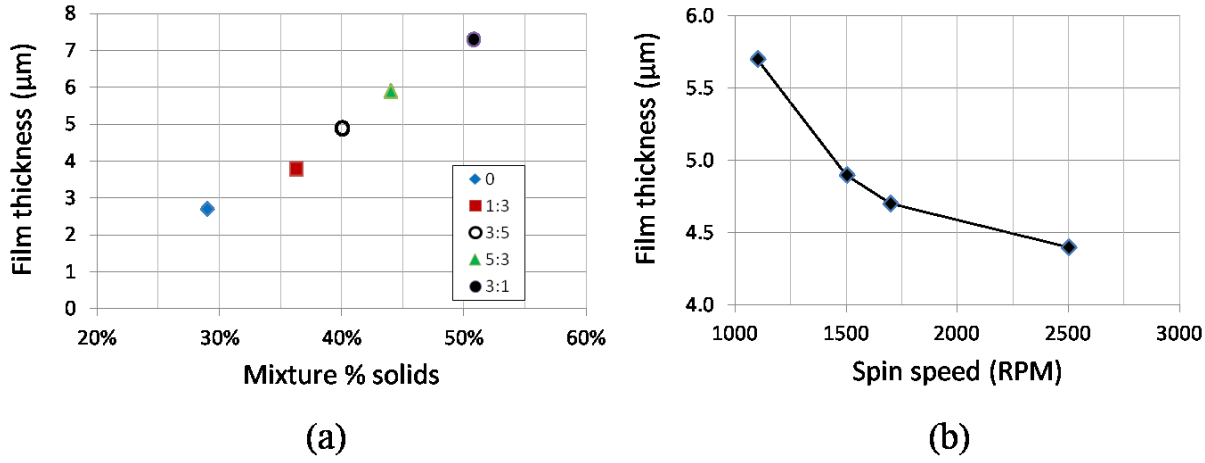

Figure 3.9 - Summary of SU-8 film preparation. (a) The median film thickness of various mixtures of SU-8 based on the estimated % solids present in each mixture. (b) The spin

speed vs. thickness relationship for a 3:5 mixture (~40% solids) of SU-8 2010 and SU-8 2002.

Both the silicon and fused silica substrates were then diced into chips of size ~4mm x 10mm with an array of SU-8 posts positioned along the edge of the silicon pieces (see Fig. 3.10 (b)). A coating of photoresist (HPR 504) was soft baked onto the substrates prior to dicing to protect the multilayer film from debris. This resist was removed using IPA after dicing. A silicon and a fused silica chip were then aligned on top one another, mirror surfaces facing one another, and clamped together. The SU-8 posts act to prop up the fused silica piece on one side (see Fig. 3.4) to produce an approximately linear taper with slop S_T = 1.15μm/mm. A UV curable epoxy (NOA 61) was then applied manually, using a needle tip, along the edges of the clamped chips to bond the two pieces together. A fully assembled chip is shown in Fig. 3.10 (b).

Table 3.2 - Optimized recipe for 3:5 mixture (~40% solids) of SU-8 2010 and SU-8 2002 used to fabricate posts of height ~4.6μm.

Step	Details
(1) dehydration	• 200°C for 300s
(2) Coating (RPM/time/acceleration)	• Spread: 500/5/5 • Spin: 1700/30/4
(3) Soft bake	• 65°C for 300s • 95°C for 120s
(4) Exposure	• 6.7s (105 mJ/cm^2)
(5) Post exposure bake	• 65 °C 240s • 95 °C 600s • 65 °C 60s
(6) Development	• 60s in SU-8 developer • 10s IPA rinse
(7) hard bake	• 200 °C for 300s

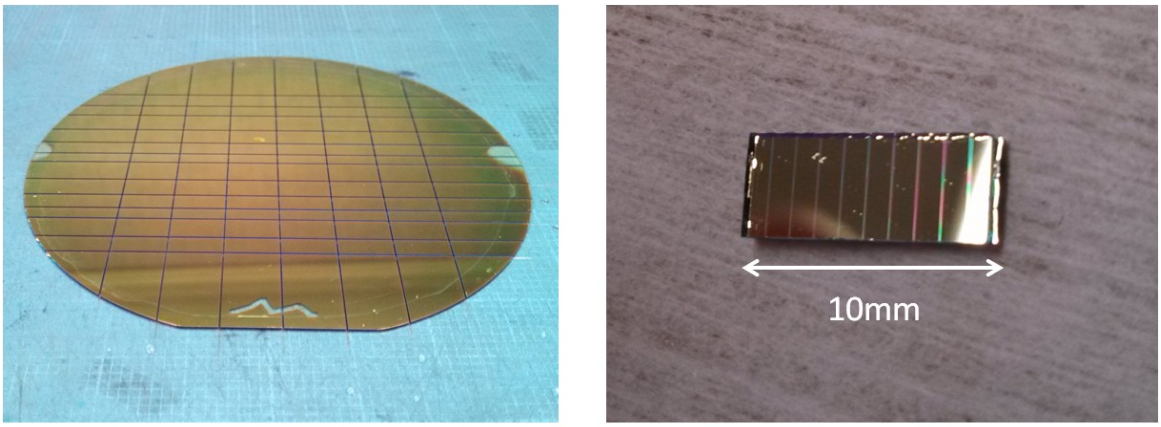

(a) (b)

Figure 3.10 - (a) Image of the quartz wafer following dicing. The protective layer of photoresist is present on the sample. (b) Fully assembled tapered waveguide. The etched channels are visible as narrow vertical lines.

3.5 Results

To characterize the devices a 532nm laser source, 543nm laser source, and broadband super-continuum source (Koheras SuperK Red) were utilized. The sources were either fibre coupled or free-space coupled to the wide end of the tapered channels. In the latter case, an objective lens was used to focus on the taper input. A CCD camera (Coolsnap ES, Photometrics) affixed with a low NA optic (Edmund optics, 0.7x - 4.5x with NA < 0.9) was adjusted above the chip to collect the out-of-plane radiation pattern from the channels. The general experimental setup is shown in Fig. 3.11.

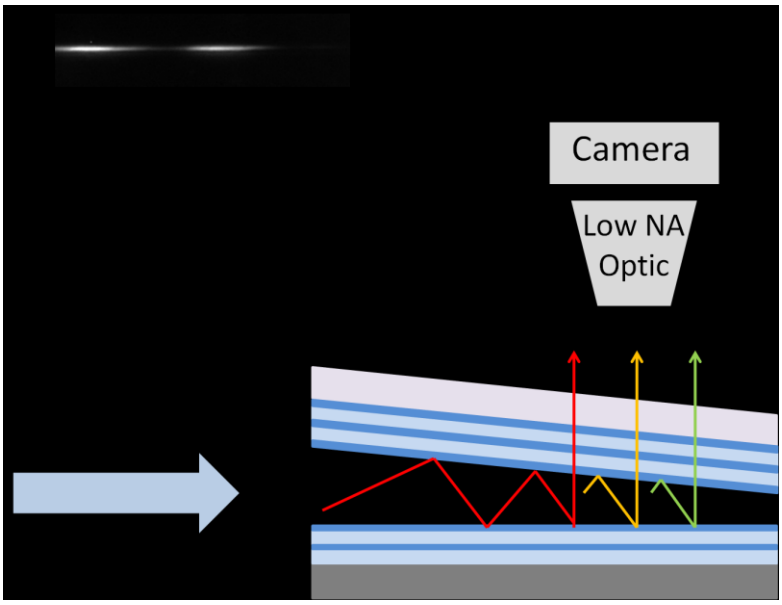

Figure 3.11 - Schematic of the general experimental setup. An example of a typical radiation streak emitted from a tapered channel (inset) is provided.

3.5.1 Resolution

The two green laser sources were used to determine the experimental resolution of the device. The lasers were launched in the wide end of the tapered channels and images were taken of the out-of-plane radiation of the lowest ordered modes. Figure 3.12(a) depicts the resultant radiation pattern from the 543nm source. Cut-off for modes guided in the channel can be seen as dots while cut-off for light guided in the slab region is seen as bright lines. Imaging software was used to determine the pixel intensity along the channel region which facilitated plotting the pixel intensity versus distance (see Fig. 3.12 (b)). Column-wise pixel averaging was employed to reduce noise, and the images were scaled using photolithographic features of known size. The experimental resolution can be determined from the FWHM of the laser dots as $d\lambda \sim dz / (\Delta z/\Delta\lambda)$ [28], where dz is the FWHM of the laser dot, Δz is the distance between the peaks of the laser sources, and $\Delta\lambda$ = 11nm is the wavelength difference between the lasers. Figure 3.12(b) depicts the pixel intensity versus distance along the channel for mode m=8 with $d\lambda$ estimated as 1.5nm. Equation (3.2) predicts a resolution of 0.30nm mode m=8. The discrepancy between experimental results and theory is a result of several factors. Namely, the theoretical result assumes a reflectance of 0.996, which neglects surface roughness and index gradient at the

transition between layers. The model also neglects to incorporate standing wave effects which act to broaden the radiation pattern near cut-off [7]. This broadening can be observed in Fig. 3.12(b) where, although a low NA optics is used, secondary peaks are present on the left of the primary peak. Nonetheless, as predicted by Eq. (3.2) resolution was found to improve with mode order where $d\lambda$ = 0.9nm for mode m=10.

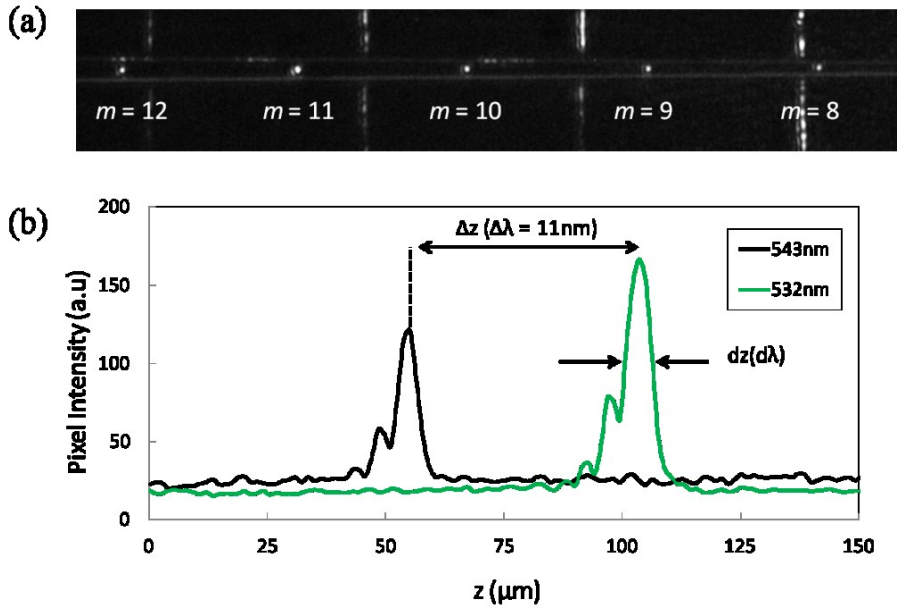

Figure 3.12 - (a) 543nm laser light radiated in the near-vertical direction from the taper and collected using a low NA optic and CCD camera. Bright dots along the tapered channel indicate cut-off positions for the laser. Cut-off modes in the slab region are also visible as bright lines outside the channels. (b) Column-wise pixel averaging of mode, *m* = 8, for 532nm and 543nm laser light within the channel region. A low NA optic was used, however, secondary peaks to the left of the primary, indicating standing wave formation and back reflectance, are still present.

3.5.2 Operating Range

As mentioned previously, the devices have a finite operating range that is limited by the width of the stop-band or the FSR. Chips were fabricated with 4.6μm SU-8 posts and an channel etch depth of 2.5μm. At the narrow end of the taper, assuming no gap, the etched channels limit the minimum core thickness possible. In the case of the fabricated chips, an etch depth of 2.5μm yields ~9 vertical modes, producing a limited FSR of ~55nm for 550nm light. Using transfer

matrix simulations, the omnidirectional band is expected to span ~70nm indicating that the fabricated devices have an operating range limited by the FSR. Figure 3.13 shows the light from the super-continuum source radiating from the taper. As evident from the image, there does not appear to be distinct modes present in the channel indicating mode overlap, and confirming the FSR limited operating range.

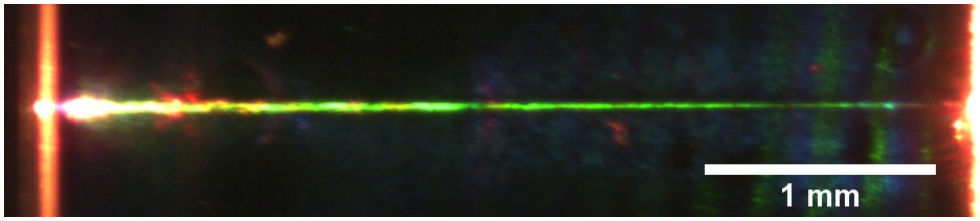

Figure 3.13 - Image of a ~4mm long tapered channel illuminated with the super-continuum source. The bright spot on the left indicates the wide end of the taper, while the bright edge on the right indicates the narrow end. It is expected that m=8 is the lowest ordered mode undergoing cut-off in the channel region. As a result, the modes from the broadband source overlap creating a uniform green streak. In contrast, there are several isolated modes in the slab region above and below in the tapered channel due to the decrease in core height.

Attempts were made, however, to determine the spectral response of the chips by analyzing the modes in the slab region which have a vanishing core thickness. In brief, the 543nm and 532nm lasers were launched into the slab region of the tapered waveguide and their cut-off positions recorded. This allows pixel-to-wavelength mapping along the length of the taper enabling the extraction of the spectrum of the broadband source. In this case a white LED (Digikey) was coupled to the wide end of the taper and the m=2 mode was analyzed. The raw spectrum of the LED extracted from pixel-to-wavelength mapping of the taper is depicted in Fig. 3.14(a). The shape of the LED spectrum obtained from using a commercial spectrometer (Ocean Optics, USB4000) is plotted for comparison.

As for any spectrometer, the 'instrument response' of the taper must be considered. Complete calibration of the extracted spectrum must take into account both the taper response and the collection optics and image sensor. The 'instrument response' in the case of the tapered spectrometer devices can be modeled as a correction factor defined as:

$$C(\lambda) = \frac{S_c(\lambda)}{S_T(\lambda)}, \tag{3.8}$$

where $S_c(\lambda)$ is the reference spectrum and $S_T(\lambda)$ is the raw spectrum obtained from the pixel-to-wavelength mapping of the source. Using the spectra from Fig. 3.13(a) the experimentally determined correction factor is presented in Fig. 3.14(b). The operating bandwidth spans ~500nm - 570nm, in close agreement with the expected TE-polarized stop-band determined from the mirror properties. The device has a relatively flat response between ~510-550nm with peak sensitivity at ~530nm.

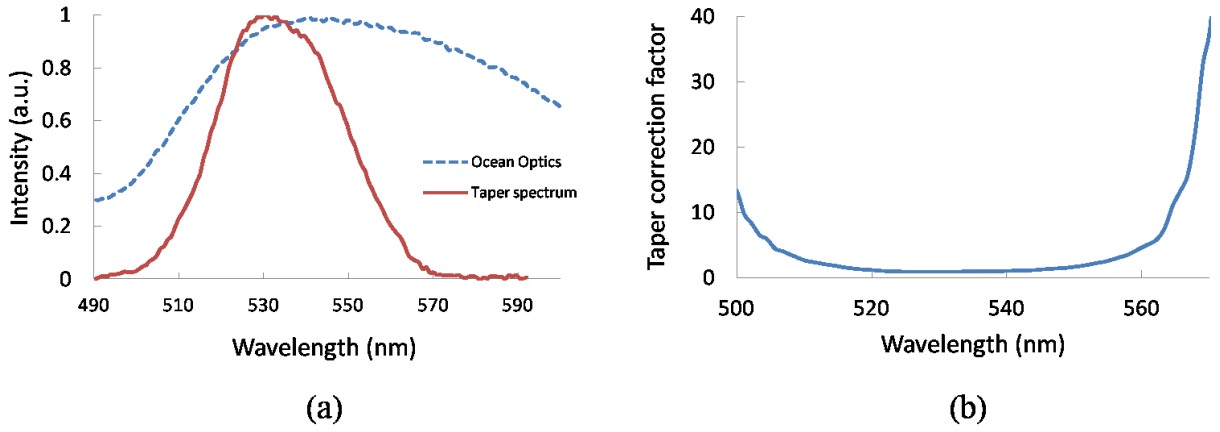

Figure 3.14 - (a) Spectrum of the white LED (solid line) radiating in the near-vertical direction from the taper using pixel-to-wavelength mapping. The shape of the LED spectrum obtained using a commercial spectrometer (dashed line) is included for comparison. (b) Resultant correction factor for the tapered waveguide obtained from the LED source.

3.5.3 Fluorescence sensing

To assess the fluorescence sensing capabilities of the prototype, a thin film of fluorescent microspheres (Fluospheres, Invitrogen) were deposited on a glass slide and positioned at the wide end of the taper. A focused 474nm laser was used to excite a small area of the microsphere film, whose emission was directed into guided modes in the tapered channels. To cover the operating range of the tapers yellow-green Fluospheres (505nm excitation, 515nm peak emission) and orange Fluospheres (540nm peak excitation, 560nm peak emission) were tested. The characteristic radiation streaks for modes *m*=8,9,10 of the yellow-green and modes *m*=8,9

for the orange Fluospheres are depicted in Fig. 3.15(a,b). Using the same imaging setup described above, and wavelength calibration technique using the 532nm and 543nm lasers, pixel-to-wavelength mapping of the emission of the microspheres was performed with the raw spectrums depicted in Fig. 3.15(c,d). The spectrum of the microsphere films obtained using a commercial spectrometer, and for the same excitation conditions, is also plotted for comparison.

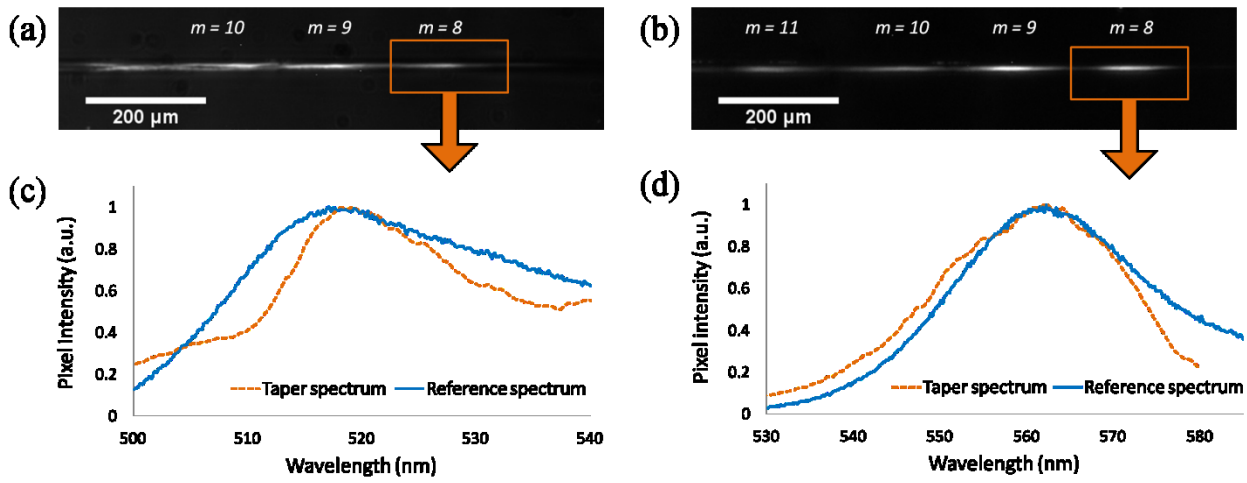

Figure 3.15 - Characteristic out-of-plane radiation streak of (a) yellow-green and (b) orange fluorescent microspheres captured by low NA optics and CCD camera. (c,d) The resultant spectrums of the *m* = 8 modes, extracted from the taper using pixel-to-wavelength mapping by the known cut-off positions of the 532nm and 543nm laser lines. Reference spectrums of the microspheres obtained using a commercial spectrometer are shown for comparison.

The raw data from the tapers for the 505/515 Fluospheres follows the general trend of the reference spectrum, with peaks matching closely. The discrepancy between spectra at the short and long wavelength side is due to the limited FSR of the m = 8 mode analyzed (FSR~60nm). For example, λ = 500nm of mode m = 8 overlaps with λ = 545nm of mode m = 7 where the Fluosphere has appreciable emission. Raw data from the tapers for the 540/560 Fluospheres also follows the general trend of the reference spectrum. Discrepancies on the right at long wavelengths are due to the limited operating range afforded by the DBR's. As mentioned above, the operating range at long wavelengths is limited to ~570nm. This aligns closely to the discrepancies observed for λ>570nm in Fig. 3.15(d).

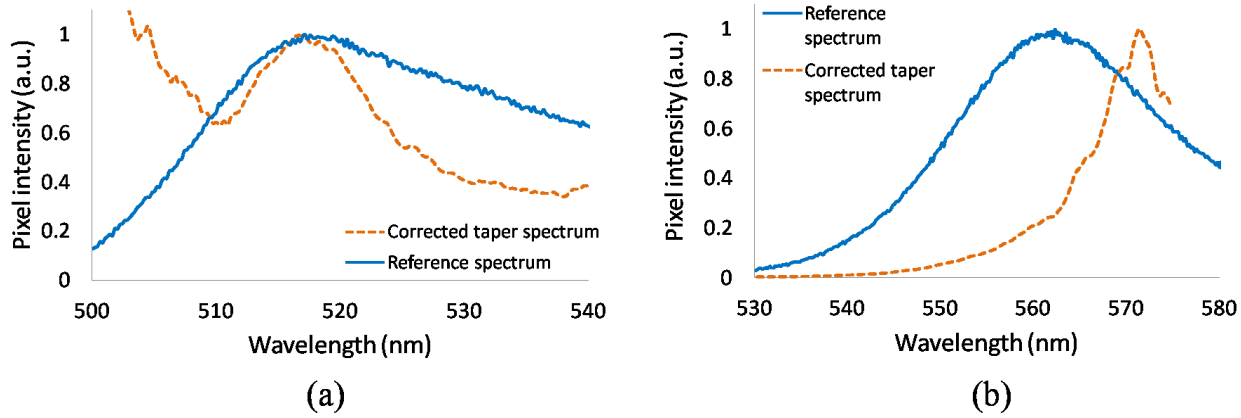

Figure 3.16 - Corrected taper spectrum of the m = 8 modes for the (a) yellow-green and (b) orange fluorescent microspheres. Near the edges of the operating range where the correction factor changes rapidly, or where significant mode overlap occurs, the spectrum begins to diverge. Reference spectrums of the microspheres obtained using a commercial spectrometer are shown for comparison.

In an effort to improve the spectrums extracted from the taper, the correction factor determined from Eq. (3.8) and presented in Fig. 3.14(b) were applied to the raw spectrums of the Fluospheres. The resultant spectrums are presented in Fig. 3.16. Results from the yellow-green Fluospheres shifted to shorter wavelengths, aligning more closely with the peak from the reference spectrum collected using the commercial spectrometer. Discrepancies close to λ = 500nm are the result of the proximity to the operating range limit where the correction factor beings to vary rapidly. The corrected spectrum for the orange Fluospheres shifted to longer wavelengths and proved to be a poorer fit to the reference spectrum. At long wavelengths near the edge of the operating range, λ = 570nm, the taper correction factor begins to change rapidly resulting in the dramatic shift of the taper spectrum to longer wavelengths. This is compounded by mode overlap at this range where λ = 570nm of mode m=8 overlaps with λ = 525nm of mode m = 9 where the Fluosphere has non-negligible emission.

3.6 Conclusions

Prototype spectroscopic sensing devices were fabricated and their fluorescence sensing capabilities were tested. With the use of low-NA collection optics, resolution as low as 0.9nm

was achieved within an omnidirectional band of ~70nm. Emission from two types of fluorescent microspheres were coupled into the devices and the spectrum extracted. Raw spectra agreed reasonably well with those collected from the sources using a commercial spectrometer. Results deviated from the reference spectrum close to the edges of the operating range of the TWS, and where significant mode overlap was present as a result of limited FSR. In an attempt to improve the extracted spectra, a correction factor was applied to remove the 'instrument' response of the system. The correction factor improved the taper response within the operating range, however, results began to deviate rapidly close to the edges of the taper operating range and where mode overlap was obvious. As a result, the correction factor is only reliable in ranges where there is no overlap between adjacent modes and for wavelengths that are well within the device operating range. To improve the operating range it is necessary to use more complex multilayer systems, or higher index contrast material combinations such as GaP and SiO_2 [81]. The limited FSR can be addressed by reducing the etch depth of the ridge region and reducing the SU-8 post height. In order to realize a fully integrated solution, compatible with microfluidics, an alternative fabrication method, such as controlled thin film buckling discussed in Chapter 5 and 6, is likely a more promising approach.

Chapter Four: Air gap resonant tunneling bandpass filter and polarizer

4.1 Introduction

This chapter describes the application of the wafer-bonding technique used in Chapter 3 to the fabrication of a bandpass filter and polarizer. While not directly related to hollow waveguides, the bandpass filter employs many of the concepts discussed in Chapter 1 along with the fabrication techniques detailed in Chapter 3 (bonding) and Chapter 5 (sputter deposition). The device is based on resonant tunneling through an air layer in the frustrated total internal reflection regime. Experimental results are reported for Si/SiO_2-based devices exhibiting a polarization-dependent pass band with bandwidth on the order of 10 nm in the 1550 nm wavelength range, peak transmittance on the order of 80%, and optical density greater than 5 over most of the near infrared region. The contents of this chapter were published in Optics Letters [82].

4.2 Background

Band-pass filters (BPFs) are essential components in many branches of optics and photonics [83]. A BPF is characterized by its pass-band shape and spectral bandwidth, peak transmittance (i.e. insertion loss) within the pass-band, polarization dependence, out-of-band rejection (often expressed in terms of optical density, OD), and out-of-band blocking range [33]. With the recent development of laser-based supercontinuum sources [84], there is an emergent need for BPFs that provide high power-handling capability and good rejection over the ~400 to ~2500 nm wavelength range. Ideally, the filter should also maintain the beam characteristics of the input light in both reflection and transmission [85].

Conventional BPFs are thin-film Fabry-Perot (FP) cavities with dielectric quarter-wave-stack (QWS) mirrors, and are designed to operate at near-normal incidence. Filters with multiple-coupled-cavities [33] are of great commercial importance, because they can provide an improved pass-band shape (e.g. a flat top) and superior out-of-band rejection in the wavelength regions adjacent to the pass-band. However, the inherent blocking range of any FP filter is

limited to the stop band of its QWS mirrors. Monolithic filters with extended blocking range can be implemented, but usually involve a complex thin film stack with an extremely large layer count [86]. To avoid this complexity, commercial FP filters are sometimes packaged with discrete blocking filters. In a typical implementation, separate filters for short wavelength blocking (e.g. colored glass filters) and long wavelength blocking (e.g. metal-dielectric filters [87]) are combined in a single enclosure with the BPF, using epoxy bonding techniques. The absorptive nature of these blocking filters can be problematic for applications that involve high power densities.

Frustrated total-internal-reflection (FTIR)-based BPFs, with one or more tunneling layers, had been extensively studied by the late 1960s [88]. One of their main attributes is excellent out-of-band rejection over a wide blocking range. Fundamentally, this derives from the fact that TIR conditions are essentially wavelength-independent (i.e. a TIR interface can behave as a very broadband mirror). However, some properties of tunneling filters, such as their large polarization and angular dependences compared to conventional FP filters, were historically viewed as fatal flaws [88]. Furthermore, the traditional use of solid tunnel layers such as MgF_2 or SiO_2 necessitates high-index coupling prisms, inconveniently high angles of incidence, and large substrates, resulting in high scattering loss and significant pass-band broadening due to spatial convolution effects arising from film non-uniformities.

It is important to note that much has changed since the early work on tunneling filters. With progress in techniques such as ion-beam sputtering, dielectric thin film stacks can now be deposited with extreme thickness accuracy and vanishingly small absorption and scattering losses [89]. Also, with the emergence of laser-based supercontinuum sources characterized by low beam étendue [84], an angular dependent response is less problematic in some applications, and can even be exploited as a tuning mechanism [90]. Finally, as discussed by Li *et al*. [91], the use of an air tunneling layer makes it possible to employ standard glass coupling prisms and convenient incident angles near 45 degrees, while, however, introducing a new set of fabrication challenges. Here, we describe a design procedure and experimental results for a BPF based on a single embedded air layer. Due to a large admittance contrast at the air layer, these filters can be designed to provide a polarization-dependent pass-band and strong rejection of the orthogonal polarization over a very wide range.

4.3 Device details

The proposed filter structure is illustrated in Fig. 4.1(a). A central air layer is embedded between two nominally identical thin film stacks, comprising alternating layers of two relatively transparent and high-refractive-index-contrast materials. Here, we use amorphous silicon (a-Si) and SiO_2, which provide a transparency range from ~900 nm to ~2500 nm, but other material combinations are possible. As depicted in Fig. 4.1(b), the thin films are typically quarter-wave-stack (QWS) Bragg mirrors at a specified angle of incidence, terminated with non-quarter-wave 'phase matching' layers adjacent to the air gap. Light is incident onto the filter structure at some angle (θ_{in}) that would normally result in TIR, and thus the fields are evanescent inside the air layer. As shown below, with proper design of the thin film multilayer stacks, efficient transmission can nevertheless occur within a narrow range of wavelengths and for a particular state of polarization.

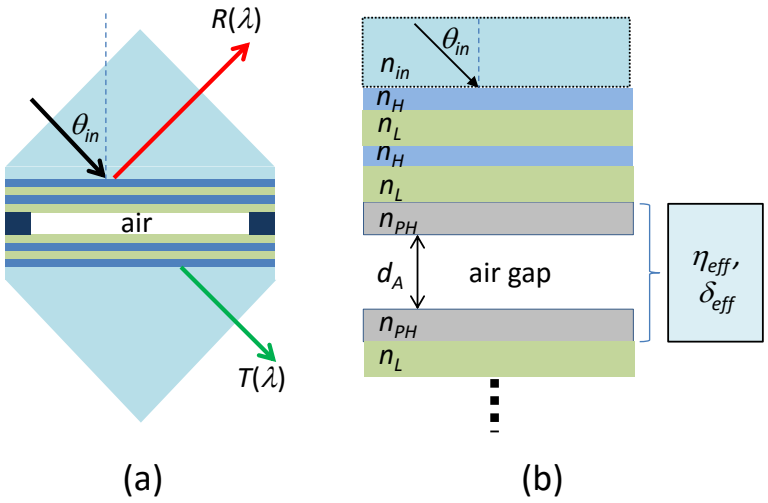

Figure 4.1 - (a) A schematic diagram of the air-gap tunneling filter is shown. The air-gap is sandwiched between nominally identical thin film stacks. (b) A more detailed view of a representative thin film structure is shown, where $n_{PH} = n_H$ or n_L. The central three layers including the air gap can be replaced by a single layer with wavelength-dependent effective admittance η_{eff} and effective phase thickness δ_{eff}.

Alternative but complementary theories can be invoked as the physical basis for the band-pass transmission. From one point of view [92,93], the pass-band is associated with

resonant tunneling mediated by surface states [46] at the air interfaces. Since each interface of the air gap supports a surface state, the transmission band can be made to resemble that of a traditional dual coupled cavity filter [33], with a flat top and relatively steep pass-band edges. Alternatively, the filter can be viewed as the 'single tunneling layer' filter described several decades ago [88], but in that case employing a solid tunneling layer. Properly designed thin film stacks provide an admittance match, and thus a pass-band, for a desired combination of incidence angle, polarization, and wavelength.

Consider the representative structure shown in Fig. 4.1(b), which depicts part of a nominally symmetric thin film stack coupled at the input and output by identical prisms (see Fig. 4.1(a)). For off-normal incidence, it is convenient to describe the film properties using the concept of tilted admittance [94]. To simplify the analysis, we assume lossless materials with real refractive indices. In that case, the tilted admittance η_j for TE and TM polarized light in medium j can be expressed $n_j\cos\theta_j$ and $n_j/\cos\theta_j$, respectively. Here, n_j is the refractive index, $\theta_j = \sin^{-1}\{(n_{in}/n_j)\sin\theta_{in}\}$ is the propagation angle from Snell's law, and n_{in} and θ_{in} are the refractive index and angle in the incident medium. Furthermore, the phase thickness of a given layer is given by $\delta_j = (2\pi/\lambda)n_j d_j\cos\theta_j$, where λ is the free-space wavelength and d_j is the physical thickness of the layer.

For $\theta_{in} > \sin^{-1}(1/n_{in})$, the electromagnetic fields are evanescent in the air layer, and the effective angle is complex with a purely imaginary cosine: $\cos\theta_A = -i\cdot(n_{in}^2\sin^2\theta_{in}-1)^{1/2}$. It follows that both the admittance and phase thickness are purely imaginary in this case, making the air tunneling layer strictly analogous to a lossless metal layer [88,95]. Thus, we can adapt well-known design procedures for metal-based induced-transmission (IT) filters to the design of the air-gap tunneling filter. While various strategies exist for the design of IT filters, we choose to employ the principle of equivalent layers [96]. Consider the 3 central layers of the filter, comprising the air gap bounded by identical 'phase matching' films. At a given wavelength, and as depicted in Fig. 4.1(b), this 3-layer structure can be replaced by an equivalent layer of effective phase thickness δ_{eff} and effective admittance η_{eff}, given by [95]:

$$\eta_{eff} = \eta_{PH}\left\{\frac{\sin 2\delta_{PH}\cosh\mu_A - \frac{1}{2}Y_M\cos 2\delta_{PH}\sinh\mu_A - \frac{1}{2}Y_P\sinh\mu_A}{\sin 2\delta_{PH}\cosh\mu_A - \frac{1}{2}Y_M\cos 2\delta_{PH}\sinh\mu_A + \frac{1}{2}Y_P\sinh\mu_A}\right\}^{1/2}, \tag{4.1}$$

Here, $Y_M = (\kappa_A/\eta_{PH} - \eta_{PH}/\kappa_A)$ and $Y_P = (\kappa_A/\eta_{PH} + \eta_{PH}/\kappa_A)$. Furthermore, $\eta_A = i\kappa_A$ and $\delta_A = i\mu_A$ are the imaginary admittance and phase thickness of the air layer, respectively, and η_{PH} and δ_{PH} are the real admittance and phase thickness of the phase matching layers, respectively.

As discussed by MacLeod [95], a condition for transmission through this 3 layer system is that η_{eff} must be real. Thus, the role of the phase matching layers is to transform the imaginary admittance of the air layer into a purely real value at some desired wavelength. When this condition is achieved, it is possible to have admittance-matched tunneling (i.e. a resonant pass-band) centered at this wavelength. For a given set of λ, θ_{in}, η_{in}, and η_{PH}, the required thickness for the phase matching layers can be expressed $d_{PH} = \delta_{PH}\lambda/(2\pi n_{PH}\cos\theta_{PH})$, where $\delta_{PH} = (\pi - \xi)/2$ and [16]:

$$\xi = \tan^{-1}\left\{\frac{2\eta_{PH}\eta_A(\cosh 2\mu_A - 1)}{(\eta_A^2 - \eta_{PH}^2)\sinh 2\mu_A + \eta_A(\eta_A^2 + \eta_{PH}^2)(4\pi \cdot d_A \cdot C_A/\lambda)}\right\} \quad . \tag{4.2}$$

In this expression, $C_A = \cos^2\theta_A$ or 1 for TM- and TE-polarized light, respectively, and the tangent should be evaluated in the first or second quadrant.

Once the required thickness d_{ph} is obtained, Eq. (4.1) can be used to evaluate the resulting real effective admittance at the design wavelength. As illustrated by the examples below, the effective admittances solved for TE and TM polarization (i.e. with the other parameters fixed) are typically very different. Specifically, with phase matching layers adjusted according to Eq. (4.2), we typically find $\eta_{eff} << 1$ for TE polarization and $\eta_{eff} >> 1$ for TM polarization. This implies that if a thin film stack is designed to admittance-match light of one polarization state (TE or TM), it will be highly mismatched for the other polarization state. This furthermore suggests that the filters should be highly polarizing, with efficient reflection of the 'off' polarization state, a fact that is confirmed by the results below.

The role of the remaining layers in the thin film stack is to transform η_{in} into a value as close to η_{eff} as possible. The analysis is simplified greatly when the matching stack is a quarter-wave stack (QWS), because a quarter-wave layer of admittance η_j, added to a structure with admittance η_{in}, transforms the front surface admittance to a value η_j^2/η_{in} [33]. Consider for example the QWS constructed from alternating high (η_H) and low (η_L) admittance layers. If we assume a substrate admittance η_{in} and start with a high admittance layer, then the front-surface admittance evolves as (η_H^2/η_{in}), ($\eta_L^2\,\eta_{in}/\eta_H^2$), ($\eta_H^4/\eta_L^2\,\eta_{in}$), ($\eta_L^4\,\eta_{in}/\eta_H^4$), *etc*., as successive

quarter-wave layers are added. This implies that the admittance will alternate between increasingly high and low values with increasing numbers of layers, and for termination by a high or low admittance layer, respectively.

For a given pair of QWS materials and a given prism index, only a discrete and limited set of values for the transformed admittance is possible at a given incident angle and wavelength. However, excellent matching to the central tri-layer can generally be achieved by using an iterative design approach. Specifically, d_A and θ_{in} can be adjusted to change the η_{eff} in one step, and the number of periods in the QWS can be adjusted in a second step. This can be iterated until an acceptable admittance match is achieved.

As a first illustrative example, consider a filter designed to exhibit an admittance-matched pass-band for TE polarized light at 1550 nm wavelength, for an incident angle θ_{in} = 48 degrees, and using an air layer thickness d_A = 3 μm. Furthermore, assume that the ambient media have refractive index n_{in} = 1.44 (representing fused silica substrates and prisms), and that the thin film materials have refractive indices n_H = 3.7 and n_L = 1.46 (representing sputtered a-Si and SiO_2 layers, respectively). Finally, assume that the lower index material is also used for the phase matching layers (i.e. $n_{PH} = n_L$). Using (4.1) and (4.2), we find η_{eff} = 0.0064, for phase matching layers with thickness d_{PH} = 90.9 nm. This effective index can be very well matched using a two-period QWS; i.e. ($\eta_L^4\ \eta_{in} / \eta_H^4$) = 0.0062.

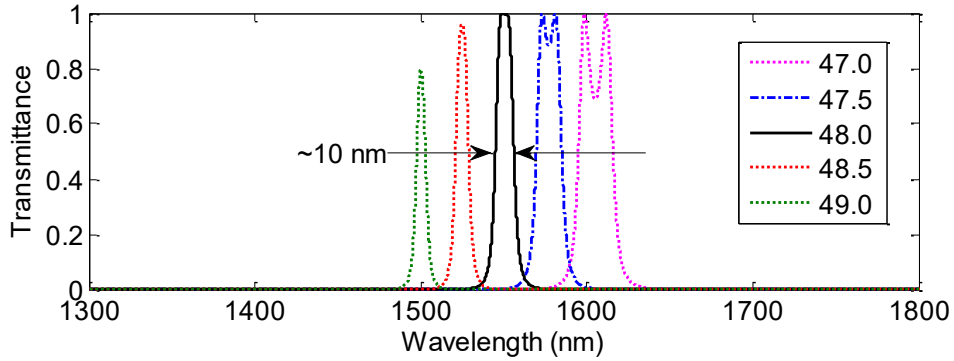

Figure 4.2 - The plot shows predicted transmittance spectra for TE polarized light, and with incidence angle varied (in half-degree increments, as indicated). The layer structure is described in the main text.

The resulting filter structure is {$HLHLL_{PH}AL_{PH}LHLH$}, where H and L denote high- and low-index quarter-wave layers (at the specified angle of incidence), L_{PH} denotes the low-index

phase matching layers, and A denotes the air layer. Transfer matrix simulations of transmittance, with material dispersion taken into account, are shown in Fig. 4.2. As expected, a resonant tunneling pass-band is predicted for TE polarized light incident at ~48 degrees. Furthermore, this pass-band has a flat top, which can be understood as arising from the resonant coupling of the surface states at each side of the air gap [92]. For slightly lower angles, these states are over-coupled, and the single transmission band splits into a pair of pass-bands associated with symmetric and anti-symmetric couplings of the surface states. For slightly larger angles, the surface states are under-coupled and the transmission pass-band has a reduced bandwidth and sub-unity transmittance. The angular shift of the center wavelength is ~ 50 nm/degree. Clearly, angular convolution effects can only be avoided through the use of a highly collimated input beam. On the other hand, angular tuning of the filter pass-band and bandwidth is possible in that case.

The polarizing and rejection properties of the filter are illustrated in Fig. 4.3(a). The simulated range is restricted to wavelengths above 800 nm, since a-Si becomes highly absorbing for shorter wavelengths. For TE polarization, the out-of-band rejection is better than OD5 for wavelengths more than ~100 nm removed from the center wavelength. For TM polarization, the thin film stack does not provide an admittance match, and no resonant pass-band is observed. However, non-negligible transmission of TM light is predicted at the long wavelength end of the spectrum, where the wavelength is on the order of the air gap thickness. This 'leakage' can be suppressed by designing the filter with a larger air gap, although this also impacts the bandwidth and other parameters.

The design procedure can be applied just as easily to achieve a TM polarized pass-band, in which case TE polarized light is strongly rejected. As above, consider using a-Si/SiO_2 matching stacks with SiO_2 phase matching layers. For air gap thickness d_A = 3.1 μm and incident angle θ_{in} = 48 degrees, a TM tunneling band centered at λ = 1590 nm can be achieved for d_{PH} = 174.6 nm, in which case η_{eff} = 234. Furthermore, a 3.5 period QWS (starting and ending with a high index layer) results in a transformed admittance (η_H^8 / η_{in} η_L^6) = 239. The resulting filter structure is {HLHLHLHL$_{PH}$AL$_{PH}$HLHLHLH}, where the symbols have the same meanings as above. The predicted transmittance for this structure is plotted in Fig. 4.3(b). As expected, a flat-top resonant pass-band is observed for θ_{in} = 48 degrees and TM polarized light.

The filter provides extremely good rejection of the TE polarized light across the entire range, but as above the rejection of TM polarized light is reduced at longer wavelengths.

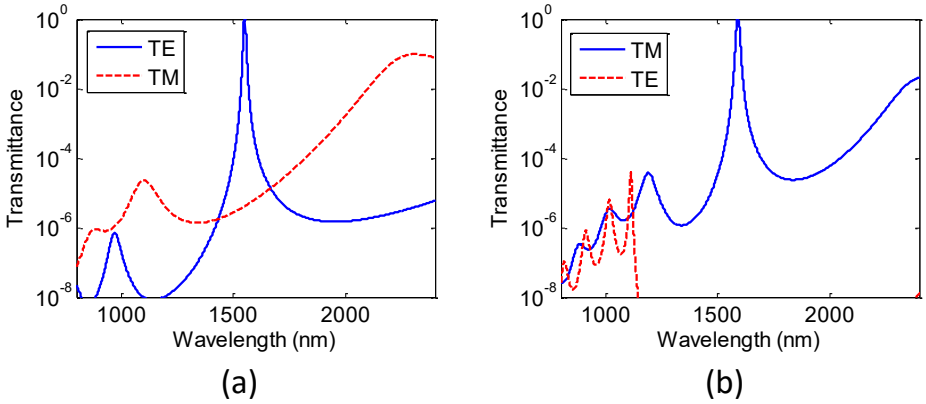

Figure 4.3 - (a) The plot shows the predicted transmittance at 48 degrees incident angle for the sample described in Fig. 4.2, and for both TE and TM polarized light. (b) The plot shows the predicted transmittance at 48 degrees incident angle, for a sample designed to provide a pass-band for TM-polarized light (see main text).

4.4 Fabrication

Prototype devices were fabricated by bonding a pair of nominally matched multilayer samples, with lithographically patterned stand-offs defining the air gap between them. The a-Si/SiO_2 matching stacks were magnetron sputtered [8] onto a piranha-cleaned fused silica substrate, using deposition time to control film thickness. Optical lithography was then used to pattern strips of SU-8 (a photosensitive resin) on parts of the wafer. The substrate was subsequently diced into chips ~10mm x 20mm in size, with SU-8 strips (~3 μm in height and ~50 μm in width) running along the perimeter of half the chips. To create the air gap tunneling filters, an un-patterned chip was clamped on top of a patterned chip. Resonant tunneling efficiency is particularly sensitive to the degree of matching between the phase matching layers on either side of the air gap [92]. Thus, care was taken to bond chips diced from adjacent regions of the substrate. From ellipsometric measurements, we estimated film thickness non-uniformities less than 1% between locations separated by ~20 mm.

Permanent bonding was facilitated by applying pressure to the samples and heating above the SU-8 glass transition temperature [97]. Samples were placed on a hotplate at ~200°C for 1

hour, while pressure was applied using a custom press. Following the SU-8 reflow bonding, a UV curable optical adhesive was placed along the sides of the chips to ensure permanent contact between the pieces and to seal the air-gap tunneling layer from the external environment. The fabricated filters were then sandwiched between a pair of fused silica prisms (Thorlabs PS610), using a refractive index matching gel (Cargille 06350). The assembled structure (see Fig. 4.1(a)) was mounted in a custom holder attached to a precision rotation stage.

4.5 Experimental results

Experimental transmission scans were obtained using a fiber-coupled supercontinuum source (Koheras SuperK SCB-RED) with spectral content spanning the ~600-1700 nm wavelength range. The light from the source was collimated by a fiber collimating lens, and then passed through a broadband Glan-Taylor polarizer. The broadband polarized light was delivered to the filter/prism structure, and transmitted light was collected with another fiber collimating lens and delivered to an optical spectrum analyzer (Yokogawa AQ6370B). In order to estimate the absolute transmittance, experimental power scans were divided by base scans obtained without a sample in the path. Measurements over such a broad spectral range are complicated by the spectral dependence of the optical components [85], so care was taken to optimize the transmission by adjusting the collimator alignment during each measurement. Excellent repeatability between multiple measurements was achieved.

For the results described here, target layer thicknesses were those of the TE-polarized pass-band example shown in Fig. 4.2 (i.e. d_H = 110 nm, d_L = 390 nm, d_{PH} = 91 nm, and d_A = 3 μm). Ellipsometric measurements were performed on single multilayers prior to wafer bonding, from which the as-deposited films were estimated to be slightly thicker than the target values. Furthermore, profilometer scans of fabricated SU-8 strips indicated a height of ~2.7 μm. Experimental transmission spectra for TE polarized light and several different incident angles are shown, for a typical sample, in Figure 4.4. The angles shown are those inside the fused silica input prism, calculated from the external angle in air using Snell's law. The data is in excellent agreement with theoretical fits obtained using d_H = 116 nm, d_L = 395 nm, d_{PH} = 94 nm, and d_A = 2.7 μm. Strong rejection of TM-polarized light across the entire measured range ($T < 10^{-3}$), in keeping with the predictions from Fig. 4.3, was also verified (not shown).

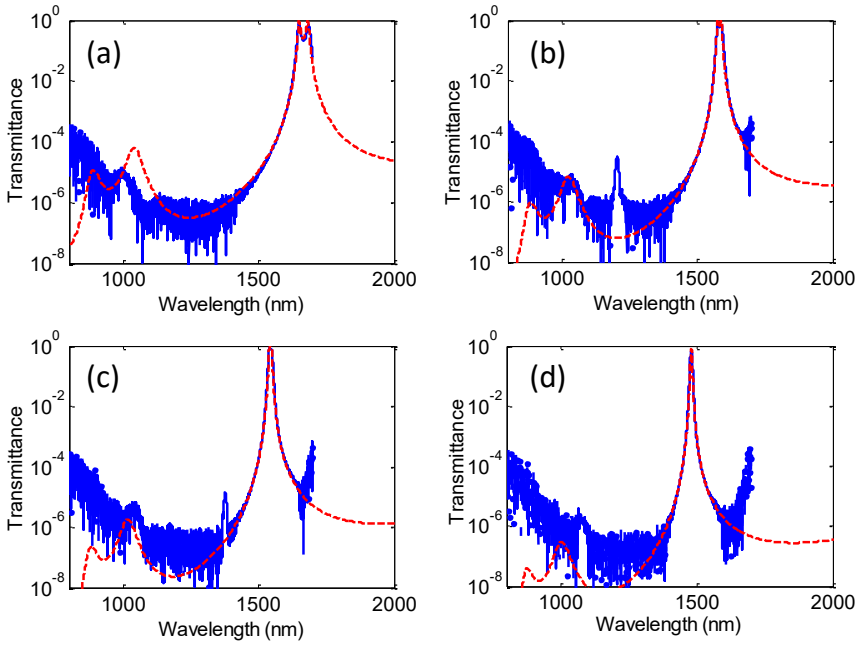

Figure 4.4 - Experimental (blue solid lines) and simulated (red dashed lines) transmittance for TE polarized light is plotted versus wavelength, at various incident angles (inside the prisms): (a) 46.7 degrees, (b) 48.2 degrees, (c) 48.9 degrees, and (d) 50.3 degrees. The layer parameters used for the fitting are described in the main text. In (a)-(c), the peak experimental transmittance is ~0.8, while in (d) it is ~0.65.

The slight discrepancy in layer thicknesses compared to target values, especially the error in d_{PH}, causes the pass-bands to be shifted to slightly longer wavelength for a given incident angle. The lower air gap thickness compared to the target value causes stronger coupling of the surface states, and thus a broader pass-band, for a given angle. Otherwise, the filter behaves as expected from the discussion above. Experimental peak transmission exceeded 85% in many cases. From numerical simulations (not shown), this indicates a mismatch of less than 1% in the phase matching layers on either side of the air gap, as well as low residual scattering and absorption by the thin film layers. Other sources of loss are likely to include thickness non-uniformities and beam divergence. The experimental out-of-band rejection is limited by the dynamic range of the instrumentation, especially near 600 and 1700 nm wavelength, where the source has limited power spectral density. Nevertheless, rejection on the order of OD6 or better is suggested by the data in Fig. 4.4. Secondary transmission peaks, such as at ~1200 nm in Fig. 4.4(b), were identified as experimental artifacts, likely due to scattering at the optics interfaces.

4.6 Conclusion

In summary, we have described a design procedure, fabrication process, and experimental results for a resonant tunneling filter and polarizer with an embedded air gap layer. Filters with flat-top pass-bands ~10 nm wide and out-of-band rejection on the order of OD6 were demonstrated. Narrower bandwidth and higher rejection are possible, in principle, with the use of higher period count matching stacks, although the layer thickness tolerances will become more demanding in that case. A key attribute of these filters is their strong rejection (i.e. reflection) of one orthogonal polarization state over a broad range of wavelengths. This is much preferable to the polarization-dependent transmission pass-bands exhibited by conventional tunneling filters [88], and could allow novel optical systems that separate both wavelength and polarization. These filters could be particularly well suited to applications involving highly collimated, broadband supercontinuum sources.

Chapter Five: Development of visible-range buckled waveguides

5.1 Introduction

This chapter details the development of a set of processes for the fabrication of hollow waveguides utilizing a guided buckling technique. An analogous process has previously been used to create hollow waveguides operating in the near-IR range, employing chalcogenide/polymer or Si/SiO_2 materials [27,29]. As detailed in Chapter 3, hollow waveguides operating in the visible range were initially fabricated using a wafer bonding technique [28,60]. The wafer bonding approach, while based on standard microfabrication steps, has many disadvantages. Specifically, the platform has limited versatility and the hybrid integration process is reliant on the skill of the assembler. To address these shortcomings, the successful adaptation of the guided-buckling technique to devices operating in the visible range was a major goal of the thesis work. Structures fabricated in this fashion have been shown to form low-loss waveguides [27], are the basis of a micro-spectrometry platform [7], provide a sensing platform for wavelength interrogation [98], and have produced high finesses optical cavities [8]. Adapting the buckling process into the visible region might enable applications to fluorescence sensing in LOC systems, as well as other hollow-core integrated optics applications such as cavity quantum electrodynamics (cQED) studies with alkali atoms [4–6].

The essential details of the Buckling-based fabrication process are shown in Fig. 5.1. First, a distributed Bragg reflector is deposited on a substrate (typically silicon). A low adhesion layer (LAL) is then patterned on top of the bottom mirror. A matching mirror is then deposited under compressive stress, embedding the LAL between the two reflectors. Lastly, an experimentally optimized release step is used to further reduce the adhesion between the LAL and mirror surfaces, in order to induce buckling of the top mirror. Buckle delaminations form over the patterned LAL regions, and can form a variety of air-core structures including uniform waveguides, tapers, s-bends and domes. To facilitate the fabrication of waveguides operating in the visible range, it was necessary to adapt the process to the use of new material combinations providing low loss at visible wavelengths. This required the optimization of each fabrication

step, to accommodate the new material system. The following sections provide a detailed overview of the development of these newly optimized processes.

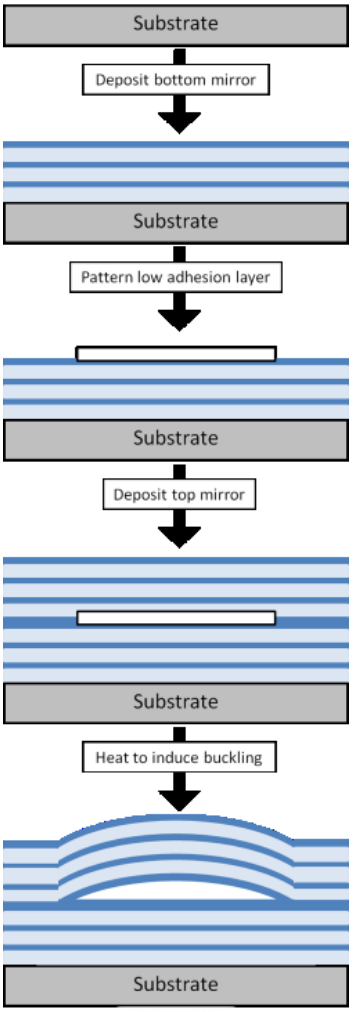

Figure 5.1 Process flow for the fabrication of hollow waveguides formed by guided buckling. A low adhesion layer is patterned between matching distributed Bragg reflectors, with the upper mirror deposited under compressive stress. An optimized release step is used to induce buckling by further reducing the adhesion between the mirrors and the LAL.

5.2 Sputtering

The process of guided buckling is reliant on the top multilayer being deposited under compressive stress. Furthermore, to form low-loss waveguides, the stress must be tuned such that straight-sided 'Euler columns' (see Chapter 2) are the dominant buckling modality, for a given

range of buckle widths of interest. Therefore, in order to fabricate low-loss buckled waveguides, the deposition process must enable a high degree of control over thin film stress, while also being capable of depositing low-loss optical thin films. Sputtering is a natural choice, since film stress can be optimized by adjusting the deposition parameters [99]. Furthermore, modern advancements in sputtering systems have enabled the high-rate deposition of low-loss optical coatings [100].

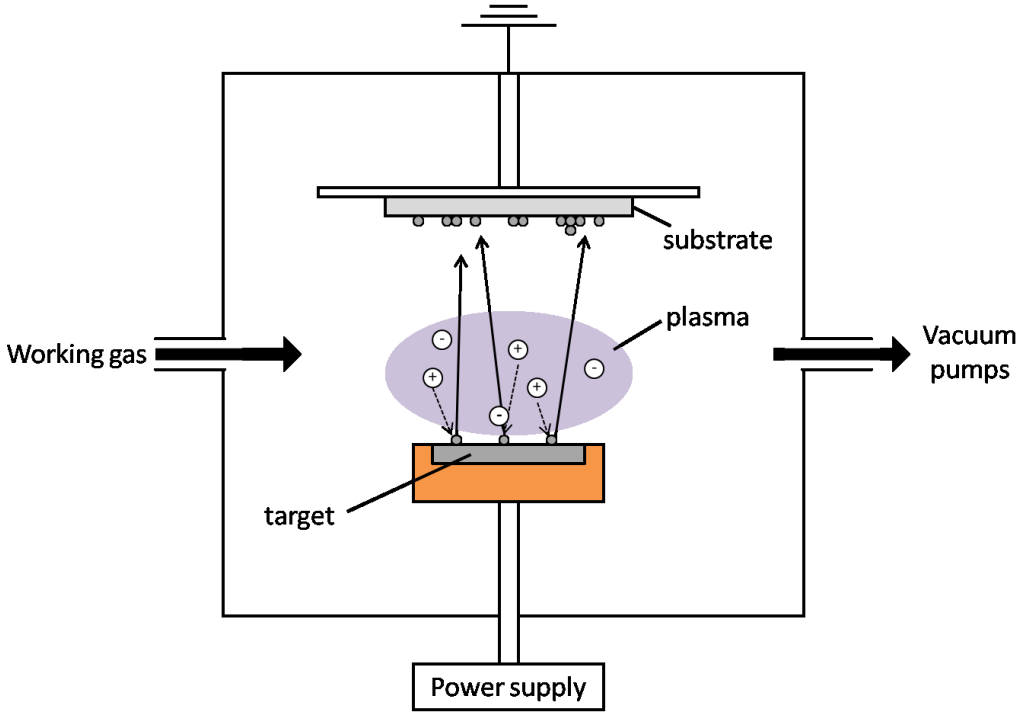

Figure 5.2 Schematic of a typical sputtering system.

Figure 5.2 depicts a schematic of a typical sputtering system. A conducting source material, called the target, and the substrate are placed in a vacuum chamber, which is pumped to low pressure to remove contaminants. A heavy inert gas, typically Ar, is introduced into the chamber and voltage is applied with the target material acting as the cathode and the substrate as the anode. A glow discharge forms in the region between the electrodes, and as the Ar atoms ionize they are driven toward the surface of the conducting target material. This bombardment of ions causes a cascade effect, where momentum transfer causes atoms of the target material to become dislodged and ejected, while secondary electrons are produced and help to fuel the glow

discharge. The ejected atoms travel with high energy through the glow discharge and strike the substrate, forming a film.

The simple sputtering process described above is known as diode sputtering, and suffers from several limitations. Ejected target atoms must travel through the plasma, causing large amounts of scattering. Atoms that reach the substrate surface have their kinetic energy significantly reduced. This ultimately leads to a low deposition rate and low film density. In diode sputtering, the plasma is also subject to low ionization efficiencies, and electrons within the plasma can produce unwanted heating of the substrate [101]. To address these shortcomings, magnetron sputtering was developed, whereby magnetic fields are used to trap secondary electron movement close to the target surface. The strong electron confinement substantially increases the ionization efficiency of the plasma and thus radical formation within the plasma, which in turn increases ion bombardment of the target surface, leading to higher sputter and deposition rates. Target consumption is localized to the areas directly below the densest regions of the plasma; this produces an erosion pattern commonly termed the "racetrack" region. In addition to higher deposition rates, the heavily efficient and localized plasma allows operation at pressures which are an order of magnitude lower than those of diode sputtering, significantly increasing the mean free path of the ejected target atoms [101]. The highly energetic nature of this deposition technique produces dense, compressively stressed films [51,102]. The impact of this technology has been profound, and has been regarded by some as the most important technology for the deposition of thin films [103].

5.2.1 Bipolar pulsed DC magnetron sputtering

To produce many of the oxide films used as optical coatings (TiO_2, Ta_2O_5, SiO_2, AlO_3, WO_3, ZrO_2, etc.), a process called reactive sputtering is required. A conductive metal target is sputtered in the presence of a reactive gas to form a desired compound. In the case of optical coatings, O_2 is often used in conjunction with Ar gas. The addition of oxygen into the system, however, introduces a host of problems. The first issue is *target poisoning*, whereby the compound forms on the surface of the target, eventually covering it. Besides a dramatic reduction in deposition rate, sputtering from a poisoned target can produce sub-optimal films. The insulating compound forming on the racetrack area of magnetron systems is typically removed by the plasma. However, dielectric buildup occurs on the centre and edges of the target. The dielectric layer

creates a capacitive effect, leading to charge buildup on the target surface. This can give rise to dielectric breakdown in the form of an *arc*. Arcing is extremely disadvantageous: large chunks of the target material can bombard the substrate producing poor quality films. Moreover, fragile targets, such as Si, can fracture due to arcing [104]. Arcing is one of the most challenging aspects to reactive sputtering and reducing or eliminating its occurrence is crucial to producing high quality optical coatings [105].

Dielectric build-up occurs not only on the target surface but also on every exposed region of the chamber. For many sputtering systems, the anode can be the chamber walls, substrate holder, or target shield, and the gradual buildup of dielectric material on these surfaces reduces their effectiveness. This can lead to the *disappearing anode* effect, which can extinguish the glow-discharge and halt the deposition.

Historically, radio-frequency (RF) sputtering has been used to address these issues. RF diodes electrically reverse the anode and cathode, effectively eliminating charge build-up on dielectric surfaces [104]. Although RF sputtering can produce high quality films, its adoption has been limited due to slow deposition rates, the need for expensive impedance matching networks, and poor scalability [101,106]. More recently, pulsed DC magnetron sputtering has been developed and has become the *de facto* technique for deposition of high quality dielectric films [100,101,103,107,108].

A schematic for the operation of pulsed DC power on a target is shown in Fig. 5.3(a). The voltage applied to the target alternates at kHz frequencies between normal operating values (negative) during the pulse-on time, τ_{on}, to some positive value during the pulse-off time, τ_{off}. During the on-time, Ar^+ ions build up on the dielectric film forming on the target surface. In the off-time, the polarity is reversed from, for example, -400V to +100V, driving electrons to the surface and charging it to a value of +100V. When the cycle switches back to the on-time, the effective voltage across the dielectric build-up region becomes -500V compared to -400V for regions without any buildup. This allows the *preferential* sputtering of the dielectric material, eliminating target poisoning and eventual arcing [107]. Electrons have significantly higher mobility compared to the Ar^+ ions, so the pulse-off voltage only needs to be ~10-20% of the pulse-on value [101]. High electron mobility also allows the duty cycle, defined as $\tau_{on} / (\tau_{on} + \tau_{off})$, to be quite high enabling deposition rates comparable to that of standard DC sputtering

[101,107]. The use of pulsed DC power compared to standard DC power is illustrated in Fig. 5.3 (b-c).

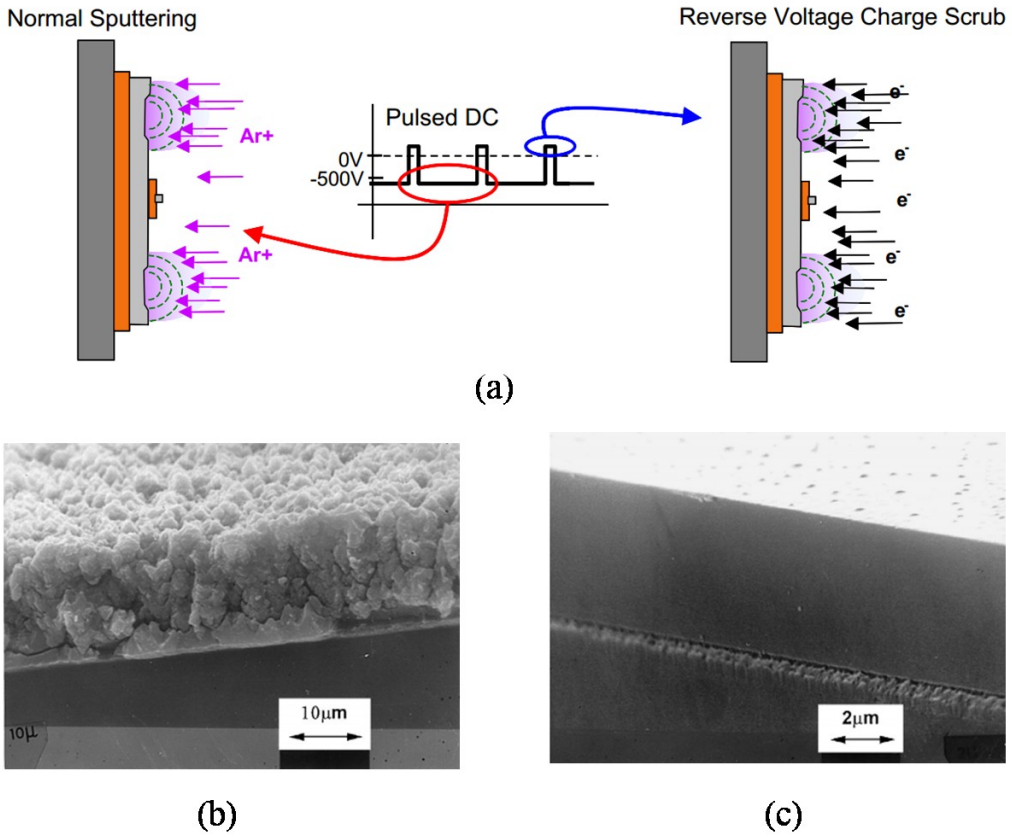

Figure 5.3 - (a) Schematic of the target surface during bipolar pulsed DC magnetron sputtering (adapted from [109]**). During the pulse-on time positive charge build-up occurs on the target surface. During the pulse-off time electrons are attracted to the target surface to counteract the positive charge buildup. SEM micrographs of Al_2O_3 films deposited by (b) standard DC reactive sputtering and (c) pulsed DC reactive sputtering (adapted from** [110]**).**

The physics behind pulsed DC sputtering is complex, with power, frequency, duty cycle, gas pressure, temperature, and chamber geometry all playing a role in the resultant film properties. Due to these complex relationships, in-house recipes must be developed for a specific deposition system and for each material of interest. Nonetheless, dielectric films deposited using pulsed DC power have been shown to be dense, defect-free, stoichiometric, and repeatable [100,101].

Depicted in Fig. 5.4 (a) is the sputtering system employed for the fabrication of the optical thin films in the present work. It is a 3-gun commercial magnetron sputtering system (Kurt J. Lesker) equipped with pulsed DC power supplies for reactive sputtering (AE Pinnacle Plus), and a mass flow controller (MKS 647C) to supply multiple reactive gases. The system is capable of substrate heating up to 150°C and can achieve base pressures < $2x10^{-6}$ Torr for a pump time of ~1 hour via a cryo-pump (Cryo-Torr®). Working gas pressure during depositions is monitored by a Baratron® gauge (MKS). Targets are loaded in 3" water-cooled copper guns located at the bottom of the chamber and fastened using a screwed-on retaining ring. Substrates are loaded on a rotating substrate holder ~20cm above the guns. A cross-sectional view of the sputter gun is pictured in Fig. 5.4 (b). The system is housed in the Nanofab at the University of Alberta and receives moderate use from a variety of users.

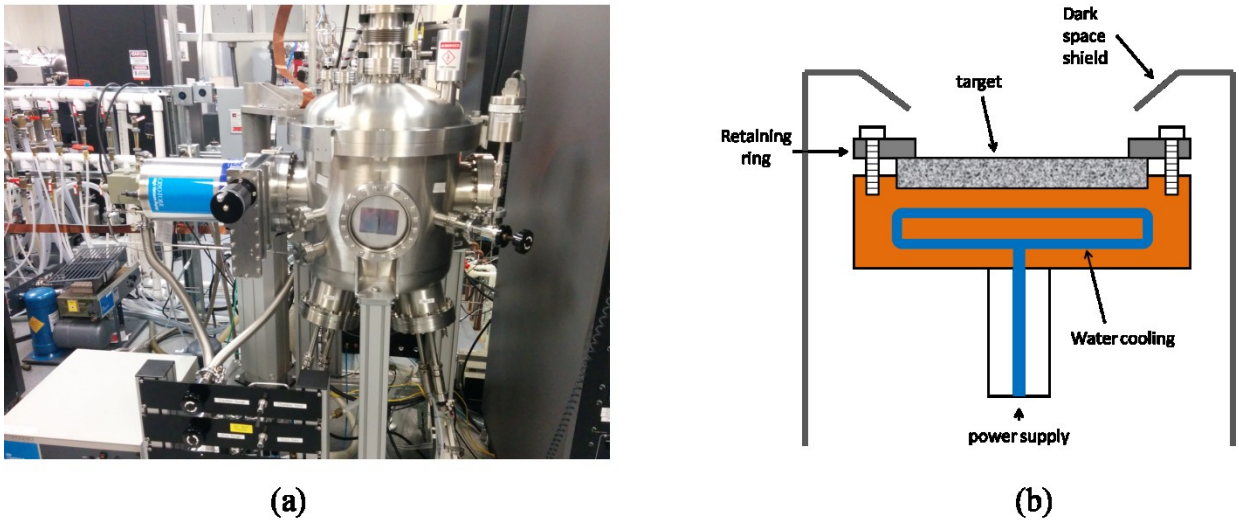

Figure 5.4 - (a) The sputtering system used for the deposition of thin films. (b) A cross-sectional schematic view of a typical sputter gun. Targets are placed in a recessed water-cooled copper holder and clamped down using a retaining ring that is affixed with screws.

5.2.2 Control of stress in sputtered films

As discussed above, sputtering was chosen because it provides the ability to modify deposition parameters to achieve the desired level of compressive stress, as needed for the buckling process. While, in general, most films deposited by sputtering are inherently compressive [51], there exists a transition region whereby the stress of the film moves from compressive to tensile or

vice versa [99]. The transition is abrupt and the precise conditions depend on a variety of factors and vary from machine to machine. There are, however, principles that can be used to guide the experimental process towards the desired stress result.

It has been found that films that are formed from more energetic atoms are typically more dense and compressively stressed [99]. Therefore, by modifying conditions which increase or decrease the energy of sputtered atoms, the stress can be modified to the desired level. Thornton and Hoffman, for example, found that a relatively low deposition rate at low pressures increased the magnitude of compressive stress in films [99]. Morton *et al.* found that most optical films became more compressively stressed when the pressure or power supplied is decreased [100]. These results can be explained by a general increase in mean-free-path of the sputtered atoms, reducing the number of collisions they undergo, which in turn minimizes energy loss. Other parameters, such as sputtering frequency and duty cycle, also play a role in determining film stress. To produce the desired buckle morphology, deposition parameters must be selected to produce stress that lies within the range for Euler-column formation (see Fig. 2.8). Films must also be deposited to minimize optical losses. Obtaining a balance between stress and optical losses proved to be a critical part of the development work in this thesis.

5.2.3 Sputtering of monolayer samples

The development of the low-loss, high stress DBRs began with the deposition of monolayer samples to determine the optical and mechanical properties of prospective high- and low-index materials. Each material underwent an in-depth optimization process to determine ideal process parameters. Optical properties were determined by fitting raw data acquired using a VASE measurement system (J.A. Woollam) as discussed in Chapter 3. Stress values were determined using a Flexus measurement system. Following this, multilayer samples were developed for buckling.

5.2.3.1 Sputtering of SiO_2

Selecting SiO_2 as the low-index material for the DBRs was a natural choice as it is one of the few low-index materials capable of being deposited by sputtering [106]. Regrettably, sputtering SiO_2 proved to be one of the more challenging aspects of the project due to issues with arcing (see above).

Films were reactively deposited onto piranha cleaned silicon substrates using a 99.999% pure *n*-type Si target (Lesker). The system was pumped down to 1.0×10^{-6} Torr prior to all depositions. The bipolar pulsed DC power supply and an O_2/Ar atmosphere were used for all SiO_2 depositions. In an effort to improve stoichiometry, films were deposited at 150°C (the maximum temperature for the system) [111]. Efforts focused on improving process repeatability and optimizing film characteristics. Two recipes were ultimately developed: the first favours high stress at the cost of higher optical loss, as is required for the upper mirror, while the second provides reduced stress but improved optical characteristics, as is more optimal for the lower mirror. Table 4.1 provides the complete recipe details. Parameters for high stress stemmed from high power depositions (200W) at low oxygen flow rate (3.2sccm) and at moderate pressure (4mTorr). Decreasing the power or pressure, or increasing the oxygen flow rate, which consequently reduced the deposition rate, tended to reduce the compressive stress of the films. Bhatt and Chandra postulate that a reduction in deposition rate allows the adatoms to have sufficient time to migrate to low energy positions before being trapped by incoming atoms [112], resulting in lower stress. Conversely, for improved optical characteristics, higher oxygen flow rate (4sccm) at lower power (150W) proved to be the optimal combination of deposition parameters. The optical constants from films produced by both recipes over the wavelength range of interest are presented in Fig. 5.5.

Table 5.1 Deposition parameters for sputtered SiO_2 films

Film	Power (W)	Freq. (kHz)	Duty Cycle (%)	Target Bias (V)	$O_2/(O_2+$ Ar) flow ratio	Pressure (mTorr)	Dep. rate (nm/s)	n_{550}	k_{550}	Film Stress (MPa)
Low loss	150	150	88	464	0.07	4.0	0.18	1.46	8×10^{-6}	-120
High stress	200	150	88	487	0.06	4.0	0.29	1.49	0.003	-200

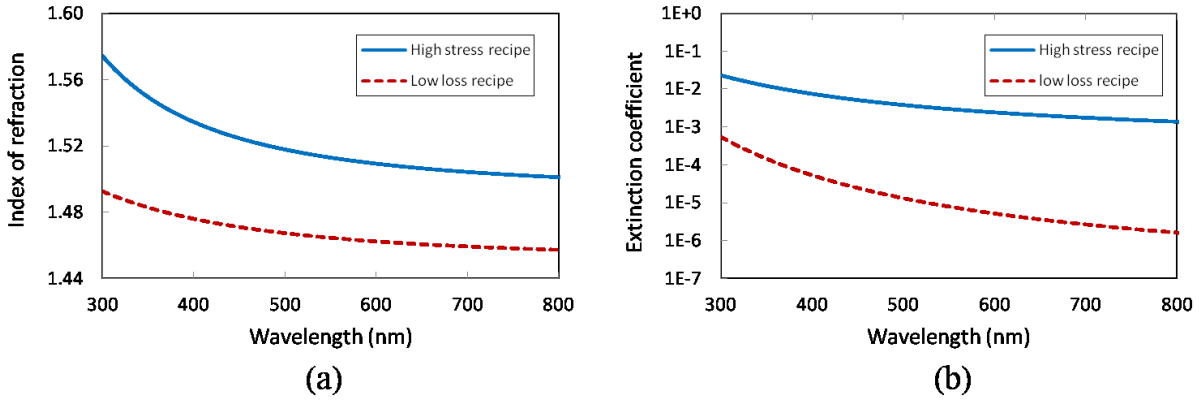

Figure 5.5 - (a) Index of refraction and (b) extinction coefficient of reactively sputtered SiO_2 films. Results were obtained using a VASE measurement system and determined using Cauchy fits.

As alluded to previously, arcing proved to be a major obstacle in the refinement of the process and film recipes. Silicon targets are particularly susceptible to the effects of arcing due to their relatively fragile nature. The Pinnacle Plus power supplied used has built in arc suppression that extinguishes hard arcs within 200μs. However, during this time target pitting can occur. The pits can turn into hairline fractures and eventually the target can break. In many cases, it is impossible to tell whether a target has completely fractured during a deposition. Several targets were damaged during the early stages of the work, but the problem was eventually addressed through a series of process refinements summarized briefly as follows:

- *Installation of aluminum ring*: The primary location of arcing was found to be along the sides of the target, which are exposed to the chamber atmosphere (see Fig. 5.4(b)). The arcs would cause chipping along the target sidewalls and within a few depositions lead to complete target fracture. To alleviate this, an aluminum ring was placed around the exposed area of the target, isolating it from the chamber atmosphere.
- *Uniform tightening of the retaining ring*: The uneven clamping of the retaining ring over the target was also a source of target fracture (see Fig. 5.4(b)). As the target is bombarded by ions during sputtering it begins to heat up and expand. If the clamping is uneven it can cause unwanted stress in the vicinity of a screw which can also lead to target fracture. Careful control of the tightness of the screws can ensure proper room for the target to expand during depositions.

- *Using bonded targets:* In the latter stages of the work, targets were purchased with an elastomer-bonded copper back plate to extend the usable life of the target. The backing plate acts to improve target cooling by transferring heat more effectively to the water cooled gun while also improving the structural rigidity of the target, allowing use even after a crack or fracture develops. Target fracture has yet to occur on the bonded targets, and replacement has only been necessary after targets have been fully consumed.
- *Long power ramp*: To further reduce the chance of thermal shock on the target, a long power ramp (600s) was added to the process. Equally important was the ramp down (also 600s) from the deposition power.
- *Using a clean or pre-conditioned chamber*: In a multiuser reactive sputtering system, many materials of varying properties (e.g. Al_2O_3, AlN, ITO, etc.) get deposited. These materials can significantly alter the chamber conditions during deposition leading to irregular results. In some cases, dielectric buildup on the chamber surfaces can occur, which increases the likelihood of an arc or disappearing anode. Cleaning all removable chamber pieces (e.g. target separator, dark space shield, retaining rings) as well as pre-conditioning the chamber (depositing titanium to cover the chamber surfaces prior to deposition) helps to ensure reproducible results.

5.2.3.2 Sputtering of TiO_2

For much the same reasons discussed in Chapter 3 (high index, hardness, chemical and mechanical stability), TiO_2 was an ideal candidate as the high index material. Furthermore, it has been shown that high quality TiO_2 films for optical applications can be deposited using pulsed DC sputtering techniques [70,113,114]. Sputtered films have been shown to have higher index, lower loss, and provide improved adhesion and wear resistance compared to films deposited using other methods.

A 99.995% pure titanium target (Lesker) was used to reactively sputter thin films onto piranha-cleaned glass or silicon substrates. Similar to the SiO_2 case, an in-house recipe was developed to meet the requirements of low loss and adequate stress. The use of a relatively low frequency setting for the power supply has been shown to produce higher indices, for example as high as $n = 2.5$ for TiO_2 films [113]. This an advantageous characteristic for maximizing the stop band of a Bragg mirror. In keeping with this, optimal pulsing parameters were found to

correspond to a supply frequency of 60 kHz with an 80% duty cycle (see Table 5.2). Other strategies found to maximize the film index include elevated deposition temperature [70], and reduced deposition pressure [115]. The elevated index is a result of a more densely packed film, which also increases the compressive stress of the film [74,116]. The O_2 flow rate can have complicated consequences on the film index and stress, which are related to the chemistry in the plasma and on the target surface. Initial attempts to deposit TiO_2 at low pressure consistently resulted in the plasma being extinguished. The source of the instability was the target and chamber surfaces, which were found to be completely oxidized after removal from the chamber (see Fig. 5.6 (a)). Attempts to reduce the oxygen flow up to 25% showed no improvement to stability. At even lower oxygen flow rates, the resultant films were found to be lossy and to have high tensile stress. It was speculated that the proximity of the particular gun used to the O_2 gas inlet was part of the reason for the instabilities. Tests proceeded on a sputter gun positioned farther from the inlet. The relative transparency of TiO_2 films deposited on this gun at different oxygen flow rates can be seen in the image shown in Fig. 5.6 (b). The changes mentioned above yielded a relatively stable process that produced low loss films, the parameters of which are provided in Table 5.2.

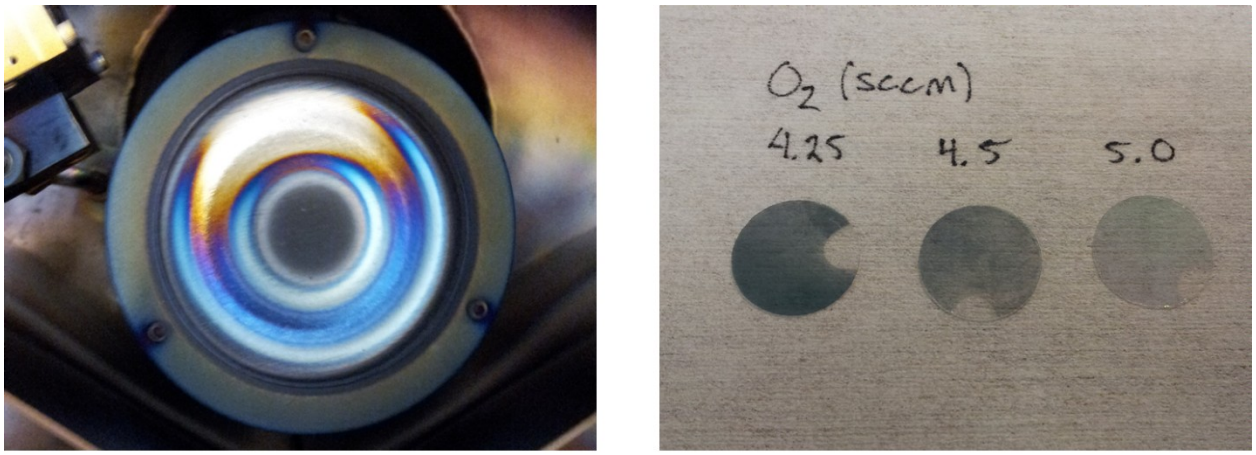

Figure 5.6 - (a) A heavily oxidized Ti target, shown following a deposition. (b) TiO_2 films sputtered at varying oxygen flow rates (as labeled) are shown. The relative transparency of the films is a visual indicator of their loss.

Table 5.2 - Deposition parameters for sputtered TiO_2 films

Film	Power (W)	Freq. (kHz)	Duty Cycle (%)	Target Bias (V)	$O_2/(O_2+$ Ar) flow ratio	Pressure (mTorr)	Dep. rate (nm/s)	n_{550}	k_{550}	Film Stress (MPa)
TiO_2	300	60	80	430	0.11	2.0	0.11	2.46	$7x10^{-7}$	-130

Optical properties of the resultant films are shown if Fig. 5.7. Films exhibited high index (n_{550} = 2.46) and low loss (k_{550} = $7x10^{-7}$) in the visible region. Film stress was found to become more compressive with decreasing pressure, with optimal films having typical stress values of -130 MPa. Interestingly, multiple samples were found to be highly compressive (> -300MPa) for identical deposition parameters. Optical characteristics were found to be invariant across multiple tests, however. The reasons for the variation in the stress is the subject of ongoing work.

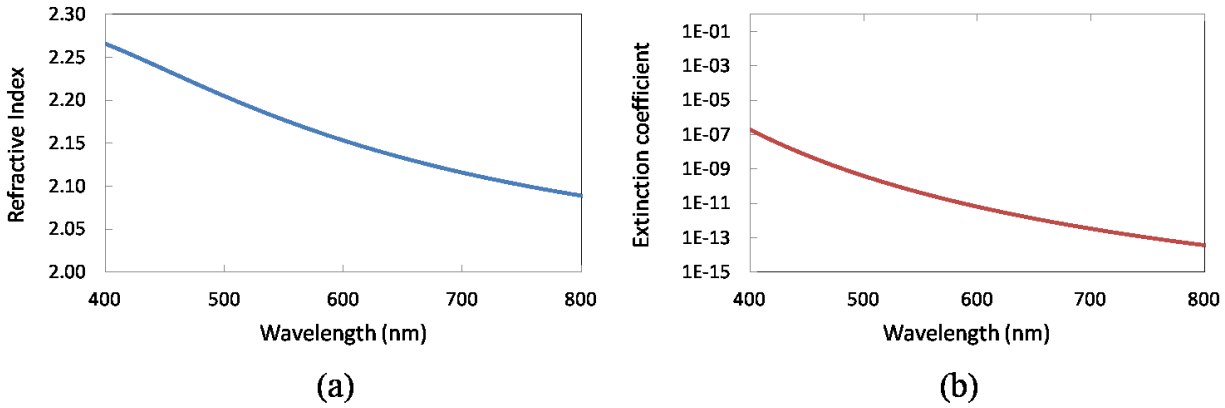

Figure 5.7 - (a) Index of refraction and (b) extinction coefficient of reactively sputtered TiO_2 films. Results were obtained using a VASE measurement system and determined using Cauchy fits.

5.2.3.3 Sputtering of Ta_2O_5

Tantala was also investigated as a high-index material. Ta_2O_5 is a commonly used high-index material [75,102], and is often combined with SiO_2 to form extremely high reflectance "supermirrors" reported in the literature [34,89]. Similar to TiO_2, Ta_2O_5 possesses many desirable characteristics, such as strong adhesion to glass [117], low absorption, high index (albeit, slightly less than TiO_2), and good controllability for thin film deposition [75].

Single-film depositions were performed using a 99.95% pure Ta target (Lesker) onto silicon and glass substrates, and were used to assess the optical and mechanical characteristics. Depositions were performed at 150°C to be compatible with the deposition of SiO_2 layers. An elevated deposition temperature can be detrimental to the stoichiometry of Ta_2O_5 films. However, for thin films (< 1μm) the effect is predicted to be negligible [118]. Parameters such as frequency, reactive gas flow rate, power, and deposition pressure were varied to determine optimal parameters. A combination of high power deposition (300W), low frequency (20kHz), and low pressure (2mTorr) produced the highest index (n_{550} = 2.21) and extremely low loss (k_{550} < $1x10^{-6}$) films, consistent with results reported in the literature [100]. Stress was moderate (-170MPa) and the deposition rate was quite high (~0.5nm/s). Often, high deposition rate is considered to be an advantageous characteristic. However, for optical thin films, where precise control over layer thickness is critical, a lower more controlled deposition rate is preferred. Taking this into consideration, subsequent films were deposited at lower power to reduce the deposition rate. The optimized deposition parameters at lower power are presented in Table 5.3.

The resultant film, as expected, had a slightly lower index (n_{550} = 2.18) but a more controllable deposition rate. The film also had slightly higher stress, a beneficial consequence, consistent with conclusions reached elsewhere [100]. The optical constants for the optimized film parameters are depicted in Fig. 5.8.

Table 5.3 - Deposition parameters for sputtered Ta_2O_5 films

Film	Power (W)	Freq. (kHz)	Duty Cycle (%)	Target Bias (V)	$O_2/(O_2+$ Ar) flow ratio	Pressure (mTorr)	Dep. rate (nm/s)	n_{550}	k_{550}	Film Stress (MPa)
Ta_2O_5	200	20	90	540	0.33	4.0	0.18	2.18	< $1x10^{-5}$	-230

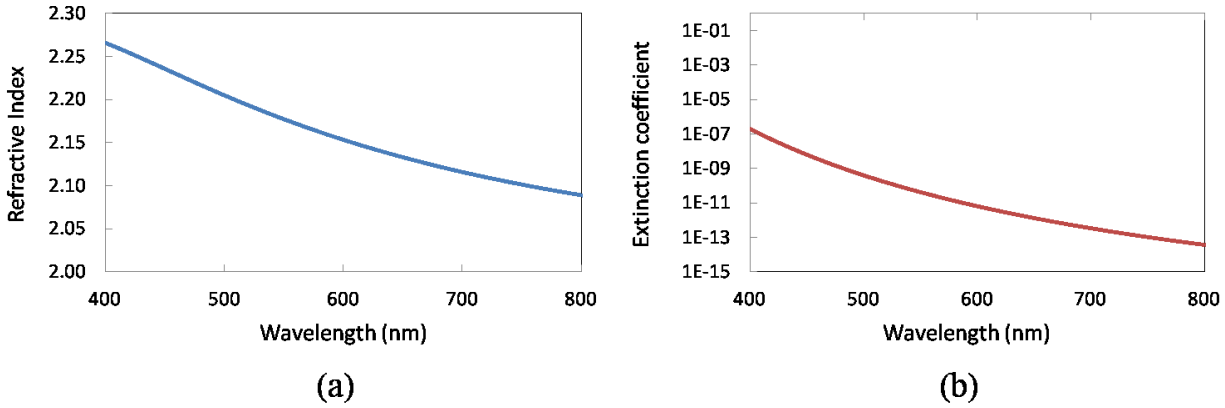

Figure 5.8 - (a) Index of refraction and (b) extinction coefficient of reactively sputtered Ta_2O_5 films. Results were obtained using a VASE measurement system and determined using Cauchy fits.

5.3 Development of the low adhesion layer

Along with high quality optical films, the development of a suitable low adhesion layer was a crucial component needed to realize buckled waveguides. Several methods exist to reduce the adhesion of thin films, but most fall within one of two categories: surface treatments [119,120] or a thin film coating such as diamond-like carbon [121] or metal layers such as aluminum or silver [30,54], to alter the surface properties. If a thin film coating is used, the layer must possess certain characteristics in order to be a suitable choice. Namely, the layer must be easily patterned using lithography techniques, be optically transparent in the wavelength range of interest, be capable of surviving the deposition of the upper mirror (high vacuum, 150°C), provide good uniformity with controllable deposition rates, and provide low enough adhesion to the high index layer to facilitate buckling.

One material that is of particular interest is polytetrafluoroethylene (PTFE), better known by its trade name Teflon®. Teflon is commonly used for non-stick coatings in consumer goods and possesses excellent thermal, chemical and electrical properties, some of which are listed in Table 5.4. Fluorocarbon (FC) thin films used in microfabrication can be seen as PTFE-like and share many of characteristics of bulk PTFE, including low dielectric constant, high hydrophobicity, low friction coefficient, high chemical inertness, biocompatablilty, high corrosion resistance, good temperature stability and good transparency in the visible range

[79,122–126]. Furthermore, FC films have been shown to have low surface energy due to long carbon chains with CF_2 groups [127]. These characteristics have made FC films an attractive option as an anti-stiction material for MEMS. As a result, there are many reports that detail the optimization of the anti-adhesive properties of this material [128–131]. Fluorocarbon thin films can be deposited by RF sputtering of a PTFE target [123], electron beam evaporation of bulk PTFE [128], spin coating a solution of FC722® and FC40® [126], and plasma polymerization of various precursor gases [122,128]. Of the various deposition methods, plasma polymerization is intriguing and has been shown to outperform bulk PTFE under certain conditions [132]. For these reasons plasma polymerized FC films were investigated in detail in this work, as the LAL for the buckling self-assembly process (see Section 5.1).

Table 5.4 - Selected properties of bulk PTFE (Teflon). Adapted from [128]**.**

Contact angle with water	Maximum Temperature	Melting Point	Refractive Index	Optical Transmission
108°	225°C	327°C	1.4	>95%

The plasma polymerized FC films used in this work were based on the material deposited during the passivation cycle of the Bosch process. The Bosch process is used to achieve deep vertical etching on substrates by alternating plasmas of SF_6 and C_xF_y feed gases. The layer produced during the C_xF_y passivation cycle protects the sidewalls from etching in the subsequent SF_6 etching cycle. FC films produced using this method have been shown to have low pin-hole density, low surface energy, and sufficient mechanical robustness to survive subsequent patterning and sputter deposition [8,129,131,133]. In order to verify material compatibility and adequate film properties, an optimization study of the plasma polymerized FC films was performed.

5.3.1 LAL experimental detail

Polymer films were deposited using a commercial inductive coupled plasma reactive ion etch system (ICP-RIE, Alcatal AMS110) housed in the class 100 cleanroom of the Nanofab at the University of Alberta. The system provides user control over a variety of processing parameters including deposition pressure, gas flow rate, RF coil power, as well as chuck bias, position and

temperature. The system has an automatic load lock which keeps the chamber under vacuum and reduces contamination. Initially, piranha-cleaned Si wafers were used as substrates, allowing a direct comparison of film properties to those of similar films reported in the literature. Samples were typically cleaved into quarter-wafers and mounted on a 6" wafer using double sided vacuum tape. Prior to deposition on the wafers, the system undergoes two conditioning steps: a 10 minute O_2 plasma clean is performed followed by a 30s FC film deposition to coat the chamber side walls. Samples were then subjected to the passivation step of the Bosch cycle with C_4F_8 as the precursor gas. Parameters that were varied to determine optimal film properties include deposition pressure, coil power, and gas flow rate.

Following deposition, the samples were characterized using a variety of equipment. Film thickness and optical properties were determined using a VASE (J.A. Woollam). The samples were scanned at 65° between 400 and 800nm at 2nm increments. Collected data was fit using Cauchy fitting parameters with an Urbach tail, as discussed previously in Chapter 3. Thickness measurements were corroborated with a contact profilometer (Alphastep IQ, KLA Tencor). Decomposition tests were also performed in air using a hotplate and, to simulate deposition conditions, under vacuum using the sputtering chamber employed for thin film deposition.

To assess hydrophobicity, contact angle measurements were performed with deionized (DI) water using a commercial system and accompanying software (First 10 Angstroms). Values reported represent an average of a minimum of five measurements per sample using droplets of the same size. Direct measurement of the adhesion of a film can be difficult and time consuming. However, indirect measurements, including liquid contact angle measurements, have been shown to be directly related to surface energy and correlate to the adhesive properties of FC films [131,133].

5.3.2 Low Adhesion Layer Experimental Results

Initially, deposition parameters were chosen to match the default passivation recipe for the Bosch cycle used in the system. This recipe, denoted as "Default", is characterized by high power (1000W), high pressure (53mTorr), and high C_4F_8 flow rate (300sccm). The recipe had a deposition rate of 2.8nm/s and films were found to be hydrophobic (contact angle 101.07°) and of high index (n_{550} = 1.50). The contact angle and refractive index were significantly different

than that of bulk PTFE (see Table 5.4) and of anti-stiction FC films reported in the literature, where index values of $n = 1.37$ and contact angles >108° are typical [122,124,131].

The properties of FC films have been shown to be dependent on the F:C ratio present in the film [134]. Higher Fluorine concentrations are indicative of higher CF_2 species which, in general, correlate to higher hydrophobicity and lower surface energy [129,130]. Furthermore, *Labelle* found that low F:C ratio films tend to have higher refractive indices than bulk PTFE [135] which suggests, coupled with the low contact angle, that the Default recipe likely possessed a low F:C ratio. Coil power and deposition pressure were found to have the most direct influence on the F:C ratio of the resultant film, with a combination of low pressure and high power favouring high F:C ratio films [135]. Although other variables such as substrate temperature and flow rate have been investigated, they appear to have less pronounced influences on the film properties. In order to assess the optimal recipe for the system, a series of depositions were performed at low pressure and increasing coil power from 300W to 600W in 100W increments. The complete set of non-variable parameters is listed in Table 5.5.

Table 5.5 - Fixed parameters used for FC films deposited with variable source power.

Film	Pressure (mTorr)	C_4F_8 flow rate (sccm)	Chuck temp. (°C)	Chuck bias (W)	Chuck position (mm)
FC	5	60	10	0	120

As shown in Fig. 5.9, the deposition rate was found to increase with power, from 1.3nm/s at 300W to 2.5nm/s at 600W. This can be explained by an increase in the number of reactive agents present in the plasma available to polymerize and form the FC film [130,135]. The Default recipe at a power of 1000W had the highest deposition rate. For the series of films deposited at low pressure, the contact angle was also found to increase with deposition power in accordance with results in the literature [122,135]. Labelle surmises that the combination of low pressure and high power produces plasmas with a high concentration of fluorine species and highly fragmented carbon species (e.g. C, C_2), leading to a two phase deposition process favouring CF_2 formation and thus increasing the hydrophobicity of the resultant film [135]. The

large increase in contact angle from 300W to 400W can be explained as the transition into the high power/ low pressure regime that favours high F:C ratio films.

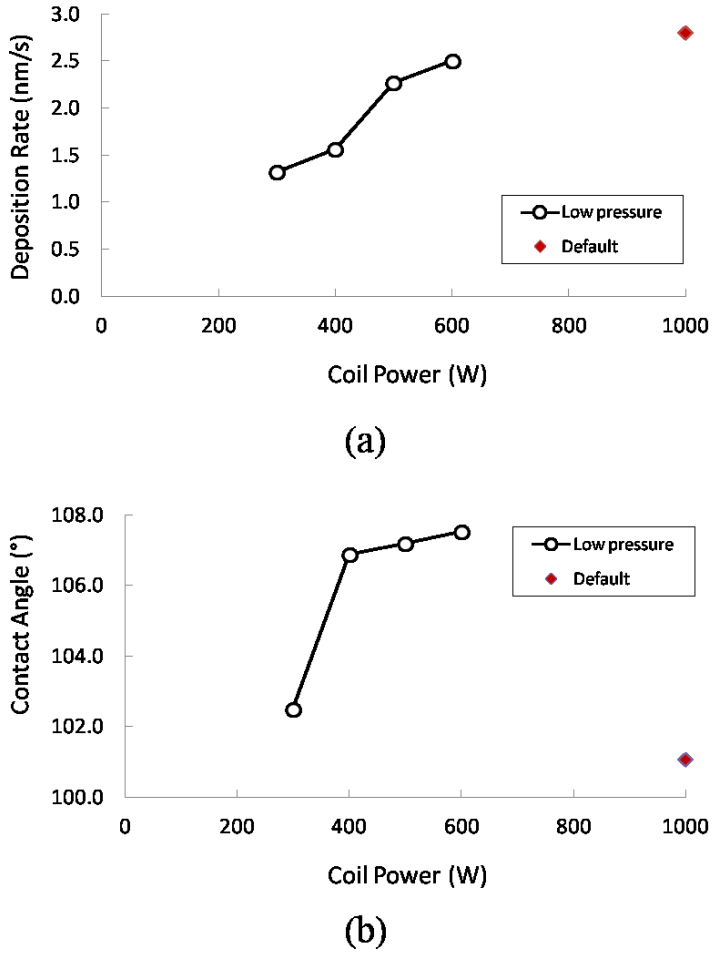

Figure 5.9 - The (a) deposition rate and (b) contact angle of fluorocarbon films deposited at low pressure (circles) and various coil powers. The results of the Default recipe (high pressure) are also indicated on the graphs as red diamonds.

The refractive index and extinction coefficient of the deposited films are listed in Table 5.6. It can be seen that, in general, increasing coil power results in a decreasing index of refraction. Indices were between 1.359-1.395 with relatively low extinction coefficients for the 400W, 500W and 600W recipes while the 300W recipe showed a significantly higher index and extinction coefficient. The higher index, extinction coefficient, and low contact angle

measurement of the 300W recipe indicate a sub-optimal stoichiometric composition of the film, likely the result of a low F:C ratio.

Table 5.6 - Optical constants at 550nm of various thin FC films deposited using the passivation cycle of the Bosch process in a RIE.

Coil Power (W)	n_{550}	k_{550}
300	1.775	0.149
400	1.395	0.017
500	1.385	0.019
600	1.359	0.019
Default	1.500	0.020

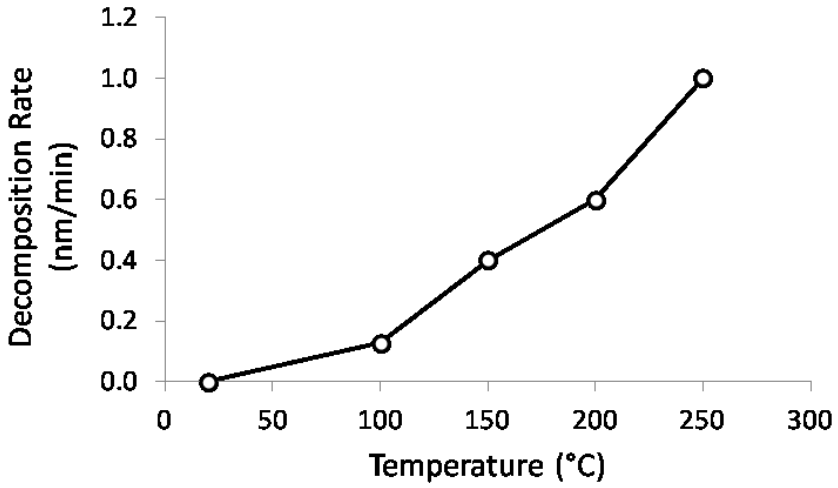

Figure 5.10 - The rate of decomposition of the fluorocarbon film produced at 600W. Profilometer measurements were performed after 10min of exposure at each temperature.

Based on the results above, the 600W recipe was selected for further testing to ensure process compatibility. First, a sample was placed in the sputtering system described in Sec. 5.2.1 and pumped down with the substrate heater set to 150°C, which is the temperature used for thin film deposition. The sample was then held at this temperature for 2h. Film thickness was measured before and after and was found to vary $\pm$10%. The step profile, however, was found to

be much smoother in the annealed sample. The thermal stability of the FC film was further examined by measuring the film thickness after 10min of exposure on a hot plate, at 50°C increments. The results are presented in Fig. 5.11 showing an increase in decomposition rate as the temperature is raised, agreeing well with results reported in other works [133]. Patterned features could not be visually located after exposure at temperatures above 250°C, indicating a rapid decomposition rate.

Fluorocarbon films deposited using the 600W recipe have characteristics, including hydrophobicity and refractive index, which closely match those of bulk PTFE. Furthermore, the thermal stability was measured and was predicted to be adequate for these films to survive the subsequent deposition of the top mirror. Moreover, the films are expected to decompose at moderate temperatures, an advantageous characteristic that allows a mechanism for further adhesion reduction during the buckling process [27]. This recipe was thus selected for full process testing, including patterning, upper mirror deposition and buckling experiments.

5.4 Buckling experiments

Following the optimization of both the low adhesion layer and optical thin films, full samples were prepared for buckling experiments, in order to test which high index material would produce the best results when combined with SiO_2. The full buckling procedure (see Fig. 5.1) using TiO_2/SiO_2 and Ta_2O_5/SiO_2 based mirrors was performed in parallel to reduce experimental variation between the samples and to allow a direct comparison of results.

The bottom claddings were deposited onto piranha-cleaned Si wafers using the optimized recipes developed in Sec. 5.2.3. The mirrors were designed using the QWS criteria with a centre wavelength of λ_{Bragg} = 550nm. In order to reduce fabrication time and complexity, 5-period mirrors were used in initial experiments. The mirrors were subsequently analyzed to determine the stress of the multilayer and to confirm optical characteristics. Samples were then sonicated in acetone to clean the surface before proceeding to the deposition and patterning of the fluorocarbon thin film.

5.4.1 Fluorocarbon Patterning

Fluorocarbon patterning was achieved using standard optical lithography and liftoff with the photoresist known as HPR-504. The mask used contains arrays of waveguides of various widths from 10μm to 80μm, as well as circles (which form buckled domes) and tapered sections (which produce tapered waveguides). Samples were spin-coated with the resist using a two step spread/spin cycle as detailed in Table 5.7, after which they were allowed to remain in atmosphere for 15 minutes to allow rehydration. Hexamethyldisilazane (HMDS), a compound used to promote adhesion between the substrate and photoresist, was found to cause the resist to adhere too well to the substrate. This led to the need for long processing times in order to adequately remove the resist, and resulted in poor quality features, such as those shown in Fig. 5.11 (a) and (b). Patterns in this case were observed to have rough edges or unwanted artifacts which significantly reduced device yield. Thus, the remaining samples described here were prepared without HMDS, which produced much improved results and had to no observable detriments. After hydration, samples were exposed using an ABM mask aligner which uses both i-line (365nm) and h-line (405nm) emission. Following exposure, samples were developed using Microposit 354 developer and then rinsed with DI water and dried using compressed N_2. Features were examined using an optical microscope and the resist thickness was measured using a contact profilometer to ensure consistency.

Table 5.7 - Spread/spin cycle for the HPR-504 photoresist.

	Spread	Spin
RPM	500	4000
duration	10s	40s

Samples were then loaded into the ICP-RIE system and, after chamber conditioning, a thin FC film was deposited using the optimized 600W recipe detailed in Sec. 5.3. The wafers were then sonicated in an acetone bath for 1 hour to remove the remaining photoresist, leaving behind the patterned FC layer in the shape of waveguides, circles, and tapers. These features define the shape of the buckling region and thus the geometry of the resultant waveguides. The wafers were then rinsed with DI water and dried with compressed N_2. Features were examined

carefully to ensure complete removal of the photoresist and assess the quality of the FC film. Fig. 5.11 (c) is an image of the patterned FC features, revealing smooth edges after liftoff. Fig. 5.11 (d) shows an entire wafer during the DI water rinse. The hydrophobic properties of the FC film are readily apparent as the water is seen beading into the regions void of the FC film. Inspired by results from Gnanappa *et al*. [124] some samples were annealed at 100°C for 1h to improve the stability and uniformity of the layer. Following patterning, the samples were loaded back into the sputtering system and a matching top mirror was deposited, embedding the FC layer between the two mirrors.

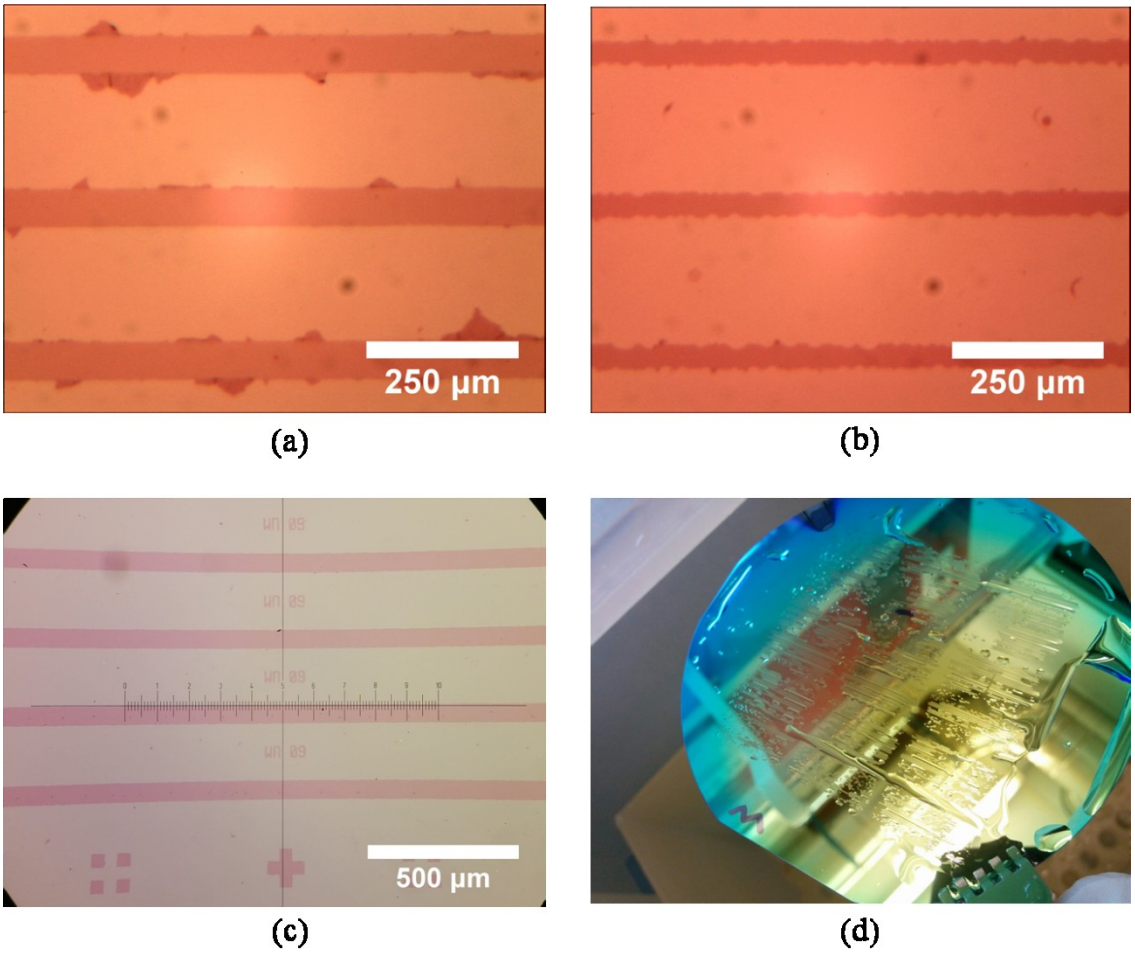

Figure 5.11 - Images of the patterned fluorocarbon thin film. (a-b) Poor quality features as a result of using HMDS to promote adhesion of the photoresist to the substrate. (c) Good quality features with straight edges. (d) A full wafer with the patterned FC film during the rinsing process. Water is filling the region void of the FC film, outlining the patterned regions and highlighting the hydrophobicity of the material.

5.4.2 TiO_2/SiO_2 sample

A summary of the processing parameters for this sample are presented in Table 5.8. A sputtered five-period TiO_2/SiO_2 distributed Bragg reflector was used as the bottom cladding. The low-loss recipe was chosen for the SiO_2 (see Sec. 5.2.3.1). The TE stopband of the bottom cladding is shown in Fig. 5.12. A ~30nm thick FC layer was patterned, and then a 4 period DBR was deposited as the upper waveguide cladding. For the upper mirror, the high stress SiO_2 recipe was used, and the multilayer was capped with a thick (~250nm) TiO_2 layer. The decision to cap the upper mirror with a thick TiO_2 layer was based on monolayer stress measurements, which yielded values > -300MPa for TiO_2, indicating that the addition of such a layer would increase the stress compared to using SiO_2 (see Table 5.1). The resultant stress of the top cladding was found to be -107MPa, which is somewhat lower than expected from an effective medium estimate based on the stress measured for single films.

Table 5.8 Processing parameters for the TiO_2/SiO_2 sample.

Bottom cladding thickness (nm)	Top cladding thickness (nm)	Top cladding stress (MPa)	FC film thickness (nm)	T_b (°C)
750	840	-107	30.2	317

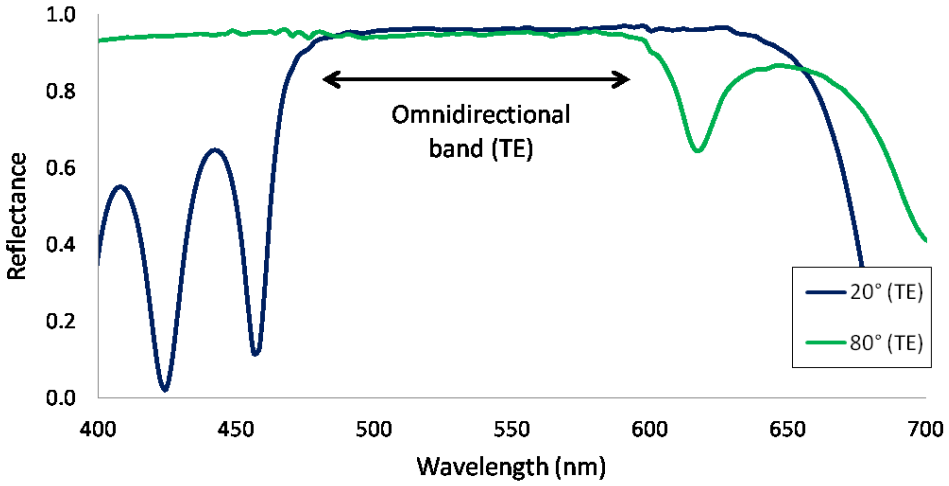

Figure 5.12 - Experimentally determined reflectance characteristics of the sputtered 5-period TiO_2/SiO_2 mirror with the (TE) omnidirectional band indicated. Results are for TE-polarized light at 20° and 80° incident angles.

The sample was subsequently cleaved into sections of size ~2.5cm^2 and prepared for buckling. Several methods were explored as a means to induce buckling, including the 'scotch tape' test [reference], sonication in an acetone bath, baking in a vacuum oven, and heating using a conventional hotplate. The hotplate proved most effective and was subsequently used for all other pieces. It is speculated that the heating begins to decompose the FC film, which further reduces the adhesion between the layer and the claddings [27]. The first sample was heated at a rate of ~ 25°C/min in an effort to determine the temperature for the onset of buckling, T_b, of the material combination. This was found to be ~317°C. To optimize the release mechanism, other samples were heated at varying rates such as 50°C/min, 100°C/min or placed on a preheated hotplate at the buckling temperature, T_b.

All samples were found to buckle to some degree, however, no defect-free pieces were obtained. Samples buckled by being placed on a 350°C preheated hotplate produced the most promising results, with long portions of waveguides appearing to buckle completely. The sample remained on the hotplate for 10 minutes during which time waveguide buckling continued on the smaller width waveguides while many of the larger width waveguides had features that completely delaminated and popped off. Upon further inspection it was found that the upper waveguide cladding had cracked and fractured in a wave pattern along the length of the buckled waveguides (see Fig. 5.13). The 60μm and 80μm waveguides were found to delaminate from the substrate as shown in Fig. 5.13 (c).

The cracking of the buckled film indicates a shift from compressive stress to tensile stress that causes strain on the film [136]. Figure 5.13 (d) presents a high magnification image of a cracked waveguide, along with micro fractures on the unpatterned regions of the TiO_2/SiO_2 film. A possible explanation for the film cracking is the following two step process. First, at high temperatures the compressive stress of the film can be baked out [27], leaving the sample with little, if any, compressive stress after initial buckling. Following this, the subsequent cooling back to room temperature can increase the tensile stress on the film and potentially cause the film to crack [136].

As discussed, the stress of the upper cladding was quite low (-107MPa), much less than a value of ~250MPa predicted using an effective medium analysis with stress values of 300MPa for TiO_2 and 200MPa for SiO_2. This discrepancy is likely the result of the variability of the TiO_2

film stress, which makes predicting the buckling results incredibly difficult. In view of this, consistent results using TiO_2/SiO_2 may not be feasible using the sputtering deposition equipment described.

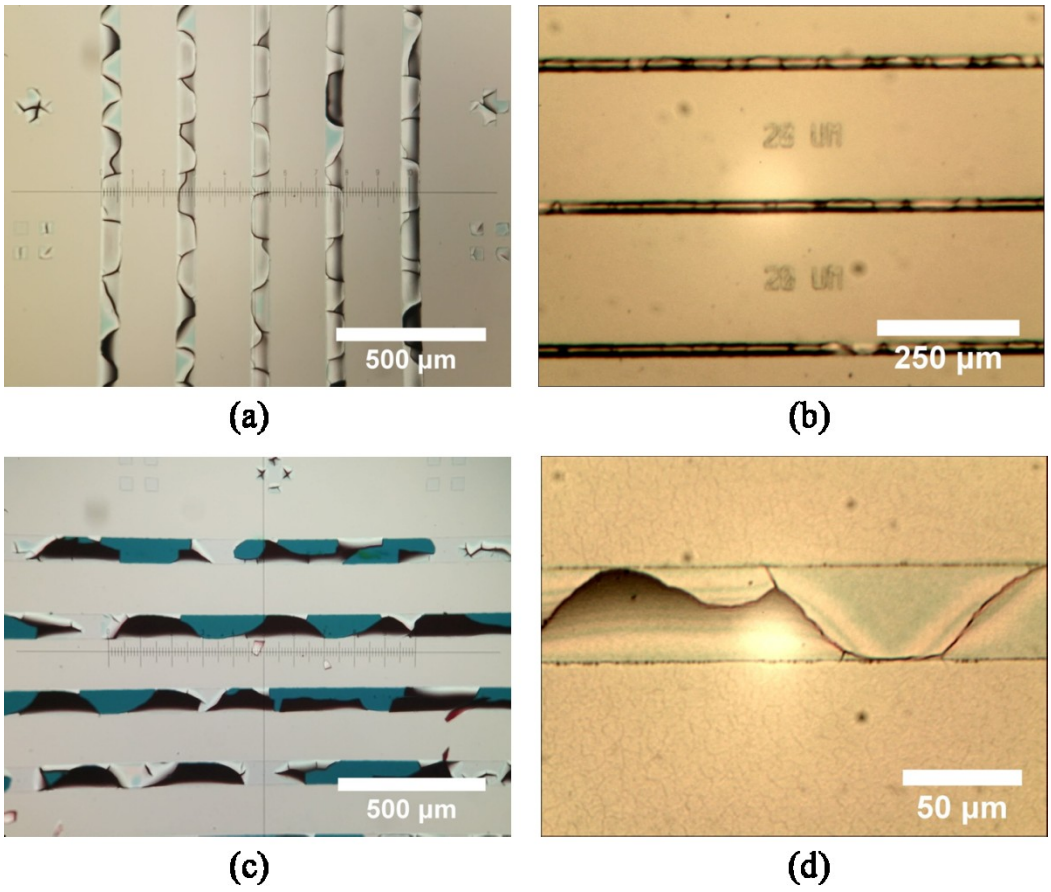

Figure 5.13 - Microscope images of TiO_2/SiO_2 buckled waveguides. (a) 40µm and (b) 20µm wide buckled waveguides with wave-like fractures. (a) 60µm wide waveguides with the upper cladding completely delaminated in some areas due to prolonged exposure to high temperatures. (b) High magnification image of a 60µm waveguide that has cracked. Micro fractures are also present in the film in the unpatterened regions.

5.4.3 Ta_2O_5/SiO_2 sample

The Ta_2O_5/SiO_2 sample was prepared in much the same way as the TiO_2/SiO_2 sample. The low-loss SiO_2 recipe was used for the 5-period bottom cladding. This was coupled with a patterned ~20nm thick FC film and topped with a 4.5-period upper cladding. A thick (~500nm) SiO_2 layer

was used to cap the top cladding in an effort to increase mechanical stability and prevent features from popping. Prior to the fluorocarbon patterning, variable angle spectroscopic ellipsometry (VASE) was employed to confirm the properties of the bottom mirror as shown in Fig. 5.14. The TE omnidirectional band is indicated and shown to span the wavelength range from ~520-580 nm. Some of the processing parameters of the sample are summarized in Table 5.8, including the stress of the upper cladding which was found to be -226MPa.

Table 5.9 - Processing parameters for the Ta_2O_5/SiO_2 sample.

Bottom cladding thickness (nm)	Top cladding thickness (nm)	Top cladding stress (MPa)	FC film thickness (nm)	Temperature for the onset of buckling, T_b
850	1275	-226	19.6	290

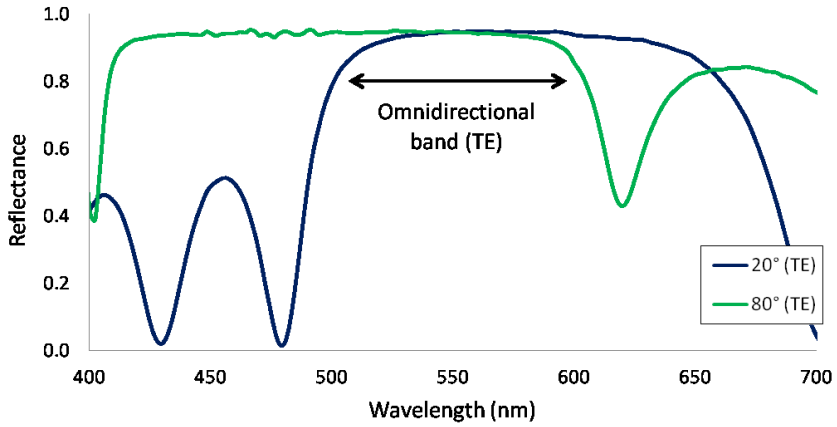

Figure 5.14 - Experimentally determined reflectance characteristics of the sputtered 5-period Ta_2O_5/SiO_2 mirror with the (TE) omnidirectional band indicated. Results are for TE-polarized light at 20° and 80° incident angles.

Similar to the results obtained with the TiO_2/SiO_2 sample, only heating with a hotplate produced buckled features. The temperature for the onset of buckling was found to be 290°C, slightly lower than that of the TiO_2/SiO_2 samples. Heating at a rate of 25°C/min was found to buckle only the 80μm wide waveguides, while rates of 50°C/min and faster were found to buckle the 40μm, 60μm and 80μm wide waveguides. In contrast to the results obtained with the

TiO_2/SiO_2 samples, buckling was found to continue even after prolonged exposure on the hotplate with no features popping off. Upon initial inspection it was found that the vast majority of 40μm, 60μm and 80μm wide waveguides buckled into straight sided Euler columns, while no visible buckling was found for the 10μm and 20μm wide waveguides. Waveguide defects were found at locations of FC film defects or where buckling at opposite ends of the same waveguide occurred and these fronts met, forming notches (see Fig. 5.15 (a)). Further exposure on the hotplate at high temperature (>350°C) acts to anneal the sample, and was observed to smooth out the notches.

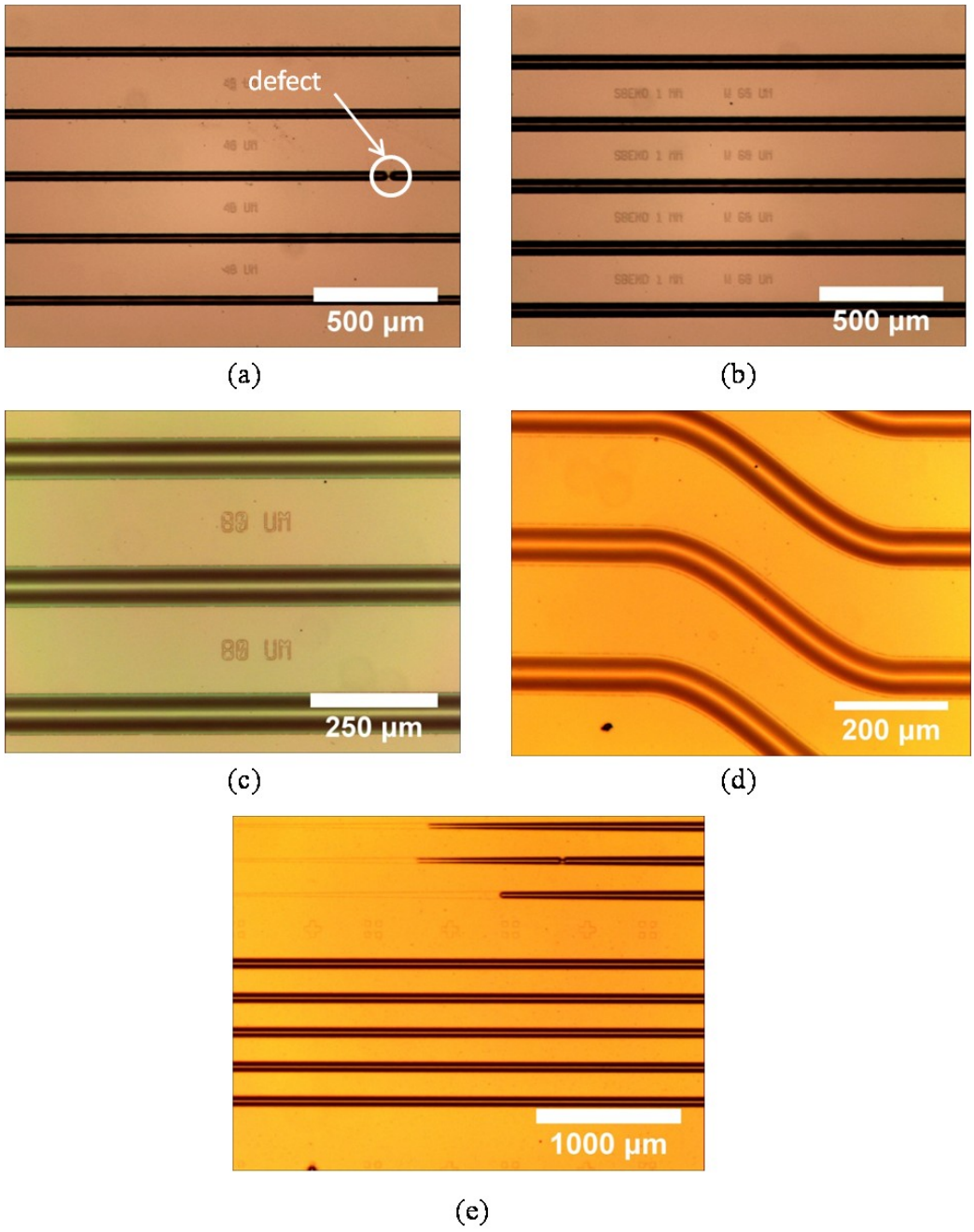

Figure 5.15 - Microscope images of Ta_2O_5/SiO_2 buckled waveguides. (a) An array of 40µm wide waveguides. A 'notch' defect is indicated by the circle. Arrays of (b) 60µm and (c) 80µm wide waveguides. Other geometries such as (d) s-bends and (e) tapers were also found to buckle, at least partially in the latter case.

Figure 5.15 (a)-(e) depicts examples of buckled waveguides of varying width and with geometries such as s-bends and tapers. From optical and contact profilometer scans, the peak height of the buckles was found to vary [8] from ~600nm for 40µm wide waveguides to ~2.6µm for 80µm wide waveguides (see Fig. 5.16). Variation in peak buckle height was the result of variances in the upper mirror thickness as well as in the speed and duration of the heating step. Using Young's modulus values of 40 GPa and 140 GPa, and Poisson ratios of 0.17 and 0.23, for SiO_2 and Ta_2O_5 respectively [137–139], the peak buckle height predicted by elastic buckling theory (see Sec. 2.3) is also presented in Fig. 5.16 (b), and shows close agreement with the measured values. It can be seen that waveguides with widths less than ~35µm are not predicted to buckle, consistent with observations. An effective medium approach was used in calculations, with an estimated composition of ~75% SiO_2 and ~25% Ta_2O_5. Elastic buckling theory was also utilized to assess the stress ratio, σ_0 / σ_c, and is presented in Table 5.9. The calculated stress ratios for 40µm, 60µm and 80µm wide waveguides are all < 6.5 indicating that buckle morphology is dominated by straight sided Euler columns as observed in Fig. 5.15. Experimental verification of the effective Young's modulus and Poisson ratio of the deposited multilayers is the subject of ongoing work. Overall yield of defect free waveguides was as high as ~ 60%.

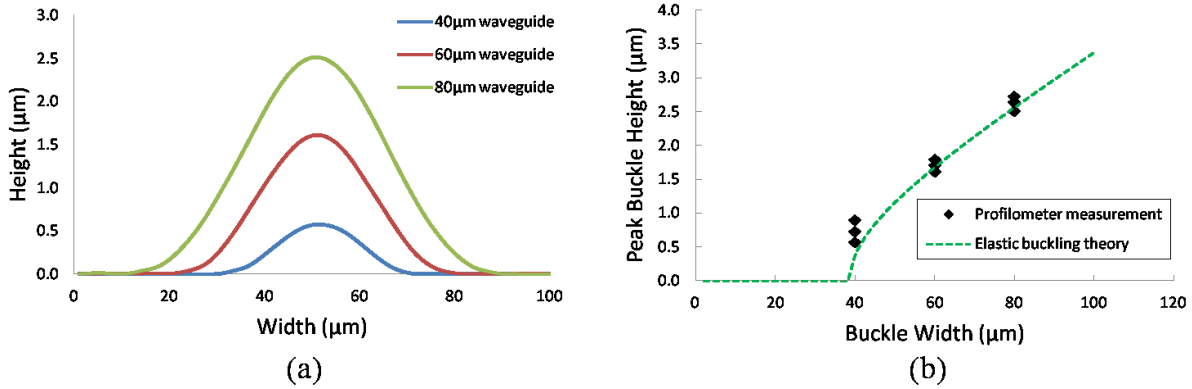

Figure 5.16 - (a) Contact profilometer scans of 40µm, 60µm and 80µm wide waveguides. (b) The peak buckle height of numerous waveguides (symbols) and the predicted buckle height according to elastic buckling theory (dashed line) using stress and film thickness values indicated in Table 5.8 and an effective Young's modulus of 65 GPa.

Table 5.10 - The stress ratio, σ_0 / σ_c, predicted by elastic buckling theory for regions of various widths for the deposited sample with an effective Young's modulus of 65GPa.

Buckle Width (μm)	σ_0/σ_c
40	1.05
60	2.38
80	4.22

5.5 Conclusions

The development of a platform used to fabricate hollow buckled waveguides was detailed. Sputtering was the thin film deposition method of choice owing to the ability to control thin film stress, which is necessary to ensure straight sided Euler column growth. Individual recipes were developed for each of the prospective optical thin film combinations, in an effort to produce multilayers with high compressive stress and low optical loss. A patterned fluorocarbon thin film was utilized as a low adhesion layer. Films deposited in an ICP-RIE system using a combination of relatively high power and low pressure were found to have suitable properties for the buckling fabrication process, and also similar characteristics to that of bulk PTFE. Buckling experiments were carried out using samples based on TiO_2/SiO_2 and Ta_2O_5/SiO_2 multilayers. An optimized heating step was used to further reduce the adhesion of the embedded fluorocarbon layer and drive the buckling process. The Ta_2O_5/SiO_2 samples produced far superior results, with straight sided Euler buckles forming for waveguides with widths 40μm, 60μm and 80μm. Prolonged exposure to heat proved advantageous to smooth out defects present in the waveguides, with overall yield was as high as ~ 60%. The morphology and peak buckle height of waveguides was consistent with the predictions of elastic buckling theory.

Based on the results obtained, the Ta_2O_5/SiO_2 combination was chosen as the material platform for future hollow-core optical devices. Chapter 6 details the fabrication and optical performance of a further refined process using 10 period mirrors.

Chapter Six: Visible range hollow waveguides by guided buckling of Ta_2O_5/SiO_2 multilayers

6.1 Introduction

This chapter describes second generation prototype waveguides fabricated using the set of processes detailed in Chapter 5. Waveguides with 10-period Ta_2O_5/SiO_2 claddings were successfully implemented using the controlled buckling technique, and were shown to have optical properties (loss, bandwidth, etc.) that are in good agreement with theoretical predictions. The contents of this chapter were published in Applied Optics [140].

6.2 Background

On-chip hollow waveguides and microcavities are attracting interest for applications in lab-on-a-chip (LOC) sensing systems [3,141] and fundamental quantum coherence studies [4,5]. This is motivated by the possibility to confine or guide light within a gas or liquid medium, and by the potential to tune these optical devices using integrated actuation mechanisms [6].

Traditionally, on-chip hollow core structures have been fabricated using either sacrificial etching [4] or wafer-bonding [6] techniques as described in Chapter 2. We have previously reported an alternative approach, in which hollow Bragg waveguides [27] and Fabry-Perot microcavities [8] were fabricated through the guided formation of delamination buckles within a multilayer thin film stack. This approach is essentially a surface micro-machining technique, but does not require the removal of a sacrificial material. It enables parallel fabrication of diverse functional structures, including straight and tapered [7] waveguides and high-finesse dome-shaped microcavities [8]. To date, these buckled devices have been limited to operation in the infrared region ($\lambda > 1000$ nm) due to the materials employed (e.g. high-index amorphous silicon layers [27]).

Visible or near-visible range operation is required to address many of the most compelling applications for hollow-core integrated optics devices. These applications include fluorescence detection in LOC systems [3] and quantum electrodynamics (QED) studies with alkali atoms [4–6]. Here, we report visible-band, Ta_2O_5/SiO_2-based hollow waveguides

fabricated by buckling self-assembly. As a high-index material, Ta_2O_5 has numerous attractive attributes, including low intrinsic photoluminescence [11], low loss in the visible and NIR ranges, high index (n ~ 2.2), excellent mechanical properties, and very good predictability and controllability for thin film deposition [75]. Many of the ultra-high reflectance 'supermirrors' reported in the literature employ Ta_2O_5 combined with SiO_2 [34,89].

6.3 Fabrication

The detailed fabrication procedure is described in Chapter 5. A brief description of the process is as follows. First, a distributed Bragg reflector (DBR) is deposited onto a silicon substrate. Next, a low adhesion layer (LAL) is deposited and patterned by liftoff. Subsequently, a second DBR is deposited under conditions that produce a desired level of compressive stress. Lastly, an empirically optimized temperature ramp is used to induce loss of adhesion between the LAL and top multilayer, such that the top multilayer buckles over the regions of the LAL. By varying the size and shape of the LAL, it is possible to produce straight, curved, and tapered waveguides, as well as dome-shaped cavities [8].

Initially, single layers of Ta_2O_5 and SiO_2 were deposited and studied in order to verify optical characteristics and optimize stress. Deposition parameters are summarized in Table 1, along with some properties of the optimized films. The films were deposited using a 3-source magnetron sputtering system equipped with a pulsed DC power supply (AE Pinnacle Plus). The process chamber was evacuated to a base pressure of $<1\cdot10^{-6}$Torr before all depositions. Substrate temperature (150°C) and deposition pressure (4mTorr) were held constant. Both Ta_2O_5 and SiO_2 films were reactively sputtered, with Ar and O_2 flow rates controlled by a mass flow controller (MKS Type 647C). Ta_2O_5 films were deposited using a 99.95% pure Ta target with gas flows rates of 40sccm (Ar) and 20sccm (O_2). SiO_2 films were deposited using a 99.999% pure Si n-type target with gas flow rates of 50sccm (Ar) and 3.2sccm (O_2).

Optical characteristics were determined using a variable angle spectroscopic ellipsometer (VASE), and film stress was measured using a Flexus stress measurement system. Both films exhibited low loss ($k<10^{-5}$) and moderately high compressive stress.

Table 6.1 - Deposition parameters and film properties for Ta_2O_5 and SiO_2 thin films

Material	Power (W)	Freq. (kHz)	Duty Cycle (%)	Target Bias (V)	$O_2/(O_2+Ar)$ flow ratio	Dep. rate (nm/min)	n_{550}	k_{550}	Film Stress (MPa)
Ta_2O_5	200	20	90	540	0.33	10	2.21	$< 10^{-5}$	-230
SiO_2	200	150	88	485	0.06	17	1.46	$< 10^{-5}$	-200

The optimized process parameters described above were subsequently applied to the fabrication of hollow waveguides. First, a 10-period Ta_2O_5/SiO_2 multilayer, terminating with Ta_2O_5, was reactively sputtered onto a piranha-cleaned silicon substrate. Nominal layer thicknesses were chosen to satisfy a quarter wave stack condition at a wavelength of 550nm. Figure 6.1 shows reflectance characteristics for TE-polarized light, both as measured using the VASE and as predicted by transfer matrix simulations. The simulations used the optical dispersion functions extracted from measurements on the single films. The experimental results agree quite well with the predicted results. Residual discrepancies are likely due to slight variations in layer thicknesses and indices. The index contrast is not sufficiently high to produce a complete omnidirectional reflection band for both TE and TM-polarizations. However, an omnidirectional band for TE-polarized light is verified in the wavelength range ~510-570nm. Peak reflectance at normal incidence is predicted to be R=0.999. For the waveguides discussed below, the low-loss propagation band is expected to closely match the reflection band at the near-glancing incident angle (80 degrees) shown. At this angle, the simulations predict peak reflectance R_{80} = 0.9999.

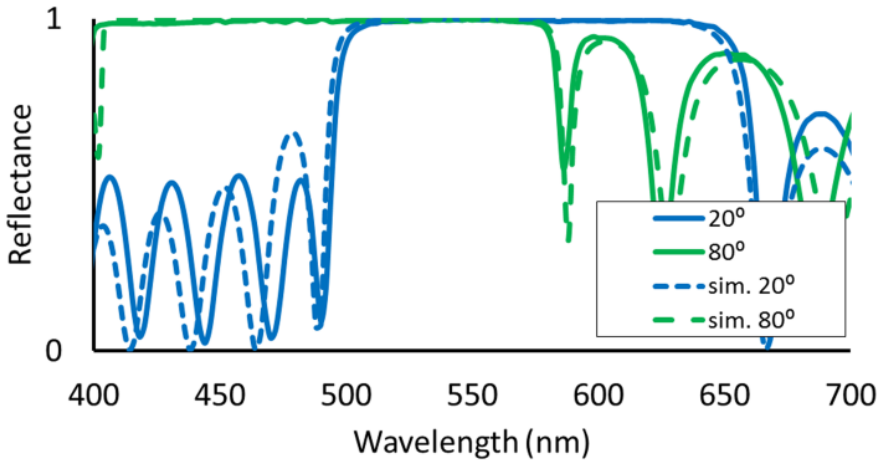

Figure 6.1 - Experimental (solid lines) and predicted (dashed lines) TE reflectance results for the 10-period bottom mirror are shown for two different angles of incidence.

A C_4F_8 based polymer was chosen as the LAL. This material has been found to have low pin-hole density, low surface energy, and sufficient mechanical robustness to survive subsequent patterning and deposition [8,129,131,133]. The polymer was deposited using an inductively coupled plasma reactive ion etch system (Oxford). Through variation of the deposition parameters, efforts were made to maximize the hydrophobicity of the fluorocarbon film on a Ta_2O_5 surface. In particular, it was found that a combination of relatively high deposition power (600W) and low deposition pressure (5mTorr) produced optimal results, consistent with other works [130,135]. Hydrophobicity was assessed by observing the water contact angle, which was measured to be >110° for optimized films. Films ~20nm thick were deposited and patterned on top of the 10-period mirror, using lithography and lift-off of a standard photoresist.

A second 10.5-period mirror was subsequently deposited on top of the patterned fluorocarbon layer. In order to enhance mechanical robustness and increase compressive stress, the top mirror was terminated with a thick (~500nm) layer of SiO_2. Measurements of the top mirror stress yielded a value of -230MPa, in reasonable agreement with an effective medium calculation based on the stress of the individual layers.

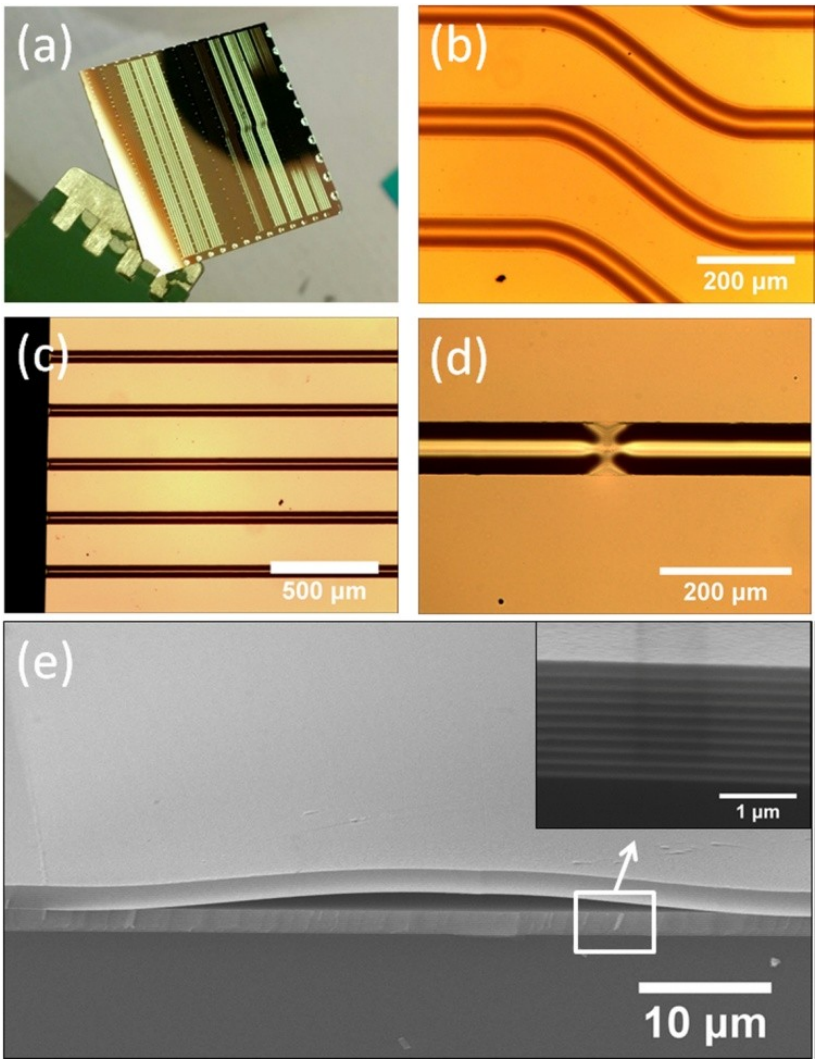

Figure 6.2 - Images of buckled waveguides. (a) Image of a 2.5cm^2 chip containing waveguides and s-bends of various widths. (b) High magnification image of 60µm wide buckled s-bends. (c) Low magnification image of a cleaved chip containing 60µm wide buckled waveguides. (d) High magnification image of a 60µm wide waveguide with a typical notch defect, the buckle height is greatly reduced at the location of the notch. (d) SEM image of the cleaved facet of a 60µm wide waveguide. Inset: SEM image of the multilayer structure of the bottom cladding.

Samples were then subjected to a heating step, which reduces the adhesion between the mirrors and embedded fluorocarbon layer [27]. The result of this process is that the compressively stressed upper mirror buckles in the regions defined by the fluorocarbon layer,

producing hollow waveguides with Bragg reflector claddings. Samples were heated on a hotplate in atmosphere up to ~250°C and kept at that temperature until uniform buckling across the entire sample was observed. We speculate that the prolonged exposure to high temperatures acts to decompose the embedded fluorocarbon layer [133]. The ultimate fate of the material is the subject of ongoing research. Figure 6.2 depicts examples of buckled waveguides of varying width and geometries, including s-bends. From optical and contact profilometer scans, the peak height of the buckles was found to vary [8] from ~1.1μm for 40μm wide waveguides to ~3.6μm for 80μm wide waveguides (see Fig. 6.3(a)). Height variation between buckles of the same base width was found to be within 10%, and features were very symmetrical in all cases. From elastic buckling theory the peak height of a straight-sided delamination buckle is predicted to be [54]:

$$\delta_{\max} = h\sqrt{\frac{4}{3}\left(\left(\frac{b}{b_{\min}}\right)^2 - 1\right)}, \tag{5.1}$$

where h is the thickness of the buckled film, b is the half width of buckle and b_{min} is the minimum half-width for the onset of buckling. Furthermore, in the range $b>>b_{min}$:

$$\delta_{\max} \approx \frac{2h}{\sqrt{3}}\frac{b}{b_{\min}}, \tag{5.2}$$

implying that the peak buckle height varies linearly with the buckle width. Figure 6.3(b) verifies this linear trend for the as-fabricated 40μm, 60μm, and 80μm wide waveguides. An in-depth investigation into the mechanical properties of the materials, and thus the exact details of the buckling process, is the subject of ongoing work.

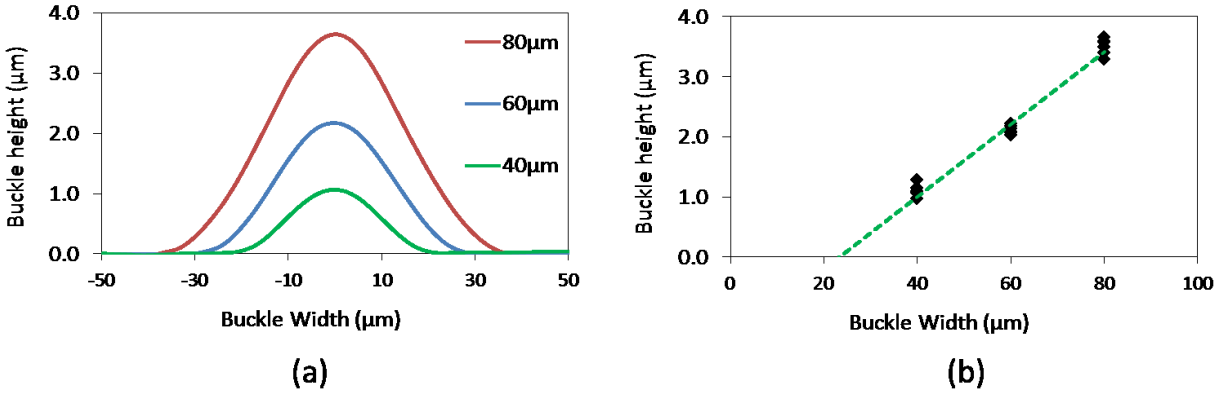

Figure 6.3 - (a) Contact profilometer scans of 40µm, 60µm, and 80µm wide waveguides. (b) The symbols indicate the measured peak height of numerous buckled waveguides. The green line is a linear fit to the data.

After buckling, the silicon substrate was cleaved into chips containing arrays of waveguides ~4-6mm in length. A microscope image of a cleaved chip containing 60µm wide waveguides is shown in Fig. 6.2(c). A SEM image of the cleaved facet of a 60µm wide waveguide is shown in Fig. 6.2(e), the inset depicts the Ta_2O_5/SiO_2 multilayer structure. In initial process runs, overall yield of defect-free features was found to be ~50-60%. The majority of defects were the result of incomplete buckling, resulting in "notches" in the waveguides (see Fig. 6.2(d)). At the notches, the core height and width are greatly reduced, such that these defects act as scattering centers for guided light. The number of defects increased with radial distance from the center of the wafer, indicating that non-uniformities in the top multilayer (which in turn would lead to variance in compressive stress across the wafer) or the fluorocarbon film are probably contributing factors. It should be possible to increase the yield of defect-free waveguides significantly, both through optimization of the film uniformity and through optimization of the fluorocarbon layer, such as by introducing an annealing step [124].

6.4 Optical characterization

Given the high reflectance of the 10-period Bragg mirrors, the existence of low-loss, air-guided modes is anticipated. As we have discussed previously [29], the buckled waveguides have low height-to-width aspect ratios, and their guidance properties are generally well predicted using

slab waveguide models. For example, using a hard-boundary approximation, the ray bounce angle associated with a fundamental air-guided slab mode can be estimated as $\phi(\lambda_0) \sim \cos^{-1}(\lambda_0/2d)$, where λ_0 is the free-space wavelength and d is the thickness of the air core (i.e. spacing between the Bragg claddings). Furthermore, the leaky waveguide loss can be estimated as $\alpha \sim -(5\lambda_0/d)\log(R)$ [dB/cm] [21], where R is the cladding mirror reflectance at the ray bounce angle associated with the mode of interest. For the waveguides discussed below, d ~2 μm, so that ϕ ~80 degrees at λ_0 ~550 nm. Furthermore, using $R_{80} = 0.9999$ from above, it follows that $\alpha < 1$ dB/cm might be possible. This analysis neglects the impact of scattering losses and higher-order modes, but provides useful context.

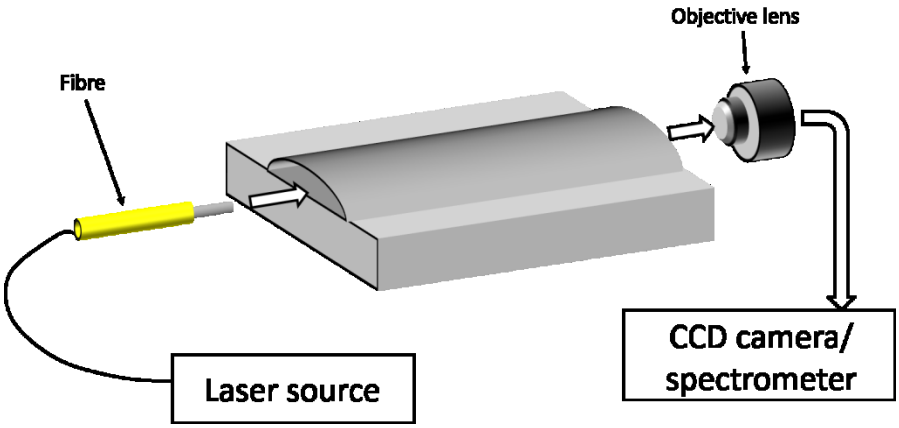

Figure 6.4 - Depiction of the experimental setup. Various laser sources where coupled to the waveguide input facet. Optical detectors affixed with detection optics were positioned at the output facet to verify light guidance and observe mode structure.

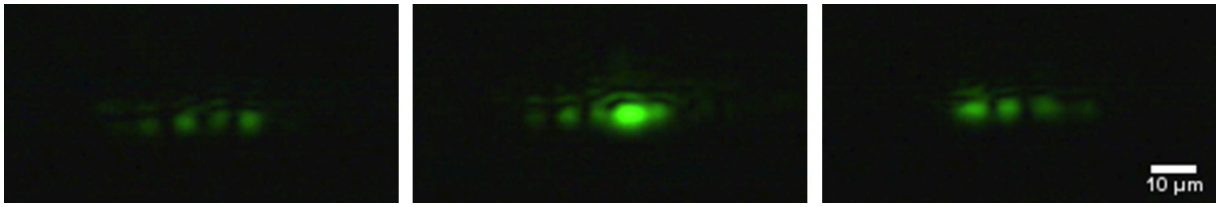

Figure 6.5 - Images of the end facet of a 40μm wide waveguide (height 1.1μm) for varying input coupling conditions of a 543nm laser source. All modes observed at the output facet were characterized by a single lobe in the vertical direction.

A supercontinuum white light source (Koheras SuperK Red) and a 543nm green HeNe laser were used for experiments on the guiding characteristics of the waveguides. Light from the sources was coupled to a standard single mode fiber (SM 450, Thorlabs), which was in turn coupled to the waveguide input facet (see Fig. 6.4). Cameras were placed above the waveguide and at the output facet in order to verify light guidance and to observe the mode structure.

Waveguides of base width 40µm, 60µm, and 80µm were studied. Due to the lower cladding reflectance for TM-polarized modes, these waveguides have very high polarization-dependent-loss (PDL) [8]. This was verified by controlling the polarization of the source, and it was found that only TE-polarized light is present in guided modes at the output facet. Figure 6.5 depicts various guided TE modes preferentially excited by varying the position of the coupling fiber relative to the waveguide input facet, and using the 543 nm wavelength source.

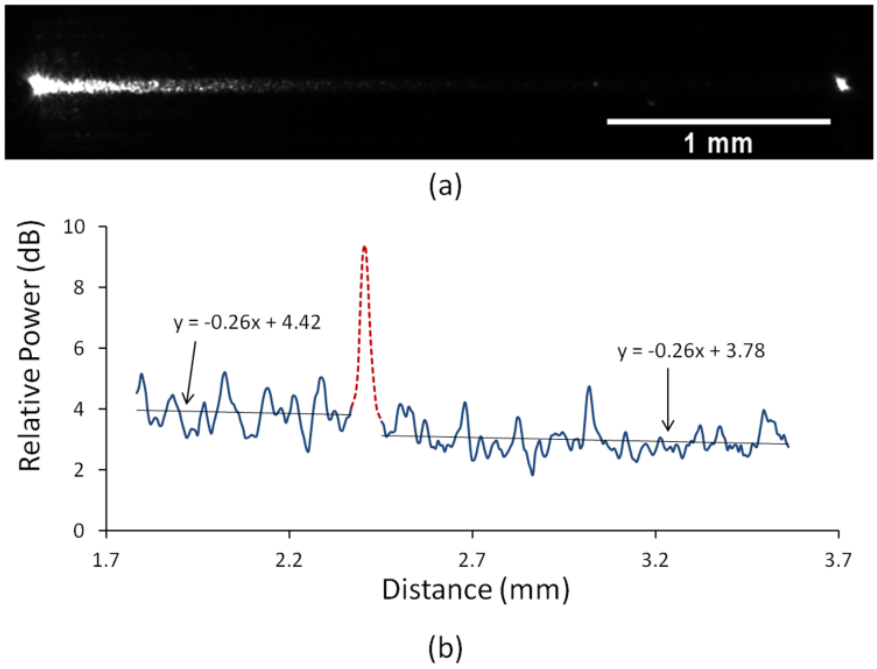

Figure 6.6 - (a) Top view of a 60µm waveguide illuminated with 543nm laser light. The laser is fiber-coupled to the input facet (left) of the waveguide. The bright spot on the right is the output facet. (b) Typical plot of scattered light at 543 nm versus distance along a waveguide. The black line is a linear fit of the data indicating a loss of ~2.6dB/cm. A defect was present over the integration region causing scattering (dotted red line) and was excluded from the linear fit calculation.

To estimate the loss of the waveguides, scattered light images were captured using a camera affixed with a low NA optic. Figure 6.5(a) shows a typical image captured with the 543nm laser source coupled into a waveguide of 60μm base width, 2.0μm peak height, and height variation less than a few percent (as determined from profilometer scans) along the length of the waveguide. The input and output facets of the waveguides are clearly visible as bright spots on the left and right, respectively. The short section of relatively bright and rapidly decaying scattered light near the input facet can be attributed to light coupled into high order modes of the waveguide. Following this initial decay, the scattered light streak is barely visible and relatively uniform over the remainder of the waveguide length. This low scattering intensity, along with the very bright spot visible at the output facet, indicates low propagation loss. Figure 6.5(b) shows the pixel response of the camera plotted versus distance along a typical section of the waveguide, revealing intensity decay on the order of ~2.6 dB/cm. This level of loss compares favorably to results reported previously for Ta_2O_5/SiO_2-based hollow waveguides [11]. Loss estimates from measurements of multiple waveguides was in the 1 to 7 dB/cm range, with variations often attributable to poor input facets or large scattering centers associated with the defects mentioned above. Nevertheless, the measured loss is in reasonable agreement with the analytical prediction from above and the modeled results below.

In order to assess the spectral dependence of the propagation loss, we used a transfer-matrix based slab model described in detail elsewhere [7,58]. Propagation loss versus wavelength was calculated for the fundamental TE mode of a symmetric, air-core slab waveguide clad by mirrors with the parameters described above. As mentioned, the slab model is reasonably valid for the buckled waveguides due to their high width-to-height ratio. In addition, as shown in Fig. 6.5, the low loss guided modes tend to exhibit a single lobe in the vertical direction, which makes it reasonable to use the fundamental TE mode approximation.

In the model, the height of the air-core was set to the measured peak height of the buckled waveguides and optical properties of the materials were set to match values acquired from VASE scans of the individual layers. Assuming lossless layers (k~0), α ~0.01 dB/cm at 543nm is predicted. With the extinction coefficients estimated from the VASE measurements included, the model yielded a loss estimate of α ~0.2 dB/cm. The model also predicts a broad transmission band ranging from 400-570nm, essentially spanning the range of high reflectance

for TE-polarized light incident at near-glancing angles on the cladding mirrors (see Fig. 6.1). The discrepancy between the predicted and experimental losses is likely attributable to several factors. First, it is possible that the loss in the multilayer may be higher than that estimated from the monolayer samples of Ta_2O_5 and SiO_2. Second, for low loss waveguides (<1.0dB/cm) the light scattering method of loss estimation can prove unreliable [142]. This is due to the low signal to noise ratio that typically results when defect centers become the predominant source of scattered light (see Fig. 6.5(b)). Additionally, the model neglects fabrication non-idealities such as scattering from defects due to the height non-uniformity along the length of individual waveguides. Finally, it should be noted that the buckled waveguides are channel waveguides, and only approximately represented by a slab waveguide model.

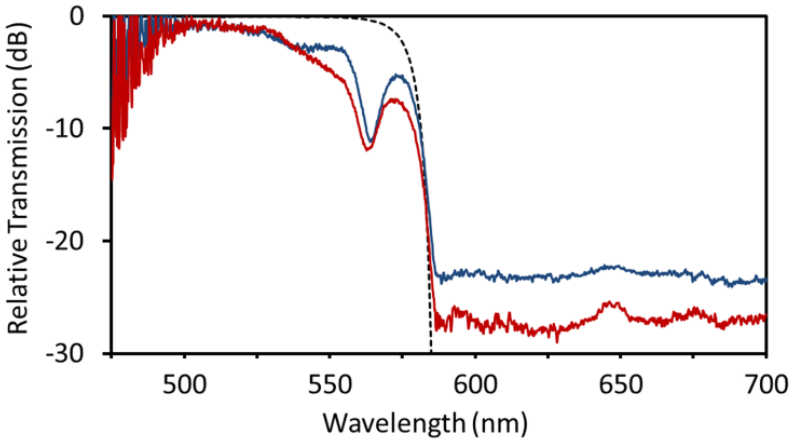

Figure 6.7 - The experimentally determined tranmission spectrum of two waveguide samples with peak core height of ~2.0µm and base width of 60µm (solid lines) and the predicted propagation loss for the fundamental TE mode (dashed line).

The supercontinuum source was used to experimentally assess the spectral characteristics of the waveguides. In this case, a commercial spectrometer (Ocean Optics USB4000), coupled via an objective lens and iris, was placed at the output facet of the waveguide. Figure 6.6 shows the normalized transmission spectra for two waveguides with peak core height of 2.0µm and base width of 60µm. A transmission band spanning ~500-570nm was observed, aligning well with the long wavelength edge of the transmission band predicted by the model. Spectral response below ~480nm was found to be too noisy for interpretation. This is attributable to the supercontinuum source used, which does not have significant power spectral density below ~490nm. A sharp dip

at ~560nm was observed in the transmission spectrum of all the measured waveguides. We postulate that this is likely due to leakage of light through the curved sidewalls of the buckled waveguides, as discussed in detail elsewhere [27], and not taken into account by the slab waveguide model.

6.5 Discussion and Conclusion

We described hollow-core waveguides operating in the visible wavelength range, fabricated by controlled thin film buckling of Ta_2O_5/SiO_2 multilayers. Device yield of defect-free waveguides was in the 50% range, most likely limited by non-uniformities in the mirror layers and the low adhesion layer. The waveguides exhibit a transmission spectrum between ~500-570nm, with loss ~2.6dB/cm at 543nm. Using these materials, devices could be fabricated for operation at any wavelength in the visible spectrum, by simply adjusting target layer thicknesses. This could make these devices of great interest for applications involving the optical integration of gas- and liquid-phase media for sensing and fundamental physics studies.

Chapter Seven: Conclusion and future work

7.1 Summary

The focus of this thesis was the development of alternative fabrication processes for realizing integrated hollow Bragg waveguides. As detailed in Chapter 3, a wafer bonding method was initially explored, and was successfully used to fabricate tapered hollow Bragg waveguides. These tapered waveguides were used to assess the spectroscopic sensing capabilities of hollow Bragg waveguides, and in particular the potential usefulness of the devices for microfluidic integration. Three dimensional guiding was facilitated by the fabrication of ridge waveguides with Bragg reflector claddings. As a dispersive element, the experimentally determined resolution of the tapered waveguides was as low as ~0.9nm in the 550 nm wavelength region. Emission from two types of fluorescent microspheres was coupled into the devices and their spectrum was extracted. The extracted spectra agreed reasonably well with those measured using a commercial spectrometer. In an attempt to improve the extracted spectra, a correction factor was applied to remove the 'instrument' response of the system. The limited operating range of the devices reduced the practicality of applying such a correction.

Chapter 4 describes a bandpass filter and polarizer fabricated using the wafer bonding techniques described in Chapter 3. The filter utilizes resonant tunneling through an embedded air gap layer in the frustrated total internal reflection regime. The design consists of a phase matching layer coupled with quarter wave stacks surrounding the air gap, facilitating admittance-matched tunneling centered at the design wavelength. By adjusting the layer thicknesses or material combination the design can be tuned to various wavelength ranges. Si/SiO_2 based devices were fabricated and were shown to have a polarization dependant passband with bandwidth on the order of 10nm in the 1550nm range, consistent with predicted results. Peak transmittance on the other of 80% and optical density greater than 5 over most of the near infrared region was also observed. The unique characteristics of the device allows for separation by both wavelength and polarization and could help develop novel optical systems.

The wafer bonded devices demonstrated the spectroscopic sensing capabilities of tapered hollow Bragg waveguides. However, to realize a fully integrated solution, the controlled

buckling of Bragg multilayers was investigated as an alternative fabrication method. The successful adaptation of the guided-buckling technique to devices operating in the visible range was detailed in Chapters 5 and 6. The process is dependent on the upper cladding having the appropriate amount of compressive stress to favor straight-sided Euler column growth. To achieve this, each material underwent an optimization process to create recipes to favor high stress while maintaining adequately low optical loss. To define the regions of buckling, a patterned fluorocarbon thin film was utilized as a low adhesion layer. This thin-film material has many characteristics that make it favorable for the buckling process, including low pin-hole density, low surface energy, adequate adhesion to survive the patterning process, and good chemical stability. Films were deposited using an ICP-RIE system with best film properties deriving from a recipe having relatively high deposition power and low pressure. Buckling experiments were carried out using samples based on TiO_2/SiO_2 and Ta_2O_5/SiO_2 multilayers. Following the patterning of the LAL and deposition of the upper cladding, an optimized heating step was used to further reduce the adhesion of the embedded fluorocarbon layer and drive the buckling process. Ultimately, the repeatability and good mechanical characteristics of the Ta_2O_5-based multilayers produced far superior results, with straight sided Euler buckles forming for waveguides of various widths.

To improve the guiding characteristics of the hollow waveguides, 10-period Ta_2O_5/SiO_2 samples were produced, resulting in claddings with peak reflectivity of ~99.9% at normal incidence. Straight-sided Euler columns were produced and buckle morphology was found to be consistent with results predicted by elastic buckling theory. Device yield was found to be as high as ~60%, with typical failure due either to notches in the waveguides or to complete delamination of the upper cladding. To date we have achieved a minimum waveguide loss of 2.6dB/cm for 543nm wavelength light guidance. A guidance band spanning ~500nm-570nm was observed, in good agreement with the theoretical predictions. Several process runs have produced consistent results, laying the foundation for interesting and unique experiments and applications involving visible-range hollow waveguides.

7.2 Future work and applications

With a stable fabrication process in place, future work can focus on refining the steps described in this thesis and adjusting the process to suit specific applications. Device yield can be increased by improving the fluorocarbon film uniformity. This can be achieved by investigating the effects of deposition temperature and the distance of the substrate from the glow discharge in the ICP-RIE. Additionally, the notches in the buckled hollow waveguides can likely be eliminated by driving the buckling of long waveguides preferentially at one end. To improve mechanical stability and increase the likelihood of clean end facets, a material such as Parylene or an optical adhesive may be used at a protective overlayer [29]. Lastly, more complex multilayer systems may be designed to increase the operating rage of the waveguides [143].

The above refinements can occur in parallel with the direct application of the devices for specific purposes such as fluorescence sensing in microfluidic systems. Having demonstrated the guiding characteristics and wavelength discrimination capabilities of the hollow Bragg waveguides, the next step would be to perform guiding experiments with liquid analytes in the hollow cores. Specific experiments could include determining the detection limits of the platform and exploiting the mainly TE-polarized nature of the waveguides for integrated filtering of the excitation light. Following that, one goal would be to develop integrated devices complete with liquid reservoirs and microfluidic channels. Furthermore, an integrated CCD sensor or cell phone with analysis software could potentially be coupled to the tapered waveguide spectrometer to allow on-demand spectral analysis in a portable fashion [144].

Another promising avenue of research is the exploration of quantum electrodynamics studies. Integrated hollow waveguides allow for optimized light-atom interactions, due to increased optical interaction lengths and increased nonlinearities [4]. Additionally, the same buckling process described in this thesis has be used to fabricate high quality optical microcavities [145] which are amongst the most important optical elements for the study of light matter interactions.. The extremely small mirror spacing in these cavities makes access to the inner cavity region a challenge for researchers [146]. One possible solution is to integrate hollow waveguides with the domed cavities. The integrated waveguides could offer a pathway to supply atoms to the cavities, as well as to guide optical trapping or interrogation beams towards the cavity [145]. Improvements to the fabrication process would see simultaneous improvements to

the waveguide capabilities and the performance of the optical cavities. This highlights a particular advantage of the buckling self-assembly platform: the capability to fabricate complex optical components in parallel on a single chip.

References

1. X. Fan and I. M. White, "Optofluidic Microsystems for Chemical and Biological Analysis," Nat. Photonics **5**, 591–597 (2011).
2. H. Schmidt and A. R. Hawkins, "Optofluidic waveguides: I. Concepts and implementations," Microfluid. Nanofluidics **4**, 3–16 (2008).
3. J. W. Parks, H. Cai, L. Zempoaltecatl, T. D. Yuzvinsky, K. Leake, A. R. Hawkins, and H. Schmidt, "Hybrid optofluidic integration," Lab Chip **13**, 4118–4123 (2013).
4. H. Schmidt and A. R. Hawkins, "Atomic spectroscopy and quantum optics in hollow-core waveguides," Laser Photon. Rev. **4**, 720–737 (2010).
5. C. Derntl, M. Schneider, J. Schalko, A. Bittner, J. Schmiedmayer, U. Schmid, and M. Trupke, "Arrays of open, independently tunable microcavities," Opt. Express **22**, 7 (2014).
6. L. Greuter, S. Starosielec, D. Najer, A. Ludwig, L. Duempelmann, D. Rohner, and R. J. Warburton, "A small mode volume tunable microcavity: Development and characterization," Appl. Phys. Lett. **105**, 121105 (2014).
7. R. G. DeCorby, N. Ponnampalam, E. Epp, T. Allen, and J. N. McMullin, "Chip-scale spectrometry based on tapered hollow Bragg waveguides," Opt. Express **17**, 16632–45 (2009).
8. T. W. Allen, J. Silverstone, N. Ponnampalam, T. Olsen, A. Meldrum, and R. G. DeCorby, "High-finesse cavities fabricated by buckling self-assembly of a-Si/SiO2 multilayers," Opt. Express **19**, 18903–9 (2011).
9. S.-S. Lo, M.-S. Wang, and C.-C. Chen, "Semiconductor hollow optical waveguides formed by omni-directional reflectors," Opt. Express **12**, 6589–93 (2004).
10. M. Kumar, "A hollow waveguide Bragg reflector: A tunable platform for integrated photonics," Opt. Laser Technol. **65**, 5–13 (2015).
11. Y. Zhao, S. Liu, J. Keeley, M. Jenkins, K. Leake, H. Schmidt, and A. R. Hawkins, "Hollow waveguides with low intrinsic photoluminescence fabricated with Ta2O5 and SiO2 films," Appl. Phys. Lett. **23**, 1466–1468 (2011).
12. L. Pang, H. M. Chen, L. M. Freeman, and Y. Fainman, "Optofluidic devices and applications in photonics, sensing and imaging," Lab Chip **12**, 3543–51 (2012).
13. D. Yin, D. W. Deamer, H. Schmidt, J. P. Barber, and A. R. Hawkins, "Single-molecule

detection sensitivity using planar integrated optics on a chip," Opt. Lett. **31**, 2136–2138 (2006).

14. A. R. Hawkins and H. Schmidt, "Optofluidic waveguides: II. Fabrication and structures," Microfluid. Nanofluidics **4**, 17–32 (2008).
15. K. Okamoto, *Fundamentals of Optical Waveguides*, 2nd Ed. (Academic Press, 2006).
16. A. Datta, I. Y. Eom, A. Dhar, P. Kuban, R. Manor, I. Ahmad, S. Gangopadhyay, T. Dallas, M. Holtz, H. Temkin, and P. K. Dasgupta, "Microfabrication and characterization of Teflon AF-coated liquid core waveguide channels in silicon," IEEE Sens. J. **3**, 788–795 (2003).
17. S. H. Cho, J. Godin, and Y. H. Lo, "Optofluidic waveguides in Teflon AF-coated PDMS microfluidic channels," IEEE Photonics Technol. Lett. **21**, 1057–1059 (2009).
18. N. Gopalakrishnan, K. S. Sagar, M. B. Christiansen, M. E. Vigild, S. Ndoni, and A. Kristensen, "UV patterned nanoporous solid-liquid core waveguides," Opt. Express **18**, 12903–12908 (2010).
19. W. Risk, H. Kim, R. Miller, H. Temkin, and S. Gangopadhyay, "Optical waveguides with an aqueous core and a low-index nanoporous cladding," Opt. Express **12**, 6446–6455 (2004).
20. H. Schmidt, D. Yin, D. W. Deamer, J. P. Barber, and A. R. Hawkins, "Integrated ARROW waveguides for gas/liquid sensing," Proc. SPIE **5515**, 67–80 (2004).
21. T. Miura, F. Koyama, and A. Matsutani, "Modeling and Fabrication of Hollow Optical Waveguide for Photonic Integrated Circuits," Jpn. J. Appl. Phys. **41**, 4785–4789 (2002).
22. M. A. Duguay, Y. Kokubun, T. L. Koch, and L. Pfeiffer, "Antiresonant reflecting optical waveguides in SiO2-Si multilayer structures," Appl. Phys. Lett. **49**, 13–15 (1986).
23. D. Yin, J. P. Barber, A. R. Hawkins, and H. Schmidt, "Waveguide loss optimization in hollow-core ARROW waveguides," Opt. Express **13**, 9331 (2005).
24. H. Schmidt, D. Yin, J. P. Barber, and A. R. Hawkins, "Hollow-core waveguides and 2-D waveguide arrays for integrated optics of gases and liquids," IEEE J. Sel. Top. Quantum Electron. **11**, 519–527 (2005).
25. S. Kühn, B. S. Phillips, E. J. Lunt, A. R. Hawkins, and H. Schmidt, "Ultralow power trapping and fluorescence detection of single particles on an optofluidic chip," Lab Chip

10, 189–94 (2010).

26. S. Dasgupta, A. Ghatak, and B. P. Pal, "Analysis of Bragg reflection waveguides with finite cladding: An accurate matrix method formulation," Opt. Commun. **279**, 83–88 (2007).
27. E. Epp, N. Ponnampalam, W. Newman, B. Drobot, J. N. McMullin, A. F. Meldrum, and R. G. DeCorby, "Hollow Bragg waveguides fabricated by controlled buckling of Si/SiO2 multilayers," Opt. Express **18**, 24917–24925 (2010).
28. B. Drobot, A. Melnyk, M. Zhang, T. W. Allen, and R. G. DeCorby, "Visible-band dispersion by a tapered air-core Bragg waveguide," Opt. Express **20**, 23906–11 (2012).
29. N. Ponnampalam and R. G. Decorby, "Self-assembled hollow waveguides with hybrid metal-dielectric Bragg claddings," Opt. Express **15**, 12595–604 (2007).
30. R. G. Decorby, N. Ponnampalam, H. T. Nguyen, M. M. Pai, and T. J. Clement, "Guided self-assembly of integrated hollow Bragg waveguides," Opt. Express **15**, 3902–15 (2007).
31. S. Campopiano, R. Bernini, L. Zeni, and P. M. Sarro, "Microfluidic sensor based on integrated optical hollow waveguides," Opt. Lett. **29**, 1894 (2004).
32. D. Yin, H. Schmidt, J. Barber, and A. Hawkins, "Integrated ARROW waveguides with hollow cores," Opt. Express **12**, 2710–2715 (2004).
33. H. A. Macleod, *Thin Film Optical Filters*, Fourth Ed. (CRC Press, 2010).
34. G. Rempe, R. J. Thompson, H. J. Kimble, and R. Lalezari, "Measurement of ultralow losses in an optical interferometer," Opt. Lett. **17**, 363–365 (1992).
35. M. Born and E. Wolf, *Principles of Optics*, 7th Ed. (Cambridge University, 1999).
36. P. Yeh, *Optical Waves in Layered Media* (Wiley-Interscience, 1988).
37. A. F. Turner and P. W. Baumeister, "Multilayer mirrors with high reflectance over an extended spectral region," Appl. Opt. **5**, 69–76 (1966).
38. M. H. Macdougal, H. Zhao, P. D. Dapkus, and M. Ziari, "Wide-bandwidth distributed Bragg reflectors using oxide/GaAs multilayers," Electron. Lett. **30**, 1147–1149 (1994).
39. Y. Fink, J. N. Winn, S. Fan, C. Chen, J. Michel, D. John, E. L. Thomas, and J. D. Joannopoulos, "A dielectric omnidirectional reflector," Science **282**, 1679–82 (1998).
40. J. D. Joannopoulos, S. G. Johnson, J. N. Winn, and R. D. Meade, *Photonic Crystals: Molding the Flow of Light* (Princeton university press, 2011).

41. J. N. Winn, Y. Fink, S. Fan, and J. D. Joannopoulos, "Omnidirectional reflection from a one-dimensional photonic crystal," Opt. Lett. **23**, 1573–1575 (1998).
42. R. D. Meade, A. M. Rappe, K. D. Brommer, J. D. Joannopoulos, and O. L. Alerhand, "Accurate theoretical analysis of photonic band-gap materials," Phys. Rev. B **48**, 8434–8437 (1993).
43. J. Li and K. S. Chiang, "Guided modes of one-dimensional photonic bandgap waveguides," J. Opt. Soc. Am. **24**, 1942–1950 (2007).
44. B. E. A. Saleh and M. C. Teich, *Fundamentals of Photonics* (Wiley, 2007).
45. T. Tamir, "Leaky waves in planar optical waveguides," Nouv. Rev. d'Optique **6**, 273–284 (1975).
46. P. Yeh, A. Yariv, and C.-S. Hong, "Electromagnetic propagation in periodic stratified media. I. General theory," JOSA **67**, 438 (1977).
47. E. Hecht, *Optics*, Fourth Edi (Addison-Wesley, 2002).
48. J. Chilwell and I. Hodgkinson, "Thin-films field-transfer matrix theory of planar multilayer waveguides and reflection from prism-loaded waveguides," J. Opt. Soc. Am. A **1**, 742 (1984).
49. A. Yariv and P. Yeh, *Optical Waves in Crystals* (Wiley, 1984).
50. F. Koyama, T. Miura, and Y. Sakurai, "Tunable Hollow Optical Waveguides and Their Applications for Photonic Integrated Circuits," Electron. Commun. **89**, 388–396 (2006).
51. L. B. Freund and S. Suresh, *Thin Film Materials: Stress, Defect Formation and Surface Evolution* (Cambridge University Press, 2003).
52. M. E. Doerner and W. D. Nix, "Stresses and deformation processes in thin films on substrates," Crit. Rev. Solid State Mater. Sci. **14**, 225–268 (1988).
53. G. Gioia and M. Ortiz, "Delamination of compressed thin films," Adv. Appl. Mech. **33**, 119–192 (1997).
54. M. W. Moon, K. R. Lee, K. H. Oh, and J. W. Hutchinson, "Buckle delamination on patterned substrates," Acta Mater. **52**, 3151–3159 (2004).
55. M. W. Moon, H. M. Jensen, J. W. Hutchinson, K. H. Oh, and A. G. Evans, "The characterization of telephone cord buckling of compressed thin films on substrates," J. Mech. Phys. Solids **50**, 2355–2377 (2002).

56. H. H. Yu and J. W. Hutchinson, "Influence of substrate compliance on buckling delamination of thin films," Int. J. Fract. **113**, 39–55 (2002).
57. B. Audoly, "Stability of Straight Delamination Blisters," Phys. Rev. Lett. **83**, 4124–4127 (1999).
58. N. Ponnampalam and R. G. DeCorby, "Out-of-plane coupling at mode cutoff in tapered hollow waveguides with omnidirectional reflector claddings," Opt. Express **16**, 2894–908 (2008).
59. B. A. Drobot, A. D. Melnyk, T. W. Allen, and R. G. DeCorby, "Tapered air-core Bragg waveguide spectrometers for lab-on-a-chip applications," Proc. SPIE **8726**, 87260V–87260V–7 (2013).
60. A. Melnyk, T. Thiessen, B. Drobot, T. Allen, and R. G. Decorby, "Tapered air-core Bragg waveguides for spectrally resolved fluorescence detection on a chip," in *Frontiers in Optics 2014* (2014), p. FW4B.4.
61. J. R. Lakowicz, *Principles of Fluorescence Spectroscopy*, 3rd ed. (Springer, 2006).
62. Z. Hu, A. Glidle, C. N. Ironside, M. Sorel, M. J. Strain, J. Cooper, and H. Yin, "Integrated microspectrometer for fluorescence based analysis in a microfluidic format," Lab Chip **12**, 2850–7 (2012).
63. J. A. Wahl, J. S. Van Delden, and S. Tiwari, "Multiple-fluorophore-specie detection with a tapered Fabry-Perot fluorescence spectrometer," Appl. Opt. **44**, 5190–7 (2005).
64. O. Schmidt, M. Bassler, P. Kiesel, C. Knollenberg, and N. Johnson, "Fluorescence spectrometer-on-a-fluidic-chip," Lab Chip **7**, 626–9 (2007).
65. S. Weidong, L. Xiangdong, H. Biqin, Z. Yong, L. Xu, and G. Peifu, "Analysis on the tunable optical properties of MOEMS filter based on Fabry–Perot Cavity," Opt. Commun. **239**, 153–160 (2004).
66. M. Eguchi, "Multilayered effective-index analysis of dielectric waveguides with complicated microstructures," J. Opt. Soc. Am. B **28**, 2478 (2011).
67. R. A. Soref, J. Schmidtchen, and K. Petermann, "Large single-mode rib waveguides in GeSi-Si and Si-on-SiO_2," IEEE J. Quantum Electron. **27**, 1971–1974 (1991).
68. S. P. Pogossian, L. Vescan, and A. Vonsovici, "The Single-Mode Condition for Semiconductor Rib Waveguides with Large Cross Section," J. Light. Technol. **16**, 1851–

1853 (1998).

69. Ö. Duyar, F. Placido, and H. Zafer Durusoy, "Optimization of TiO2 films prepared by reactive electron beam evaporation of Ti3O5," J. Phys. D. Appl. Phys. **41**, 095307 (2008).
70. J. Kim, E. Barnat, E. J. Rymaszewski, and T. Lu, "Frequency-dependent pulsed direct current magnetron sputtering of titanium oxide films," J. Vac. Sci. Technol. A Vacuum, Surfaces, Film. **19**, 429 (2001).
71. H. K. Pulker, G. Paesold, and E. Ritter, "Refractive indices of TiO(2) films produced by reactive evaporation of various titanium-oxygen phases," Appl. Opt. **15**, 2986–2991 (1976).
72. C. H. Heo, S.-B. Lee, and J.-H. Boo, "Deposition of TiO2 thin films using RF magnetron sputtering method and study of their surface characteristics," Thin Solid Films **475**, 183–188 (2005).
73. D. Yoo, I. Kim, S. Kim, C. H. Hahn, C. Lee, and S. Cho, "Effects of annealing temperature and method on structural and optical properties of TiO2 films prepared by RF magnetron sputtering at room temperature," Appl. Surf. Sci. **253**, 3888–3892 (2007).
74. H.-C. Chen, K.-S. Lee, and C.-C. Lee, "Annealing dependence of residual stress and optical properties of TiO2 thin film deposited by different deposition methods," Appl. Opt. **47**, C284–7 (2008).
75. J. E. Klemberg-Sapieha, J. Oberste-Berghaus, L. Martinu, R. Blacker, I. Stevenson, G. Sadkhin, D. Morton, S. McEldowney, R. Klinger, P. J. Martin, N. Court, S. Dligatch, M. Gross, and R. P. Netterfield, "Mechanical characteristics of optical coatings prepared by various techniques: a comparative study," Appl. Opt. **43**, 2670–2679 (2004).
76. H. W. Lehmann and K. Frick, "Optimizing deposition parameters of electron beam evaporated TiO(2) films.," Appl. Opt. **27**, 4920–4 (1988).
77. R. Linsbod, E. Ritter, and K. Leitner, "Evaluation of the oxidation of TiO2 films during reactive evaporation of Ti3O5 and during exposure of the films to the atmosphere," Appl. Opt. **42**, 4580–3 (2003).
78. T. Amotchkina, M. Trubetskov, A. Tikhonravov, I. B. Angelov, and V. Pervak, "Reliable optical characterization of e-beam evaporated TiO2 films deposited at different substrate temperatures," Appl. Opt. **53**, A8–15 (2014).

79. S. Y. Kim, "Simultaneous determination of refractive index, extinction coefficient, and void distribution of titanium dioxide thin film by optical methods," Appl. Opt. **35**, 6703–7 (1996).
80. E. H. Conradie and D. F. Moore, "SU-8 thick photoresist processing as a functional material for MEMS applications," J. Micromechanics Microengineering **12**, 368–374 (2002).
81. J. Gao, A. M. Sarangan, and Q. Zhan, "Experimental confirmation of strong fluorescence enhancement using one-dimensional GaP/SiO2 photonic band gap structure," Opt. Mater. Express **1**, 1216 (2011).
82. A. Melnyk, M. H. Bitarafan, T. W. Allen, and R. G. DeCorby, "Air gap resonant tunneling bandpass filter and polarizer," Opt. Lett. **41**, 1845–1848 (2016).
83. J. A. Dobrowolski, "Optical Properties of Films and Coatings," From Handb. Opt. Fundam. Tech. Des. (1994).
84. A. P. Levick, C. L. Greenwell, J. Ireland, E. R. Woolliams, T. M. Goodman, A. Bialek, and N. P. Fox, "Spectral radiance source based on supercontinuum laser and wavelength tunable bandpass filter : the spectrally tunable absolute irradiance and radiance source," Appl. Opt. **53**, 3508–3519 (2014).
85. I. J. Arnold, H. Moosmüller, N. Sharma, and C. Mazzoleni, "Beam characteristics of fiber-based supercontinuum light sources with mirror- and lens-based beam collimators," Opt. Express **22**, 13860–13869 (2014).
86. R. I. Seddon, B. L. Swaby, R. J. Ryall, S. E. Solberg, and E. W. Anthon, "Monolithic linear variable filter and method of manufacture," U.S. patent 5,872,655 (1999).
87. A. Piegari and J. Bulir, "Variable narrowband transmission filters with a wide rejection band for spectrometry," Appl. Opt. **45**, 3768–3773 (2006).
88. P. W. Baumeister, "Optical tunneling and its applications to optical filters," Appl. Opt. **6**, 897–906 (1967).
89. C. J. Hood, H. J. Kimble, and J. Ye, "Characterization of high-finesse mirrors: Loss, phase shifts, and mode structure in an optical cavity," Phys. Rev. A **64**, 033804 (2001).
90. K. Singh, E. Prenner, and A. D. Streater, "Optical spectral filter, angular filter, and polarizer," U.S. patent US 8,977,082 B2 (2015).

91. L. Li and J. A. Dobrowolski, "Optical coatings with an integral FTIR air layer," Opt. Express **18**, 3784–92 (2010).
92. S. Brand, R. A. Abram, and M. A. Kaliteevski, "Evanescently coupled interface states in the gap between two Bragg reflectors," Opt. Lett. **35**, 2085–7 (2010).
93. G. H. Cross and S. Brand, "Wavelength-dependent frustrated internal reflection via photonic interface states," Appl. Phys. Lett. **99**, (2011).
94. T. W. Allen and R. G. Decorby, "Conditions for admittance-matched tunneling through symmetric metal-dielectric stacks," Opt. Express **20**, A578–A588 (2012).
95. H. A. MacLeod, "A new approach to the design of metal-dielectric thin-film optical coatings," Opt. Acta (Lond). **25**, 93–106 (1978).
96. B. V. Landau and P. H. Lissberger, "Theory of Induced-Transmission Filters in Terms of the Concept of Equivalent Layers," JOSA **62**, 1258–1264 (1972).
97. D. Welch and J. B. Christen, "Seamless integration of CMOS and microfluidics using flip chip bonding," J. Micromechanics Microengineering **23**, 035009 (2013).
98. C. Potts, T. W. Allen, A. Azar, A. Melnyk, C. R. Dennison, and R. G. DeCorby, "Wavelength interrogation of fiber Bragg grating sensors using tapered hollow Bragg waveguides," Opt. Lett. **39**, 5941–4 (2014).
99. D. W. Hoffman, "Perspective on stresses in magnetron-sputtered thin films," J. Vac. Sci. Technol. A Vacuum, Surfaces, Film. **12**, 953 (1994).
100. D. E. Morton, D. Konopka, and F. T. Zimone, "Bipolar Pulsed DC Sputtering of Optical Films," in *42nd Annual SVC Technical Conference* (1999), pp. 217–222.
101. P. J. Kelly and R. D. Arnell, "Magnetron sputtering: a review of recent developments and applications," Vacuum **56**, 159–172 (2000).
102. A. Piegari and F. Flory, eds., *Optical Thin Films and Coatings* (Woodhead Publishing, 2013).
103. G. Bräuer, B. Szyszka, M. Vergöhl, and R. Bandorf, "Magnetron sputtering – Milestones of 30 years," Vacuum **84**, 1354–1359 (2010).
104. K. Seshan, *Handbook of Thin-Film Deposition Processes and Techniques - Principles, Methods, Equipment and Applications (2nd Edition)* (2002).
105. A. Anders, "Physics of arcing , and implications to sputter deposition Physics of arcing ,

and implications to sputter deposition," in *International Conference on Coatings on Glass* (2004), p. LBNL–54220.

106. G. Brauer, J. Szczyrbowski, and G. Teschner, "New approaches for reactive sputtering of dielectric materials on large scale substrates," J. Non. Cryst. Solids **218**, 19–24 (1997).
107. J. Sellers, "Asymmetric bipolar pulsed DC: the enabling technology for reactive PVD," Surf. Coatings Technol. **98**, 1245–1250 (1998).
108. A. Belkind and R. Scholl, "Single-Magnetron Approach Reactive Sputtering of Dielectrics," Vac. Technol. Coat. (2000).
109. W. D. Sproul, D. J. Christie, and D. C. Carter, "Control of reactive sputtering processes," Thin Solid Films **491**, 1–17 (2005).
110. P. J. Kelly, O. A. Abu-Zeid, R. D. Arnell, and J. Tong, "The deposition of aluminium oxide coatings by reactive unbalanced magnetron sputtering," Surf. Coatings Technol. **86**, 28–32 (1996).
111. S.-I. Jun, T. E. McKnight, A. V. Melechko, M. L. Simpson, and P. D. Rack, "Characterisation of reactively sputtered silicon oxide for thin-film transistor fabrication," Electron. Lett. **41**, 822 (2005).
112. V. Bhatt and S. Chandra, "Silicon dioxide films by RF sputtering for microelectronic and MEMS applications," J. Micromechanics Microengineering **17**, 1066–1077 (2007).
113. P. S. Henderson, P. J. Kelly, R. D. Arnell, H. Backer, and J. W. Bradley, "Investigation into the properties of titanium based films deposited using pulsed magnetron sputtering," Surface **174**, 779–783 (2003).
114. P. J. Kelly, C. F. Beevers, P. S. Henderson, R. D. Arnell, J. W. Bradley, and H. Bäcker, "A comparison of the properties of titanium-based films produced by pulsed and continuous DC magnetron sputtering," Surf. Coatings Technol. **174-175**, 795–800 (2003).
115. P. Löbl, M. Huppertz, and D. Mergel, "Nucleation and growth in TiO2 films prepared by sputtering and evaporation," Thin Solid Films **251**, 72–79 (1994).
116. J. Szczyrbowski, G. Bräuer, M. Ruske, J. Bartella, J. Schroeder, and A. Zmelty, "Some properties of TiO2 layers prepared by medium frequency reactive sputtering," Surf. Coatings Technol. **112**, 261–266 (1999).
117. M. N. Inci and T. Yoshino, "A fiber Optic Wavelength Modulation Sensor Based on

Tantalum Pentoxide Coatings for Absolute Temperature Measurements," Opt. Rev. **7**, 205–208 (2000).

118. P. Jain, J. S. Juneja, V. Bhagwat, E. J. Rymaszewski, T. Lu, and T. S. Cale, "Effects of substrate temperature on properties of pulsed dc reactively sputtered tantalum oxide films," J. Vac. Sci. Technol. A Vacuum, Surfaces, Film. **23**, 512 (2005).
119. H. S. Khoo, T. W. Huang, Y. F. Chen, M. H. Chen, T. H. Hsu, and F. G. Tseng, "Improved hydrophobicity of vapor coated chlorosilane self assembled monolayers using evaporative drying of solvent and annealing," in *Solid-State Sensors, Actuators and Microsystems Conference* (2007), pp. 1629–1632.
120. Y. Song and M. Zou, "Superhydrophobic surfaces by dynamic nanomasking and deep reactive ion etching," Proc. Inst. Mech. Eng. Part N J. Nanoeng. Nanosyst. **221**, 41–48 (2008).
121. B. Bhushan, H. Liu, and S. M. Hsu, "Adhesion and Friction Studies of Silicon and Hydrophobic and Low Friction Films and Investigation of Scale Effects," J. Tribol. **126**, 583 (2004).
122. A. K. Gnanappa, O. Slattery, F. Peters, C. O'Murchu, C. O'Mathuna, R. Fahey, J. A. Taylor, and T. N. Krupenkin, "Factors influencing adhesion of fluorocarbon (FC) thin film on silicon substrate," Thin Solid Films **516**, 5673–5680 (2008).
123. Z. J. Liu, Q. Ji, Y. H. Zhang, and Y. Z. Xia, "Deposition of Fluorocarbon Films by RF Magnetron Sputtering at Varying Target-Substrate Distance," Appl. Mech. Mater. **50-51**, 589–593 (2011).
124. A. K. Gnanappa, C. O'Murchu, O. Slattery, F. Peters, B. Aszalós-Kiss, and S. A. M. Tofail, "Effect of annealing on hydrophobic stability of plasma deposited fluoropolymer coatings," Polym. Degrad. Stab. **93**, 2119–2126 (2008).
125. Y. Suzuki, H. Fu, Y. Abe, and M. Kawamura, "Effects of substrate temperature on structure and mechanical properties of sputter deposited fluorocarbon thin films," Vacuum **87**, 218–221 (2013).
126. K.-K. Lee, J.-G. Park, and H.-J. Shin, "Determination of optical properties of fluorocarbon polymer thin films by a variable angle spectroscopic ellipsomtery," in *Materials Research Society Symposium Proceedings* (2000), Vol. 588, pp. 297–302.

127. R. W. W. Jaszewski, H. Schift, B. Schnyder, A. Schneuwly, and P. Gröning, "The deposition of anti-adhesive ultra-thin teflon-like films and their interaction with polymers during hot embossing," Appl. Surf. Sci. **143**, 301–308 (1999).
128. H. V. Jansen, J. G. E. Gardeniers, J. Elders, H. A. C. Tilmans, and M. Elwenspoek, "Applications of fluorocarbon polymers in micromechanics and micromachining," Sensors Actuators A. Phys. **41**, 136–140 (1994).
129. A. A. Ayón, D.-Z. Chen, R. Khanna, R. Braff, H. H. Sawin, and M. A. Schmidt, "A novel integrated MEMS process using fluorocarbon films deposited with a deep reactive ion etching (DRIE) tool," Mater. Res. Soc. Symp. Proc. **605**, 141–147 (1999).
130. S. Keller, D. Haefliger, and A. Boisen, "Optimized plasma-deposited fluorocarbon coating for dry release and passivation of thin SU-8 cantilevers," J. Vac. Sci. Technol. B Microelectron. Nanom. Struct. **25**, 1903 (2007).
131. J. Han, J. Yeom, G. Mensing, D. Joe, R. I. Masel, and M. A. Shannon, "Surface energy approach and AFM verification of the (CF) n treated surface effect and its correlation with adhesion reduction in microvalves," J. Micromechanics Microengineering **19**, 085017 (2009).
132. P. Gröning, "“Self-thickness-limited” plasma polymerization of an ultrathin antiadhesive film," J. Vac. Sci. Technol. A Vacuum, Surfaces, Film. **14**, 3043 (1996).
133. Y. X. Zhuang and A. Menon, "Wettability and thermal stability of fluorocarbon films deposited by deep reactive ion etching," J. Vac. Sci. Technol. A Vacuum, Surfaces, Film. **23**, 434 (2005).
134. N. Amyot, "Electrical and structural Studies of Plasma-polymerized Fluorocarbon Films," Thin Solid Films **238**, 104–109 (1994).
135. C. B. Labelle, V. M. Donnelly, G. R. Bogart, R. L. Opila, and A. Kornblit, "Investigation of fluorocarbon plasma deposition from c-C4F8 for use as passivation during deep silicon etching," J. Vac. Sci. Technol. A Vacuum, Surfaces, Film. **22**, 2500 (2004).
136. J. W. Hutchinson and Z. Suo, "Mixed Mode Cracking in Layered Materials," Adv. Appl. Mech. **29**, 63–191 (1991).
137. D. R. M. Crooks, G. Cagnoli, M. M. Fejer, G. Harry, J. Hough, B. T. Khuri-Yakub, S. Penn, R. Route, S. Rowan, P. H. Sneddon, I. O. Wygant, and G. G. Yaralioglu,

"Experimental measurements of mechanical dissipation associated with dielectric coatings formed using SiO_2, Ta_2O_5 and Al_2O_3," Class. Quantum Gravity **23**, 4953–4965 (2006).

138. W. D. Nix, "Mechanical properties of thin films," Metall. Trans. A **20**, 2217–2245 (1989).
139. G. Alcalá, P. Skeldon, G. E. Thompson, a B. Mann, H. Habazaki, and K. Shimizu, "Mechanical properties of amorphous anodic alumina and tantala films using nanoindetation," Nanotechnology **13**, 451–455 (2002).
140. A. Melnyk, C. A. Potts, T. W. Allen, and R. G. Decorby, "Visible range hollow waveguides by guided buckling of Ta_2O_5/SiO_2 multilayers," Appl. Opt. (in press, 2016).
141. A. A. P. Trichet, J. Foster, N. E. Omori, D. James, P. R. Dolan, G. M. Hughes, C. Vallance, and J. M. Smith, "Open-access optical microcavities for lab-on-a-chip refractive index sensing," Lab Chip **14**, 4244–9 (2014).
142. T. A. Strasser and M. C. Gupta, "Optical loss measurement of low-loss thin-film waveguides by photographic analysis," Appl. Opt. **31**, 2041–6 (1992).
143. K. V Popov, J. A. Dobrowolski, A. V Tikhonravov, and B. T. Sullivan, "Broadband high-reflection multilayer coatings at oblique angles of incidence," Appl. Opt. **36**, 2139–51 (1997).
144. A. Arpa, G. Wetzstein, D. Lanman, and R. Raskar, "Single lens off-chip cellphone microscopy," IEEE Comput. Soc. Conf. Comput. Vis. Pattern Recognit. Work. 23–28 (2012).
145. C. A. Potts, A. Melnyk, H. Ramp, M. H. Bitarafan, D. Vick, L. J. LeBlanc, J. P. Davis, and R. G. DeCorby, "Tunable open-access microcavities for on-chip cavity quantum electrodynamics," Appl. Phys. Lett. **108**, 041103 (2016).
146. H. Mabuchi and A. C. Doherty, "Cavity quantum electrodynamics: coherence in context," Science **298**, 1372–1377 (2002).